CHARACTERIZATION OF MICROSTRUCTURE AND INTERNAL DISPLACEMENT FIELD OF SAND USING X-RAY COMPUTED TOMOGRAPHY

By

MOHAMMAD REZA RAZAVI

A dissertation submitted in partial fulfillment of
the requirements for the degree of

DOCTOR OF PHILOSOPHY

WASHINGTON STATE UNIVERSITY
Department of Civil and Environmental Engineering

December 2006

To the Faculty of Washington State University:

The members of the Committee appointed to examine the dissertation of MOHAMMAD REZA RAZAVI find it satisfactory and recommend that it be accepted.

_____
Chair

_____

_____

_____

ACKNOWLEDGEMENTS

First and foremost I wish to thank my advisor, Professor Muhunthan for his support, patience, guidance, friendship, and encouragement from the first day that I applied for the PhD program at Washington State University. While I was writing the thesis, he gave me the moral support and freedom I needed to move on.

I would like to thank all of my thesis committee members, Professor Stephen Antolovich, Professor Hussein Zbib, and Professor Adrian Rodriguez-Marek for their continuous support and their helpful comments. Special thanks to Professor Stephen Antolovich for all his friendship, kindness, help, and support from the first day I met him. I also would like to thank Professor David Field for all of his kindness and help.

Many people at Washington State University helped me through my studies and provided a pleasant environment for me, which I will always remember and be thankful for. I would like to thank Maureen Clausen, Larissa Morton, Kathy Cox, Glenda Rogers, Vickie Ruddick, Lola Gillespie, Cyndi Whitmore, Mary Furnari, Roslyn Carlson, Kevin Emerson, Tom Weber, Bill Elliott, Jon Grimes, and Robert Lentz.

I would like to thank two great friends, Larissa Morton and Cyndi Whitmore, who have always been there for my wife and me during the most difficult times.

I would like to thank my wife, Morvarid, for all she has done to help me reach my goals. Without her support, help and sacrifices, it would not be possible for me to accomplish this study.

My parents, brothers and sister have always supported me and provided me the best in my life and I will always be thankful to them all.

I would like to thank Professor Omar Al Hatamleh for all his help and encouragement. Professor William Clocksin, Professor Larry Lake, and Professor Michael Dennis, helped me by providing very useful information for my research and I would like thank them.

I also would like to thank all of my friends and colleagues at Washington State University for their kindness and their cooperation.

Steve Schramm, Anthony Davis, and Tony Melton, from HYTEC, helped me to learn the X-ray CT and assisted with every problem I had with X-ray CT, and I would like to thank them.

Daniel Eaton, from British Columbia University, provided me fast 3-D normalized cross correlation code in MATLAB. It was a great help to reduce the analysis time and I appreciate his kindness.

I would like to thank Professor Nasser Talebbeydokhti, from Civil Engineering Department at Shiraz Engineering University, who did a great job allowing me to continue my studies at Washington State University.

Professor Hamid Seyyedian, a great friend and teacher from Civil Engineering Department at Shiraz Engineering University, who helped and supported me in following my dreams and encouraging me to never give up. I am always thankful to him.

I would like to thank Professor Arsalan Ghahramani, Professor Ghassem Habibagahi, Professor Nader Hataf, and the other Professors in Civil Engineering Department at Shiraz Engineering University, for all their kindness and support.

Financial support by the National Science Foundation and Civil Engineering Department at Washington State University is gratefully acknowledged.

CHARACTERIZATION OF MICROSTRUCTURE AND INTERNAL DISPLACEMENT FIELD OF SAND USING X-RAY COMPUTED TOMOGRAPHY

Abstract

by Mohammad Reza Razavi, Ph.D.
Washington State University
December 2006

Chair: Balasingam Muhunthan

This study presents a systematic method to examine the microstructure characteristics and internal displacement field of sands using X-ray computed tomography (CT) images. The 3-D images of spherical glass beads, Silica sand, and Ottawa sand are characterized using advanced image processing techniques.

An interactive computer program is developed to study porosity variation with increasing radius of a spherical volume from the 3-D images of these materials. The porosity variation of Silica sand and Ottawa sand shows three characteristic regions: an initial fluctuation region due to microscopic variations, a constant plateau region, and a region with a monotonic increase/decrease due to heterogeneity. The homogenous medium of glass beads did not show the last region. The results show that for the spherical glass beads the representative elementary volume radius is about 2 to 3 times the average diameter. The radius for Silica sand composed mainly of elongated particles is between 5 to 11 times of d_{50} and for Ottawa sand composed mainly of subrounded particles is between 9 to 16 times of d_{50}. These values appear to justify the use of 10 to 20 diameters of sand grains adopted in some past studies.

A novel triaxial system is designed to facilitate the characterization of the 3-D images of soil microstructure and its evolution nondestructively in real time using X-ray computed tomography while it is subjected to shearing. The system was designed to have a total weight of 500 N, capable to increase the cell pressure up to 400 kPa, and applying up to 10 kN axial load. Moreover, the system is designed to be able to do temperature controlled (-10 to 65 °C) triaxial and uniaxial tests on many different materials, including soil, asphalt concrete, wood, small metal specimens, and composites. The system is fully microprocessor controlled using a workstation outside of the protection cabinet of X-ray CT. Load can be kept constant, or applied either in strain control or stress control.

A computer code is developed to determine the internal displacement field in sands by comparing two successive X-ray CT images. The method is an extension of the template matching technique used in image processing for 3-D situations. The program is verified by applying a known displacement or rotation to the reference image. An interactive computer program is developed to find the changes in local porosity distribution within the sand specimen as it is subjected to shearing. The ability to quantify the internal displacement and local porosity would contribute in the characterization of strain localization and shear band development.

TABLE OF CONTENTS

LIST OF FIGURES

LIST OF TABLES

To My Wife, Morvarid

Chapter 1

INTRODUCTION

1.1 Introduction

The macroscopic stress strain response of granular materials is influenced by its microstructure. However, the difficulties associated with internal measurements have resulted in the development of constitutive models for granular materials mostly based on deformations measured on the boundaries of laboratory specimens or field tests. Since deformation is progressive, such boundary measurements may not reflect the internal changes that occur in granular microstructure that control the overall macroscopic response. This becomes even more complicated when the boundary condition of the continuum is kept unchanged and the internal strains concentrate into a narrow zone called shear band. Microscopic observations have shown several shear bands to form initially that coalesce into one or two dominant shear bands before failure. From a continuum mechanics standpoint, the shear band phenomenon results in a discontinuity and classical theories fail. Therefore, shear band characteristics must be accounted for when predicting the constitutive behavior granular materials. This is done in a phenomenological manner by either increasing the kinematic degrees of freedom of the particles (Vardoulakis 1989; de Borst 1992; Fleck and Hutchinson 1993) or by using integral (Bazant and Gambarova 1984) or gradient theories (Mindlin 1964; Aifantis 1987; Zbib and Aifantis 1988; Vardoulakis 1996; Al Hattamleh et al. 2003).

The fundamental continuum hypothesis is that the behavior of many physical elements is essentially the same as if they were perfectly continuous. Physical quantities, such as mass and density, associated with individual elements contained within a representative elementary volume (REV) are regarded as being spread over the volume instead of being concentrated on each particle or element. Macroscopic variables are defined typically as averages of microscopic variables over a REV.

The REV of a continuum has been qualitatively assumed to be sufficiently large so that granular fluctuations are smoothened out but sufficiently small so that the macroscopic changes do not affect the result (Bear 1972; Dullien 1979). The difficulties associated with the measurement and the characterization of granular microstructure had prevented the identification of the size of REV in real media. Some measurements relating to the REV of glass beads have been made recently by Culligan et al. (2004) using a cubical elementary volume. Numerical simulations of particle assemblies have also been made to determine the REV for relevant properties (Stroeven et al. 2004; Ostoja-Starzewski 2005).

In the absence of experimental measurements, the minimum dimensions of the REV are set by the grain size with the best guess being the REV is between 100 to 1000 grain diameters. For sandy soils, a REV with a radius of 10 to 20 grain diameters appears to have been adequate for obtaining well defined average for applications in ground water flow (Charbeaneau 2000). Despite all the hurdles, the notion of REV is absolutely essential for engineering applications because it enables the use of continuum measures that can be adopted in practice. This study makes use of the current advances in microstructure characterization to accurately quantify the characteristics of REV of sands

and glass beads nondestructively using high resolution X-ray computed tomography (X-ray CT).

Few studies have been performed to monitor granular deformation using X-ray CT in real time. Geraud et al. (1998) have used CT to observe crack locations in granitic samples subjected to heat, low confining pressure and axial loading. A real time X-ray CT triaxial testing was performed on a coal specimen to determine the meso-damage evolution law (Ge et al. 1999). Similar X-ray CT triaxial tests have been performed on soils to study evolution of shear bands in a qualitative manner (Otani et al. 2000 and 2001). By tracing the movement of glass beads within a hot mix asphalt triaxial specimen Chang et al. (2003) have made quantitative measurements of the displacement field as well as the changes in the fabric tensor. Sun et al. (2004) have performed a series of triaxial tests on a silty clay soil using a medical CT scanner and related the CT numbers to stress-strain behavior of the soil. These measurements were limited to the determination of damage and heterogeneity of the intact clay. Desrues et al. (1996) studies local void ratio in the localization zones in triaxial tests on sand using X-ray CT. Desrues (2004) studied evolution of shear band in triaxial specimens in an aluminum cell. However, the tests were not performed directly inside the scanner measuring field.

None of the above studies have quantified the displacements of the soil particles and evolution of shear band characteristics nondestructively. In this study, a special triaxial apparatus is designed to perform real time monitoring of deformation within the X-ray CT chamber. The displacement field is calculated by processing of the X-ray CT

images in 3-D using special computer vision techniques. The local void ratio changes at various strain levels are monitored to study the evolution of shear bands.

1.2 Objectives

The main objectives of this research are to:

1. Study the characteristics of the representative elementary volume using X-ray CT.
2. Develop a novel triaxial apparatus for use with X-ray CT for real time monitoring of granular microstructure evolution.
3. Develop a method to determine the 3-D internal displacement field and local porosity distribution using X-ray CT images.

1.3 Organization of the Thesis

A background to this study is given in chapter 2. It includes past studies on real time monitoring of shear band evolution and characterization. The results, conclusions, advantages and drawbacks of these studies are discussed briefly. The chapter also includes discussion on methods to determine 2-D displacement fields within soil specimens and three dimensional fields for asphalt specimens.

Representative elementary volume (REV) of sand is discussed in chapter 3. REV and its characteristics for glass beads, silica sand, and Ottawa sand are studied. An interactive 3-D image processing computer program is developed. The effects of the location of the REV center, shape and angularity of particles on the size of REV are studied.

The development of a novel triaxial device that can be placed inside the X-ray CT chamber is detailed in chapter 4.

Chapter 5 describes the extension of 2-D computer vision techniques to 3-D to trace displacement fields. The algorithm of the developed interactive computer program, based on template matching technique is provided. Verification of the program is examined by moving several 3-D images with known displacements.

Development a method to characterize 3-D porosity distribution is explained in chapter 6. Variation of the local porosity is applied as a criterion to study the evolution of shear band. A series of computer programs are developed to accomplish these tasks.

Chapter 7 includes a summary of the conclusions, and findings of the study, as well as recommendations for future research on this topic.

Basic details on X-Ray Computed Tomography, an overview to digital image processing, and an alternate design of X-ray CT triaxial for large loads are given in Appendices A, B, and C. User's manuals of the various computer programs such as MFC, M-REV, and M-DST computer programs are provided in an internal report of Washington State University (Razavi 2006).

Chapter 2

BACKGROUND

2.1 Introduction

X-ray computed tomography (CT) is an advanced imaging technique, which generates 3-D high resolution images (down to 5 μm spatial resolution at the present time) of the microstructure of engineering materials. This resolution is sufficient to detect and separate sand particles. X-ray CT combined with testing instruments and image processing techniques enable us with a capability to advance the state-of-art in microstructure characterization and monitoring of the desired variables in real time.

The development of a triaxial X-ray cell in the early 90's (Geraud 1991; Vinegar et al. 1991) was a significant step in studies associated with real time monitoring of geomaterials using X-ray CT. Since then the number of studies in this area have been growing significantly with improving capabilities of the X-ray CT machines, computer hardware and software, and image processing techniques.

2.2 Determination of Representative Elementary Volume using X-ray CT

X-ray CT has been used to measure different properties of porous media such as volume fractions, porosity, and pore size distribution (Warner et al. 1989; Spanne et al. 1994; Auzerais et al. 1996; Klobes et al. 1997; Clausuitzer and Hopmans 1999; Cislerova and Votrubova 2002; Al Ramahi 2004; Al Raoush and Willson 2005; Al Raoush and Alshibli 2006). Three different regions in the plot of porosity versus the size of a cubical

elementary volume for glass beads specimens were recognized by Culligan et al. (2004). These regions are microscopic fluctuations, constant region, and macroscopic heterogeneity, which had been introduced by Bear (1972) and Dullien (1979). Measurement of REV for sand based on pore network properties from 3-D X-ray CT images also appears in the works by Al Roush and Willson (2005). All the past studies suffer from using glass beads instead of real sand or using a cubical region instead of a spherical region or both.

2.3 Triaxial and X-ray CT for Real Time Monitoring

X-ray CT has been used widely to characterize soil microstructure and evolution of shear band (Desrues et al. 1996; Tani 1997; Shi et al. 1999; Otani 2000; Alshibli et al. 2000, 2003; Wang 2004; Viggiani 2004; Desrues 2004).

The regular method to hold the locations of grains is to use of a low density adhesive material like resin filling the pore spaces (Alshibli et al. 2000). However, a fixed specimen with resin can no longer be used for the next loading or unloading step. This poses problems in the study of any strain dependent phenomena, such as evolution of shear band in a particular specimen. In addition a small disturbance due to injection of resin into the pores is always expected. To overcome these difficulties a few researchers modified the triaxial apparatus to load the specimen and take CT images at the same time. However, it is important to keep in mind that at the present time even the fastest CT scanners need a couple of minutes (depends on the image size and quality) to take a 3-D CT image, and on the other hand the specimen cannot be loaded during scanning to avoid blurriness.

Geraud et al. (1998) have used X-ray CT to observe crack locations in triaxial granite samples subjected to heat up to 180°C and a maximum confining pressure of 10 MPa. They developed a triaxial X-ray transparent cell for real time monitoring (Geraud 1991; Vinegar et al. 1991). The cell had to withstand a maximum confining pressure of 28 MPa and temperature of up to 180° C for granite samples 40 mm in diameter. They used a beryllium tube to use as for the confining pressure cell and an aluminum tube to compensate the strain induced by the confining pressure. In this manner they could observe the porosity variations under different mechanical and thermal loading conditions directly.

Ge et al. (1999) used the triaxial apparatus in X-ray CT to find a meso-damage evolution law for coal in real time. Li and Zhang (2000) monitored the changes in the structure of road foundation soil in uniaxial compression test with X-ray CT.

Otani et al. (2001) developed a new triaxial apparatus for maximum axial load and confining pressure of 1 kN and 400 kPa, respectively. The steel rods around a transparent cell were removed to enable X-ray penetration. A motor was placed on top of the cell to apply loads. The size of soil specimen was limited to 50 mm in diameter and 100 mm in height. Triaxial compression tests under consolidated drained conditions were conducted on Toyoura Sand with relative density of 65.3% (minimum dry density of 1330 kg/m^3 and maximum dry density of 1650 kg/m^3). The specimen was consolidated to 49 kPa confining pressure. It was scanned before applying the axial load to have an image of the initial condition. Loading and unloading of the specimen was performed at strain level intervals of 3%. The specimen was scanned when the deviatoric stress reached zero to avoid the effect of stress relaxation (Otani et al. 2001). This

process was continued until a strain level of 15.0%. The X-ray CT system needed 5 min to scan one slice of CT images. Based on a qualitative analysis, the shape and characteristics of the soil failure were evaluated.

Damage evolution of natural expansive soil during triaxial test was studied by Lu et al. (2002) using X-ray CT. Viggiani et al. (2004) used a compact triaxial apparatus similar to that of Otani et al. (2001) to conduct a qualitative study on localized deformation in saturated Beaucaire Marl (a sedimentary soil) using X-ray CT.

Sun et al. (2004) studied deformation characteristics of triaxial silty clay specimens using a medical X-ray CT scanner. Inhomogeneity and original damage of the silty clay were observed by inspection of the CT images and variation of CT numbers. The triaxial apparatus was placed horizontally inside the medical X-ray CT scanner. Therefore, the tests cannot be considered to be axisymmetric.

2.4 Internal Displacement Fields using X-ray and X-Ray CT

There are two different techniques to calculate the internal displacement fields using X-ray or X-ray CT at the present time; tracing easily X-ray detectable markers such as small metallic spheres (Nemat-Nasser and Okada 2001; Wood 2002) or wires (Alshibli and Alramahi 2006), and numerical techniques based on computer vision description (White and Bolton 2001).

Zhou et al. (1995) developed a constrained nonlinear regression model for estimation of displacement fields from a sequence of 3-D X-ray CT images for small displacement gradients. It was shown that the method can determine displacement fields over a range of inter-image displacements of up to eight pixels accurately. Quantitative measurements of displacement fields as well as changes in fabric tensor within hot mix

asphalt and glass bead specimens were made by Chang et al. (2003). By tracing the movement of glass beads in X-ray CT images, the analysis consisted of a 3-D cubic grid embedded in the domain. Neighboring grains are identified within an examination distance. The choice of the distance is depends on the heterogeneous deformation scale. A linear displacement field based on the least square method is lead to fit the displacements of the 18-26 neighboring grains within the examination distance.

Cross correlation or template matching is a classic pattern recognition technique to determine the relative displacements between two images by finding the maximum similarity between different blocks on them. In geotechnical engineering, it has been used to monitor soil deformations during shear (Horii et al. 1998; Guler et al. 1999; White et al. 2001; Rechenmacher and Saab 2002; Sadek 2002). Cross correlation scheme also has been used for monitoring fracture processes in concrete (Shah and Choi 1996; Lawler and Shah 2002). Liu and Iskander (2004) developed an advanced algorithm for cross correlation called adaptive cross correlation (ACC) method to reduce the errors associated with conventional cross correlation technique. ACC technique was used to determine the 2-D displacement fields under a strip footing by comparing images before and after deformation.

2.5 Experimental Observations and Characterization of Shear Bands in Sands

Experimental observations on shear bands have been made by several investigators using a biaxial loading equipment (Vardoulakis 1980; Oda et al. 1982; Han and Drescher 1993; Yoshida et al. 1994; Pradhan 1997; Finno et al. 1997; Oda and Kazama 1998; Alshibli and Sture 2000), simple shear apparatus (Budhu 1984), triaxial apparatus (Desures and Hammad 1989; Yagi et al. 1997; Oda et al. 2004), torsional shear

apparatus (Schanz et al. 1997), and true triaxial apparatus (Wang and Lade 2001). Figure 2.1 shows X-ray CT images around shear band formed in a sand triaxial specimen (Oda et al. 2004).

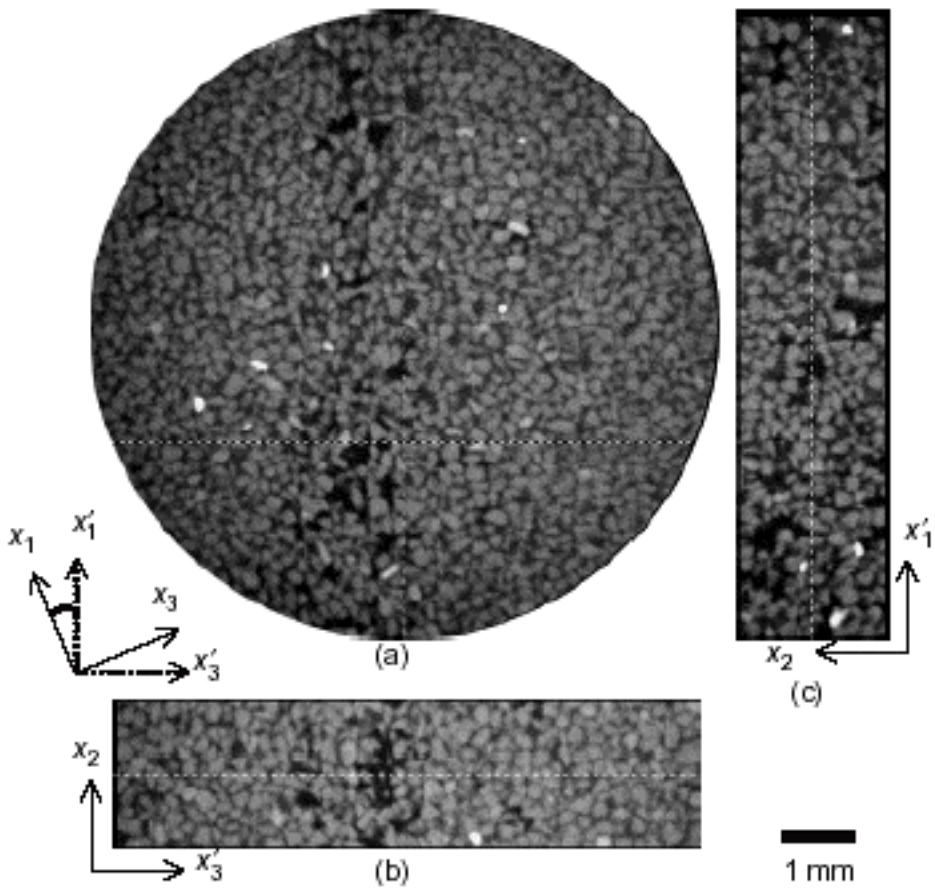

Figure 2.1. 2-D X-ray attenuation images around a shear band (Oda et al. 2004):

(a) 2-D image of x_1-x_3 plane (b) 2-D image of x_1-x_3' plane inside

(b) the shear zone (c) 2-D image of x_1'-x_2 plane

Several different techniques have been used to characterize the shear bands in sand including video images (Saada et al. 1999), digital imaging (Alshibli et al. 1999;

Gudehus and Nubel 2004), radiography (Nemat-Nasser and Okada 2001), X-ray CT (Alshibli et al. 2000; Desures et al. 1996; Tani 1997; Otani 2001; Desures 2004), high speed cameras (Saada et al. 1994), and stereophotogrammetry (Finno et al. 1996). The main focuses of these studies are on shear band inclination, thickness of shear band, and inception of localization.

Chapter 3

REPRESENTATIVE ELEMENTARY VOLUME ANALYSIS FOR POROSITY FOR SAND

3.1 Introduction

The methods of continuum mechanics have provided an effective means of predicting the behavior of the collection of a large number of elements. The fundamental continuum hypothesis is that the behavior of many physical elements within a control volume is essentially the same as if they were perfectly continuous. If the size of the control volume is small, the behavioral property is likely to vary spatially, and the medium is termed heterogeneous although the spatial variation may be smooth. When progressively larger control volumes are used the value of a specific property may tend towards a constant value everywhere in the medium. In such cases, these volumes are defined as the representative elementary volumes and the medium is classified as homogenous. Specifically, physical quantities such as mass and density, associated with individual elements contained within a representative elementary volume (REV) are regarded as being spread over the volume instead of being concentrated on each particle or element. Macroscopic variables are defined typically as averages of microscopic variables over a REV and represent the property of the medium regardless of location. REV is used extensively in multiscale engineering problems and has facilitated the development of a number of macroscopic measures for the description of the mechanistic

and transport behavior of particulate media (Christofferson et al. 1981; Chang 1987; Jenkins 1987; Walton 1987; Meegoda 1997; Muhunthan et al. 1996; Masad et al. 2000).

The fundamental ideas relating to the relevance and existence of REV in granular materials can be illustrated by following the elegant analysis of a one dimensional continuum model by Roberts (1994). Suppose we wish to measure the density of the collection of granular particles at some point x and at some time t placed along a one-dimensional continuum. This can be done by using a sampling length L of the continuum, centered at x, and measuring the mass m of this material in this interval. The density can then be computed by (Roberts 1994):

$$\rho(L;x,t) = \frac{m(L;x,t)}{L} \tag{3.1}$$

The density as computed from Equation 3.1 will be a function of not only of position but also of the sampling length L as shown qualitatively in Figure 3.1. This graph has three distinct regions: in region I, the average density $\rho(L)$ is dominated by microscopic molecular fluctuations caused by the influence of chance when there are only a small number of molecules in an averaging length; in region (II), $\rho(L)$ is essentially constant; while in region III $\rho(L)$ varies smoothly, the variations being caused by the macroscopic non-uniformity of the material. The features of Figure 3.1 for average density are characteristic of other granular properties such as porosity (Bear 1972).

Based on the features described above the REV of a continuum has been qualitatively assumed to be sufficiently large so that granular fluctuations are smoothened out but sufficiently small so that the macroscopic changes do not affect the result (Bear 1972; Dullien 1979). The difficulties associated with the measurement and the

characterization of granular microstructure had prevented the identification of the size of REV in real media except in a few cases. Some measurements relating to the REV of glass beads (Culligan et al. 2004) and of ooid sand (Al-Raoush and Willson 2005) have been made recently using a cubic elementary volume. Numerical simulations of particle assemblies have also been made to determine the REV for relevant properties (Stroeven et al. 2004; Ostoja-Starzewski 2005).

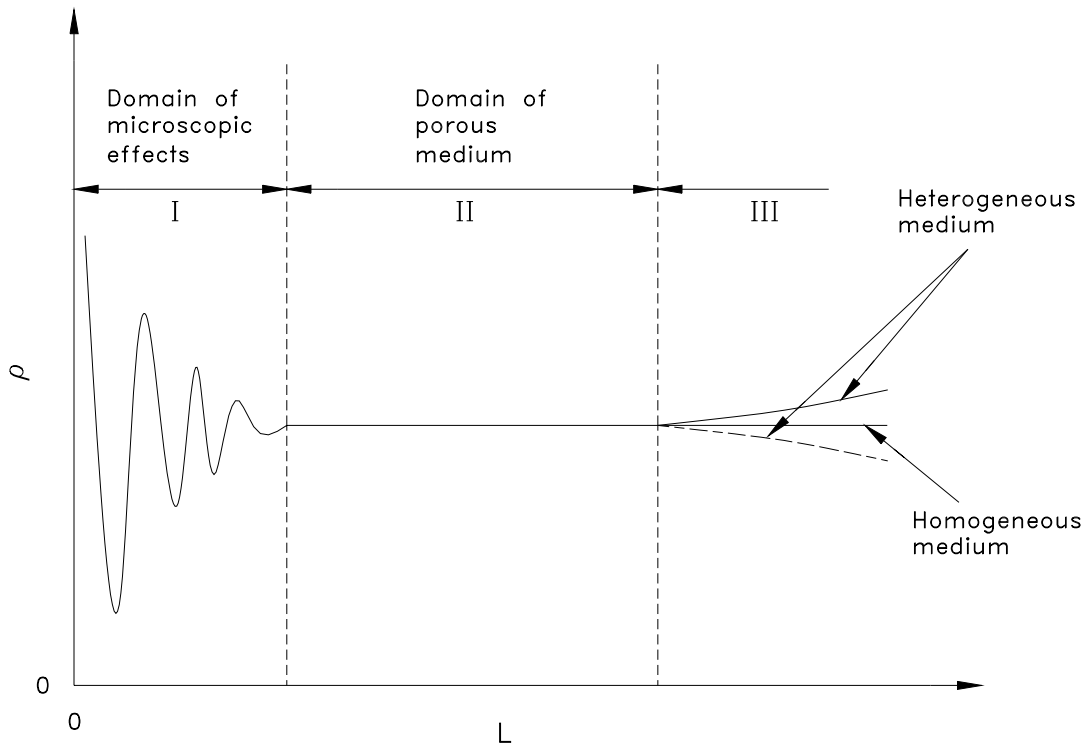

Figure 3.1. Three different regions of variation of density versus length (Roberts 1994)

Recent advances in imaging techniques such as X-ray computed tomography and magnetic resonance imaging have provided geotechnical researchers with superior tools to characterize the microstructure of granular materials (Desrues et al. 1996; Alshibli et al. 2000; Wang et al. 2004). X-ray computed tomography image analysis can be used to

nondestructively characterize the 3-D microstructural features of granular materials and their evolution with shear deformation.

This study makes use of the current advances in microstructure characterization to accurately quantify the characteristics of REV of sands and glass beads. High resolution X-ray computed tomography is used to obtain 3-D images. These images are post processed using robust algorithms to study the variation of the porosity within a spherical volume element.

Based on the features described above the REV of a continuum has been qualitatively assumed to be sufficiently large so that granular fluctuations are smoothed out but sufficiently small so that the macroscopic changes do not affect the result (Bear 1972; Dullien 1979). The difficulties associated with the measurement and the characterization of granular microstructure had prevented the identification of the size of REV in real media. Some measurements relating to the REV of glass beads have been made recently by Culligan et al. (2004) using a cubical elementary volume. Numerical simulations of particle assemblies have also been made to determine the REV for relevant properties (Stroeven et al. 2004; Ostoja-Starzewski 2005).

In the absence of experimental measurements, the minimum dimensions of the REV are set by the grain size with the best guess being the REV is between 100 to 1000 grain diameters. For sandy soils, a REV with a radius of 10 to 20 grain diameters appears to have been adequate for obtaining well defined average for applications in ground water flow (Charbeaneau 2000). Despite all the hurdles, the notion of REV is absolutely essential for engineering applications because it enables the use of continuum measures that can be adopted in practice.

This part of the study makes use of the current advances in microstructure characterization to accurately quantify the characteristics of REV of sands and glass beads. High resolution X-ray CT is used to obtain 3-D images. These images are post processed using robust algorithms, and the variation of the porosity within a spherical volume element is studied.

3.2 Materials and Methods

Specimens were prepared from Ottawa 30-40 sand, silica 30-40 sand, and glass beads with average particle diameters of 6 mm, and 1.6 mm. The shape of the particles was determined by the average axial ratio, $\bar{n}$, defined as the average ratio of the apparent longest axis, L_1, to the apparent shortest axis, L_2, of particles:

$$\bar{n} = \frac{1}{N}\sum_{i=1}^{N}\left(\frac{L_1}{L_2}\right)_i \tag{3.2}$$

where N is the number of particles.

The axial ratio of each material was estimated based on measurements made on 398, 261, and 150 particles on digital photographs for silica sand, Ottawa sand, and glass beads, respectively, using MATLAB image processing toolbox (IPT version 5.1), and was reported in Table 3.1. It can be seen that glass beads are nearly spherical particles, Ottawa sand is composed mainly of subrounded particles, and silica sand is composed mainly of elongated particles. Specific gravity of these materials is also given in Table 3.1.

Cylindrical specimens of dry silica sand and Ottawa sand with different porosities (MR015SON to MR022SON) were prepared in the laboratory. They were compacted in five layers by tamping on the sides of the plastic mold. Two specimens of glass beads

(MR023GLN and MR024GLN) were also prepared. All of the specimens were scanned using X-Ray CT and their 3-D images obtained. Although use of higher magnification gives an image with a better resolution, required memory to store the image increases by the third power of magnification. For example, if a 3-D CT image of a part needs 1 GB memory then increasing the magnification to 2 times, increases the memory usage to 8 GB. Therefore, several preliminary scans were performed to choose the optimum magnification to attain the best resolution within the constraints of the computer memory and the ability to process the images. Based on the results to minimize the error in processing the images, it was found that a magnification of 3.1 was sufficient for specimens MR015SON through MR023GLN, and a magnification of 1.8 for specimen MR024GLN. Table 3.2 shows the X-ray CT scanning parameters, image resolution, and number of voxels for each specimen in the study.

Table 3.1. Properties of the sand and glass beads specimens

Specimen	Type	Diameter, *mm*	Height, *mm*	G_s	d_{50}, *mm*	$\bar{n}$	Porosity
MR015SON	Silica Sand	27.82	150.62	2.70	0.453	1.85	0.462
MR016SON							0.405
MR017SON							0.425
MR018SON							0.401
MR019SON							0.444
MR020SON	Ottawa Sand	27.82	150.62	2.65	0.246	1.40	0.419
MR021SON							0.412
MR022SON							0.451
MR023GLN	Glass Beads	27.82	76.34	2.30	1.6	1.10	0.550
MR024GLN		48.0	74.18		6.0	1.10	0.479

Table 3.2. X-ray CT Scanning parameters of the specimens

Specimen	*E*, *keV*	*I*, *mA*	Image Resolution, *μm/pixel*	Image Size, *voxel*
MR015SON	160	0.284	40.0	675×671×672
MR016SON	160	0.284	39.7	680×679×500
MR017SON	160	0.284	39.8	675×678×500
MR018SON	160	0.284	39.9	676×676×500
MR019SON	160	0.284	39.8	674×679×500
MR020SON	160	0.284	39.5	683×679×500
MR021SON	160	0.284	39.5	679×683×500
MR022SON	160	0.284	39.6	682×682×500
MR023GLN	180	0.203	42.0	628×643×591
MR024GLN	180	0.203	71.3	671×673×500

3.3 REV and Image Characterization

An interactive computer program, M-REV, was developed in MATLAB to perform the analyses on the 3-D CT images. The main features of the M-REV program are presented in the form of a flowchart in Figure 3.2. First, the 3-D CT image is read and stored as a 3-D array so that the reconstructed CT slices show the top view of the specimen. If necessary the gray scale values of the voxels can be rescaled to spread the histogram of the gray scale values between 0 and 255. This is called histogram equalization for intensity adjustment. In most cases, CT slices contain some noise on the image background which tends to propagate a significant error in processing. User can specify the outer boundaries of the specimen in the program to remove background noise. Figure 3.3(a) shows a two-dimensional CT slice of glass beads in which the wall of the container and noise in the background are evident. Figure 3.3(b) shows the same slice after removal of the container walls and the background noise with intensity adjustment.

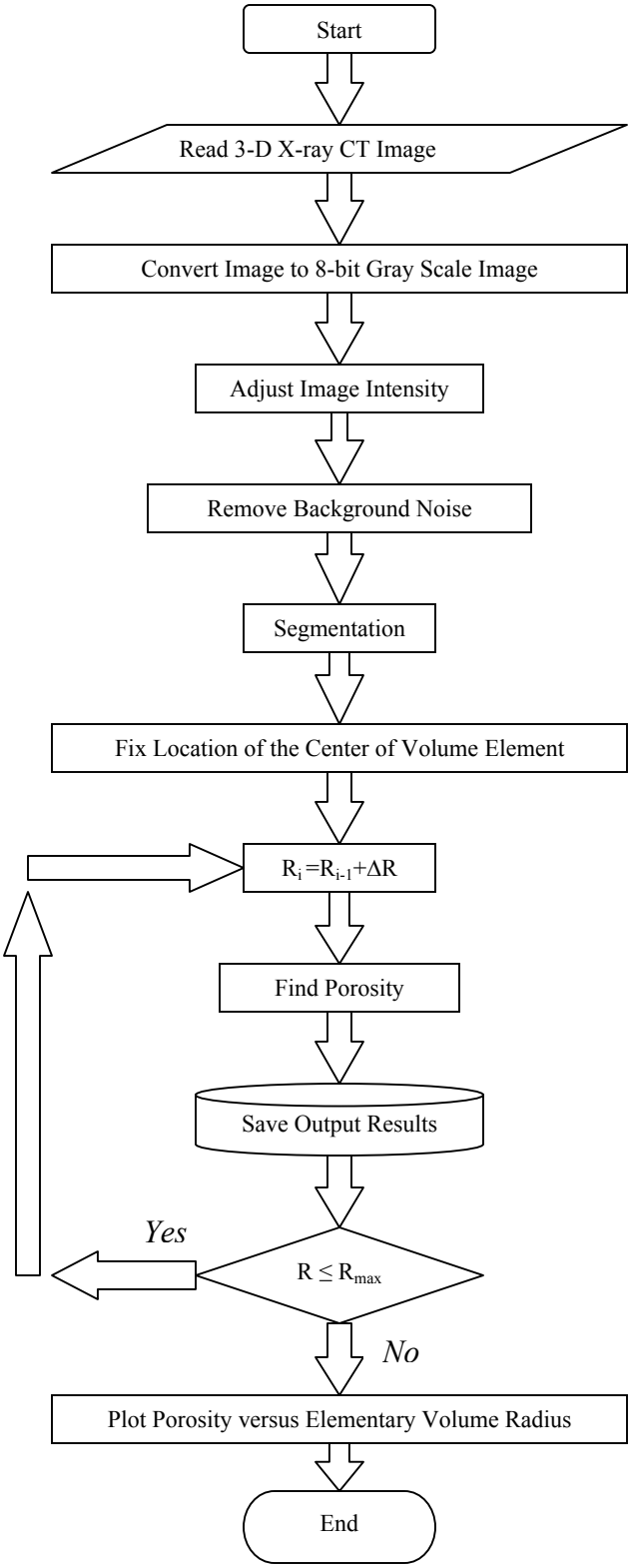

Figure 3.2. Flow chart of the M-REV program

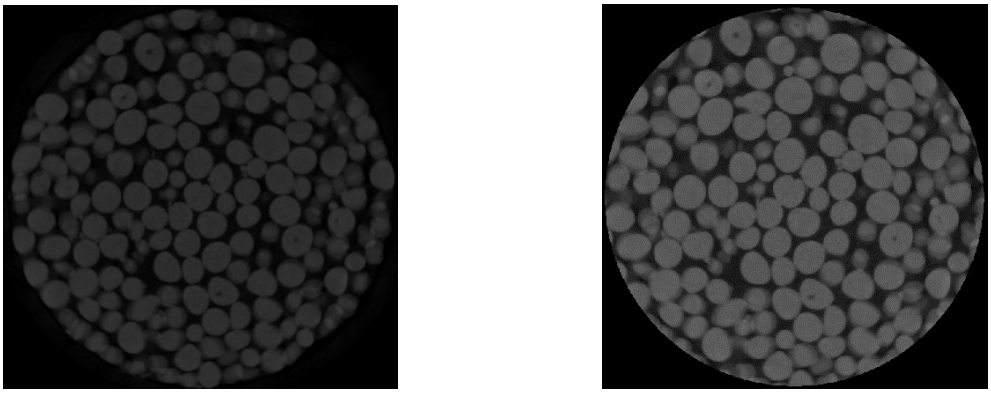

(a) (b)

Figure 3.3. (a) A 2-D CT slice of glass beads before any corrections (b) the same CT slice after circular cropping, intensity adjustment, and background noise removal

In the next step, the image is converted to a logical image (black and white image or BW image) using a threshold value. In this study, the method proposed by Otsu (1979), which chooses the threshold to minimize the interclass variance of the black and white pixels, was applied to find the best threshold to convert the image to a logical image (Appendix B). The result is as shown in Figure 3.4(a). It is noted, however, that the user can manually choose a desired threshold between 0 and 255 to separate the features by looking at the image histogram and visual inspection. It can be seen that use of a threshold alone does not separate the grain boundaries very well. Thus, and advanced image processing technique called watershed transform (Gonzalez et al. 2004; Russ 2002) with gradient is applied to segment or separate the contact points of particles. The watershed transform applies the same idea as in geography for segmentation of the gray scale images. Watershed ridgeline is the line, which separates the two connected objects. In order to apply watershed transformation to binary images, first a

transformation of the distance from every pixel to the nearest nonzero valued pixel is calculated. Once the distance transformation of the image is determined, then watershed transformation is applied. The resulting watershed image will appear as shown in Figure 3.4(b).

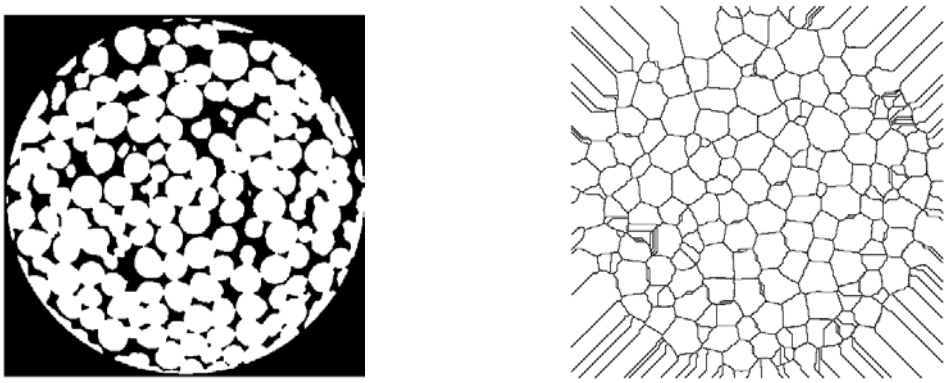

(a) (b)

Figure 3.4. (a) Converted gray scale image to a logical image using Otsu's method (b) watershed transform of the image

The watershed image is subtracted from the original image so as to give the image in Figure 3.5(a). In some cases, even with the use of watershed transform the boundaries of the particles may not be clear as is the case in Figure 3.5(a). For such cases, application of a gradient prior to using the watershed transformation is recommended. In the gradient method, the image is filtered by a 3×3 Sobel mask, which approximates vertical or horizontal gradients of the image (Gonzalez et al. 2004). In case of over-segmentation due to watershed transform as in Figure 3.5(a) in which many grains have been segmented around the boundaries and inside, the method of regional minima is

applied to remove the unnecessary segmentation within the grains (Gonzalez et al. 2004). Figure 3.5(b) is the result of the application of the regional minima algorithm to Figure 3.5(a) to fix over-segmentation. Additional details of the above standard image processing techniques are available from text books (Russ 2002; Gonzalez et al. 2004).

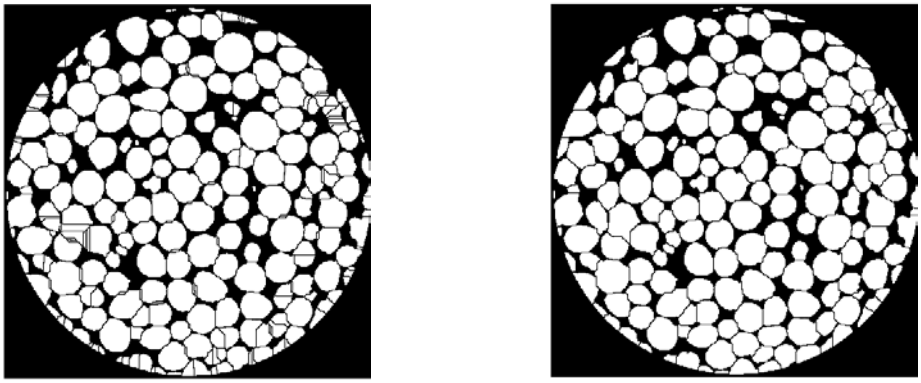

(a) (b)

Figure 3.5. (a) Segmentation of the image (over segmentation) (b) final segmentation (correction of over segmentation using regional minima)

The REV program chooses a spherical volume element whose center can be fixed anywhere within the specimen (Figure 3.6). Once the location of the center is fixed, the radius of the sphere is increased from zero to its maximum limited by the specimen boundary. The variation of porosity with the radius of volume element is plotted for each incremental step of the spherical radius.

In REV program, the user can examine the images from three different viewpoints; top, front, and right. The user can zoom (in or out) the images, find the location of each plane, the gray scale value of any voxel, and distance between different

objects on images. The output results are saved in MATLAB, and can also be exported to a spreadsheet.

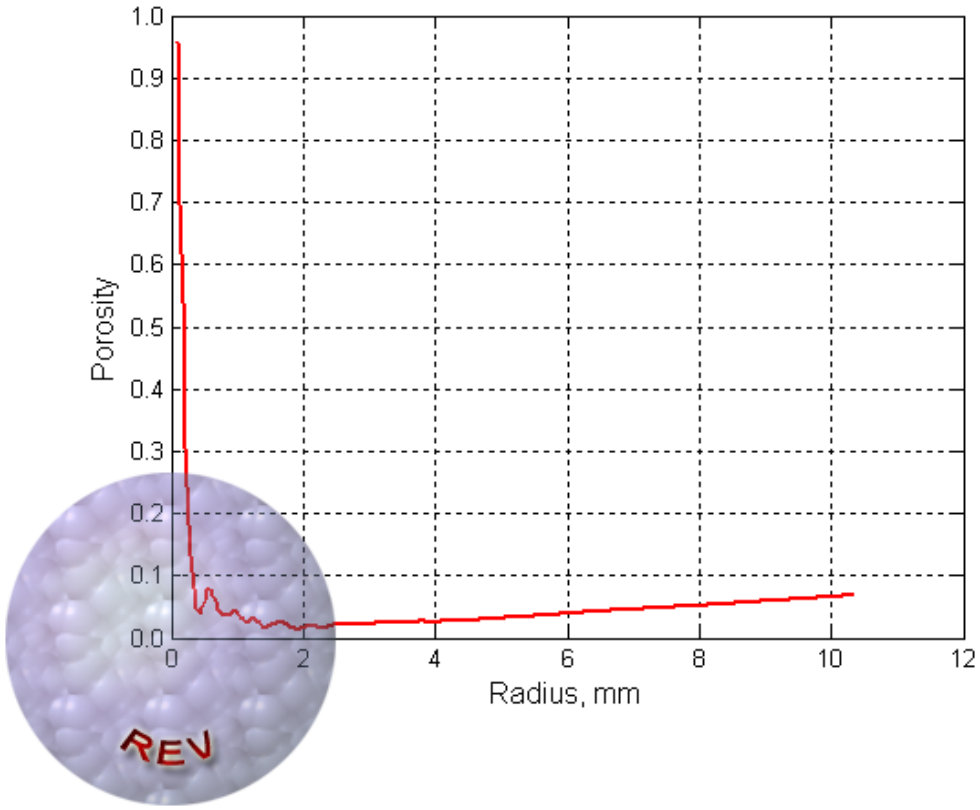

Figure 3.6. A sample plot of variations of porosity versus the radius of the spherical volume element.

3.4 Results and Discussion

Six different assemblages of 8 to 10 identical spheres with diameter *d* as suggested by Graton et. al. (1935) are shown in Figure 3.7 along with a sphere with a radius of twice the diameter of identical spheres. These basic assemblages can be fitted within the middle sphere and the pattern repeated randomly to produce a homogeneous medium. This in effect means that a basic volume element with a radius of 2 to 3 times of sphere diameters is expected to be the REV for random packing of identical spheres. It is also noted that inspection of the 3-D CT images of the glass beads specimens showed that the assemblage (α) is the dominant pattern that was repeated.

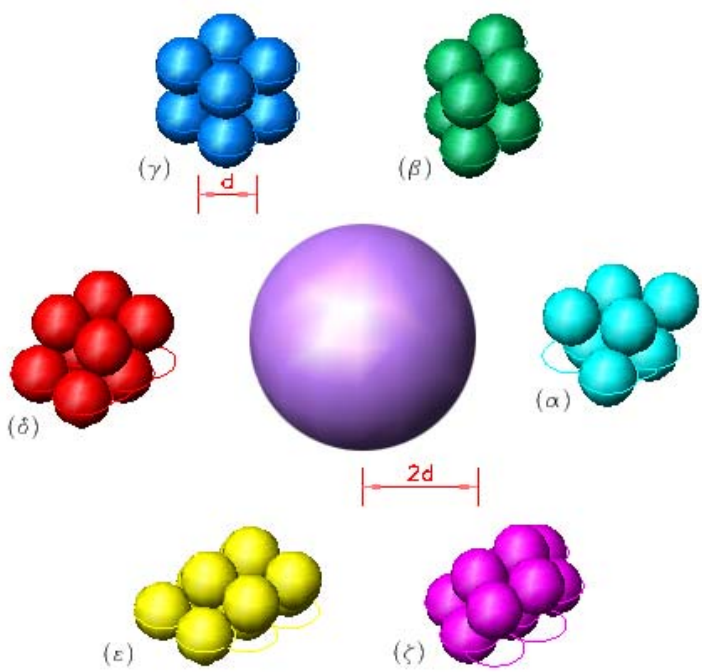

Figure 3.7. Assemblages of identical spheres with diameter *d* around a spherical volume element with a radius of *2d*. (Note, most of the observed patterns on 3-D CT images were similar to assemblage α)

Figure 3.8 shows the variation of porosity with the radius of the spherical volume element for glass beads specimens. It can be seen that the variation attains a constant value after an initial fluctuation. The specimens of glass beads are similar to identical spheres with repeated packing pattern and homogenous. The plateau in region II will continue at large radii as is evident from Figure 3.8. The normalized plot for one of the glass beads specimen (MR023GLN) with respect to the average diameter of the beads (d_{50}) is shown in Figure 3.9. It is seen that the radius of the REV is between 2 and 3 times of the average spheres diameters as expected for an assemblage of random spheres.

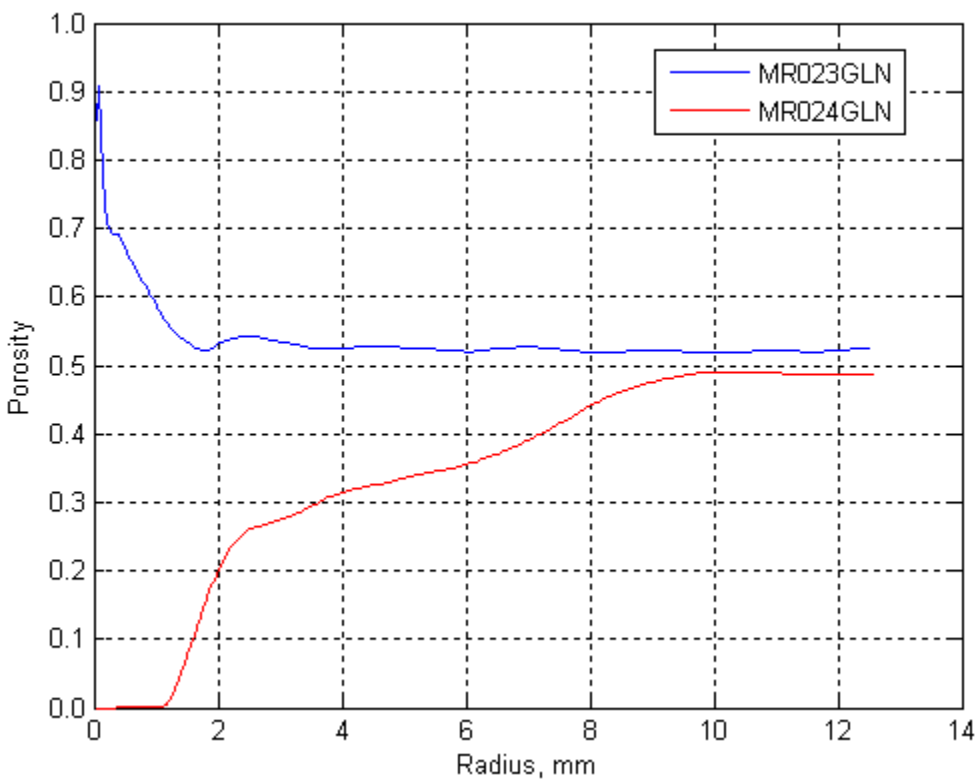

Figure 3.8. Porosity versus volume element radius for glass bead specimens

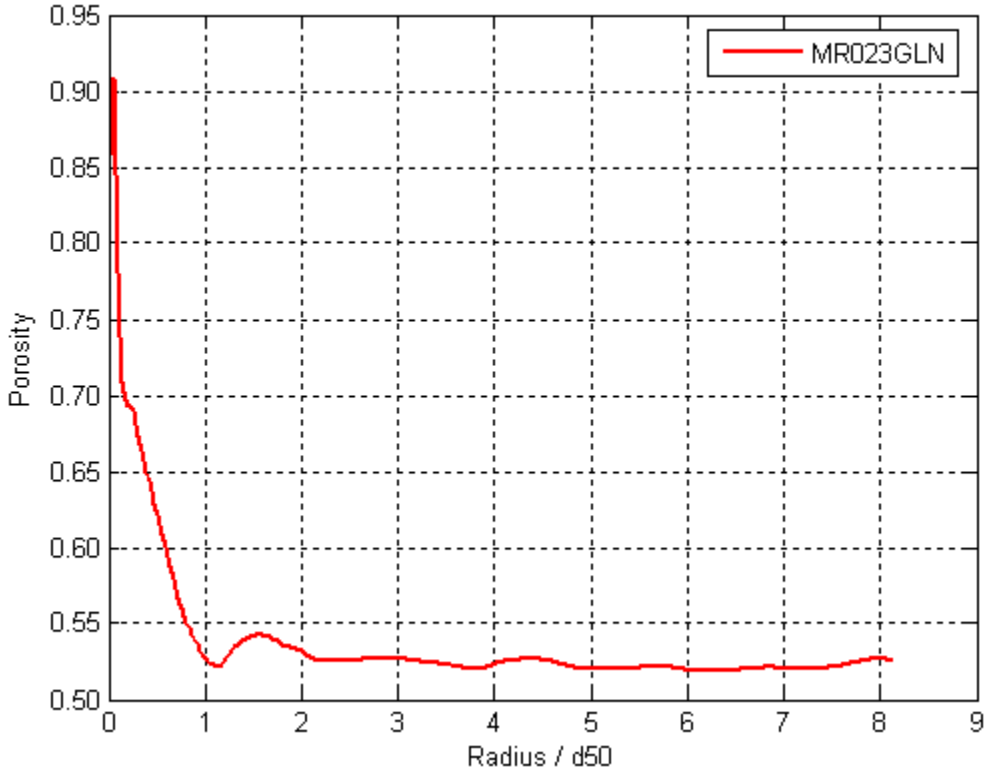

Figure 3.9. Normalized REV range to d_{50} for small size glass beads

Figure 3.10 shows the variation of porosity versus the radius of the spherical volume element for five silica sand specimens. It can be seen that the variation of the porosity of all five specimens show the characteristics of regions I, II, and III in Figure 3.1; a segment with fluctuation part at the beginning, a constant segment in the middle and a monotonically increasing segment at the end. It is also evident that the boundaries of the region are nearly the same in all of the specimens. The same trend is evident in the case of Ottawa sand (Figure 3.11) although the region III in these two materials has both an increase and a decreasing trend.

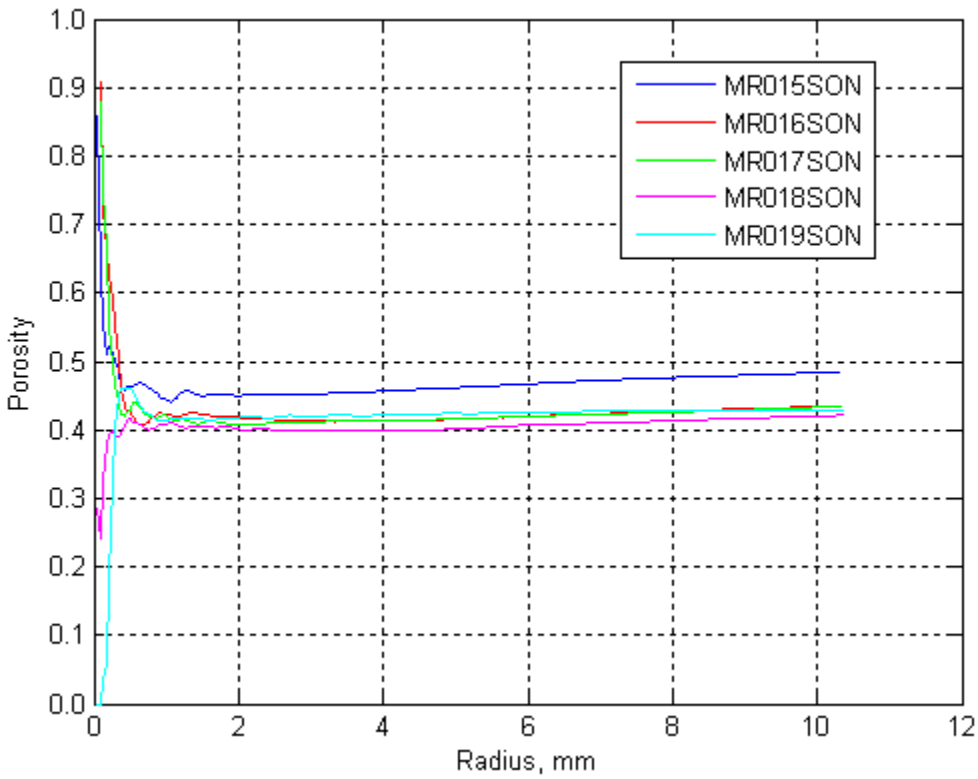

Figure 3.10. Porosity versus volume element radius for silica sand specimens

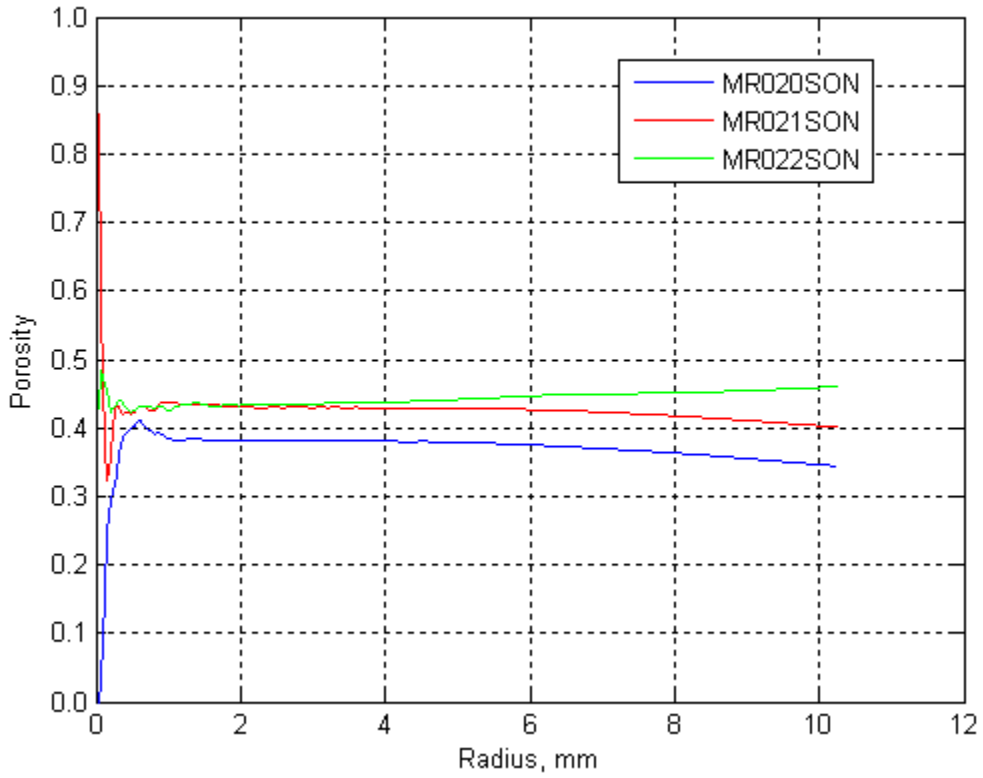

Figure 3.11. Porosity versus volume element radius for Ottawa sand specimens

Figure 3.12 shows the plot of variation of porosity respect to the normalized radius of the spherical volume element for two selected specimens of silica sand (MR018SON) and Ottawa sand (MR020SON). It can be seen that the REV radius for Ottawa sand is formed with more grains with a diameter of d_{50}. The ranges of representative elementary volume radius for all specimens are summarized in Table 3.3. Comparison those ranges with d_{50} of sand specimens shows that the ratio of the REV radius to d_{50} is about 5 to 11 times of for silica sand, 9 to 16 times for Ottawa sand, and about 2 to 3 times for uniform glass beads with random packing.

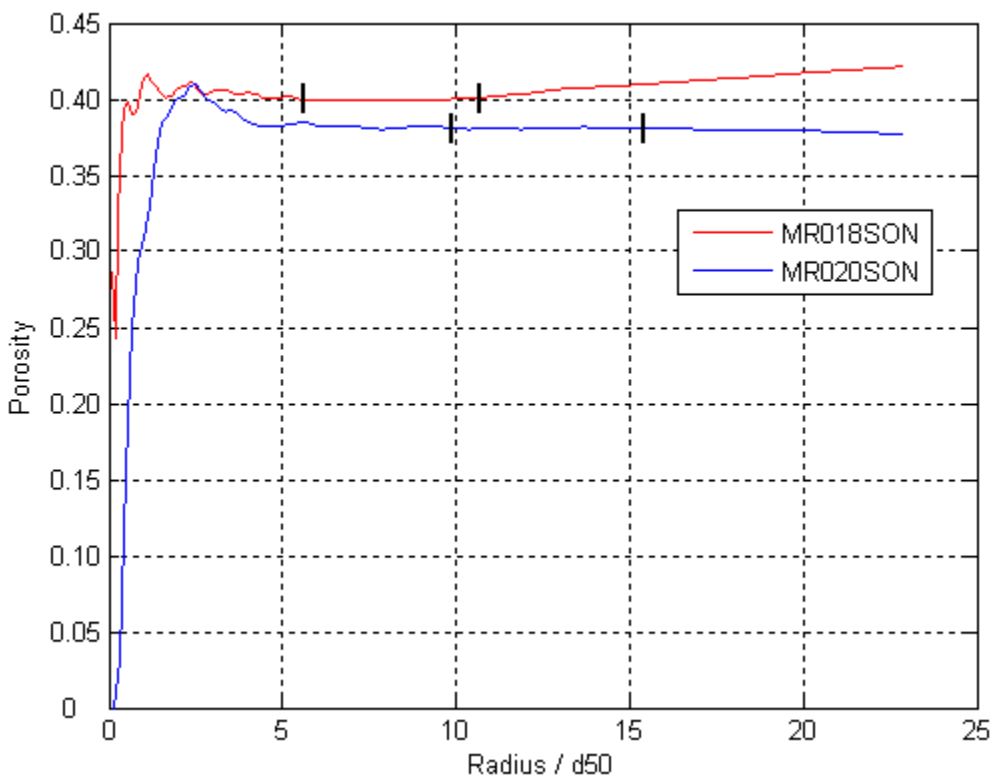

Figure 3.12. Normalized REV range to d_{50} for two selected specimens of silica sand (MR018SON) and Ottawa sand (MR020SON)

Figure 3.13 shows effect of the center location of the REV element within the specimen on the size of REV for specimen MR018SON. The location of the center of spherical volume element was changed from point A to F with the numbers within the brackets beside each letter indicating the coordinate. It can be seen that change in the location of the center of spherical volume element does not have a significant effect on REV radius. This was the case for other specimens as well.

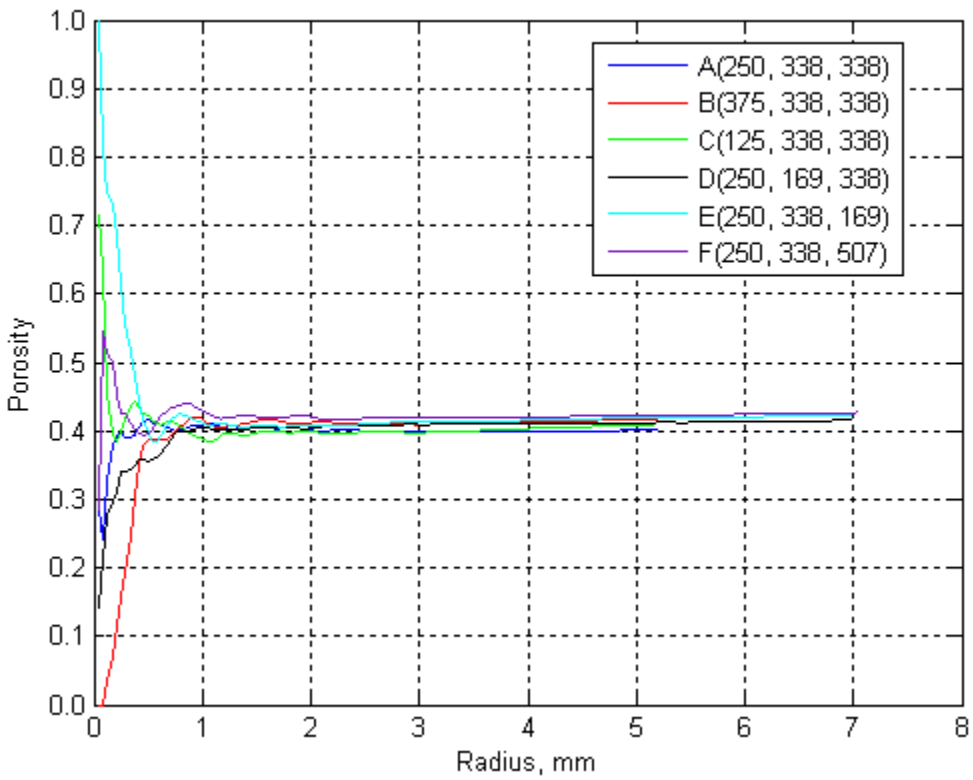

Figure 3.13. Porosity versus volume element radius for six different center locations of specimen MR018SON

The last column of Table 3.3 shows the comparison of the porosity obtained from image processing (n_{ip}) and the laboratory measured values (n_{lab}). The values compare very well. It is noted, however, that the relative error is much higher in Ottawa sand. This sand had finer grains and although the size of the finest grains of Ottawa sand specimen was larger than the resolution of the CT image, fewer pixels are used to form the image in sands with finer grains for a given magnification. This problem tends to propagate the error in processing the images and results in a higher relative error. Smaller specimens with higher magnification will reduce such error but the processing is limited by available memory.

Table 3.3. REV radius and relative errors

Type	Specimen	R_{REV} Range, *mm*	R_{REV}/d_{50} Range	n_{ip}	n_{lab}	% Error
Silica Sand	MR015SON	[2.54, 3.34]	[5.6, 7.4]	0.454	0.462	1.73
	MR016SON	[3.04, 4.66]	[6.7, 10.3]	0.412	0.405	-1.73
	MR017SON	[2.46, 3.25]	[5.4, 7.2]	0.412	0.425	3.06
	MR018SON	[2.54, 4.83]	[5.6, 10.7]	0.401	0.401	0.00
	MR019SON	[3.29, 4.26]	[7.3, 9.4]	0.422	0.444	4.95
Ottawa Sand	MR020SON	[2.63, 3.80]	[9.9, 15.4]	0.379	0.419	9.55
	MR021SON	[2.44, 3.64]	[9.9, 14.8]	0.429	0.412	-4.13
	MR022SON	[2.23, 2.73]	[9.1, 11.1]	0.435	0.451	3.55
Glass Beads	MR023GLN	[3.59, 3.70]	[2.2, 2.3]	0.543	0.550	1.27
	MR024GLN	[12.03, 12.23]	[2.0, 2.04]	0.485	0.479	-1.25

3.5 Discussion on REV

While the use of REV in developing macroscopic measures has been used widely in fluid flow and continuum mechanics applications, the existence of REV and its size has remained conjectural. It has never been identified systematically in real media in the past. This study presents a unique technique to quantify the characteristics of

representative elementary volume in granular materials. It makes use of the X-ray computed tomography imaging techniques to examine the presence of REV.

An interactive 3-D image-processing program was developed to process the 3-D CT images and choose the REV. The effect of the shape and size of the particles, specimen porosity, and location of the REV center were examined in this study using different specimens of spherical glass beads, silica sand and Ottawa sand. The results show three different characteristic regions: a microscopic fluctuation region, constant region, and monotonically increasing/decreasing region.

The REV radius for the glass beads specimens and random packing is found to be 2 to 3 times of the identical average sphere diameter. The radius for silica sand composed mainly of elongated particles is between 5 to 11 times of d_{50}, and for Ottawa sand composed mainly of subrounded particles is between 9 to 16 times of d_{50}. These values appear to justify the use of 10 to 20 diameters of sand grains adopted in some studies. The fact that the radius of REV appears to decrease with elongation and angularity leads us to believe that interlocking may be a contributor in determining its size.

The proposed method is general and it can be applied for any granular or perforated material if the void sizes are more than the maximum CT image resolution. However, at the present time the maximum specimen size is limited to the capabilities of the X-ray CT equipment and available memory to process the image.

On a final note, in view of its usefulness, the concept of REV relating to numerical modeling and selection of specimen size for laboratory tests has been debated recently. As discussed in the introduction, it is necessary to realize that the REV concept

is useful for obtaining average properties of a homogenous medium. On the other hand, element tests on natural media inevitably encounter heterogeneity and the classical continuum hypothesis breaks down. In this case, the size of REV becomes scale-dependent. One may define a REV size for a specific sized specimen in a laboratory-scale problem but this may not be applicable to larger sized specimens or field-scale problems, where heterogeneity at several scales exists. Additional non-local continuum measures are needed to fully describe scale effects in such heterogeneous media (See Al Hattamleh et al. 2003).

Chapter 4

X-RAY CT TRIAXIAL SYSTEM

4.1 Introduction

The triaxial device is widely used in geotechnical practice to find the stress deformation properties of soil. A conventional triaxial apparatus includes a transparent Perspex cylindrical cell, a pump to apply confining pressure, a system to apply axial compressive or tensile load, volume measuring devices, pore pressure transducers, and micro-processor data acquisition unit. The different components of a typical triaxial system are shown in Figure 4.1.

Figure 4.1. Triaxial system

However, use of the conventional triaxial system, especially the cell and loading arrangement inside the X-ray CT chamber is impractical. Thus, a new design is needed to enable simultaneous measurements of microstructure changes with shearing. The design of a new triaxial apparatus for use with the X-ray CT system at Washington State University is presented in this chapter.

4.2 Characterization of the Soil Microstructure using Triaxial Apparatus

The soil specimen must be simultaneously scanned using X-ray CT while it is subjected to shearing in order to develop 3-D images of soil microstructure and its evolution. This process suffers from the following limitations.

1. There is only limited place available within the X-ray CT shield cabinet. This is not sufficient to place a triaxial device. Furthermore, the diameter of the object placed on the rotary stage of X-ray CT system at WSU is limited to a maximum of 50 cm.
2. Steel rods around a conventional cell prevent X-ray from penetrating into the specimen. This would result in CT images of the specimen that are defective for processing. The CT image of a soil specimen obtained using a conventional triaxial cell is as shown in Figure 4.2. It is evident that the image is not good for processing.
3. The total weight on X-ray CT system at WSU rotary stage is limited to 500 N.

Therefore, in order to perform real time monitoring of microstructure, a new triaxial system was designed to meet the above limitations. Such design is much dependent on the specifications of X-ray CT system, load limitations, and cost.

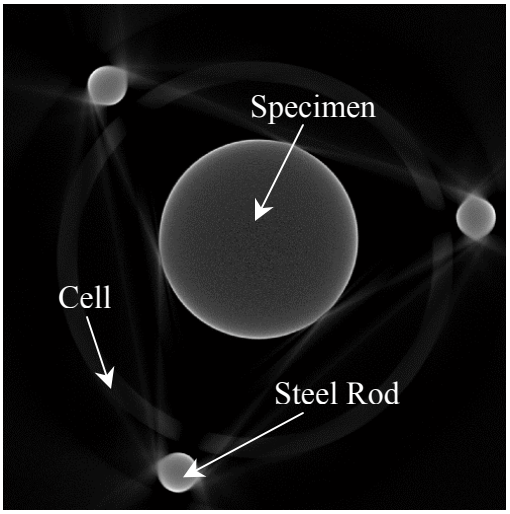

Figure 4.2. A CT slice of a soil specimen in a conventional triaxial cell (Details of the specimen image are not clear.)

4.3 Development of a Novel X-Ray CT Triaxial Apparatus

The past few years have seen significant advances in developing high strength X-ray transparent materials such as glass reinforced plastic (GRP) that has tensile strength as much as twice that of grade 50 steel (Dagher et al. 1997). Glass reinforced plastic also is a good material that resists hoop stress. This coupled with the advent of small but powerful loading systems enable us to design a triaxial cell that avoids the use of steel rods using GRP.

The loading frame of conventional triaxial system is replaced with a small loading jack attached with tension bars on top of the cell (Figure 4.3). This way, the applied compressive force by the jack is counter balanced by the tensile forces developed in the tension bars (Figure 4.4). Further, the internal cell pressure does not generate any external force; thus, the only applied force on the CT stage is the weight of the triaxial apparatus.

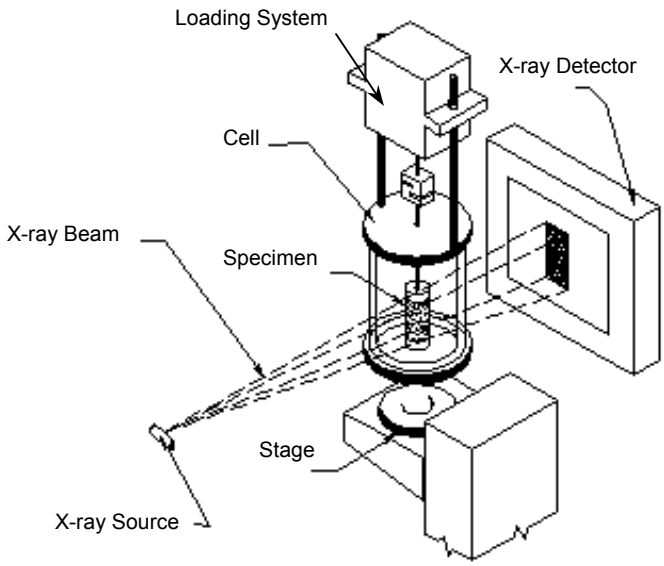

Figure 4.3. Schematic of the modified X-ray CT triaxial device

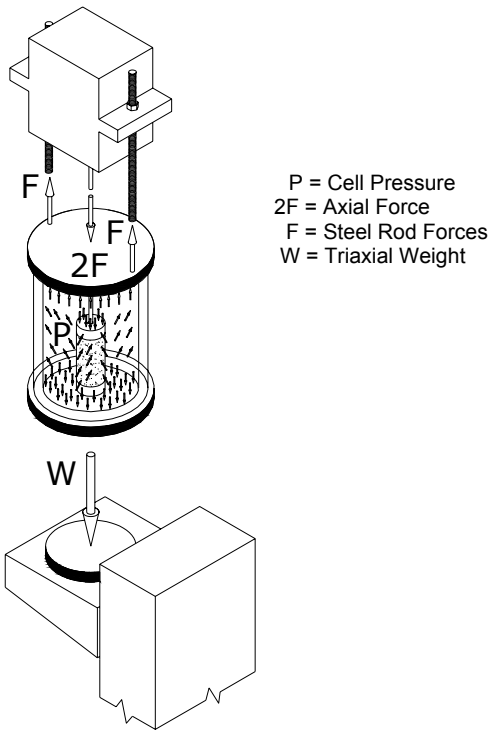

Figure 4.4. Force diagram of the triaxial apparatus

It is noted that Otani et al. (2001) have developed a similar triaxial device for use use with their X-ray CT. However, its capability is limited to specimen size, axial load, and cell pressure less than 50 mm × 100 mm, 1 kN, 400 kPa, respectively.

4.3.1 Design Requirements

The design requirements for the new system are as follows:

I. Maximum enclosure box dimensions: 50 cm ×50 cm at base and 100 cm in height
II. Maximum axial load: 10 kN
III. Maximum cell pressure: 400 kPa
IV. Maximum specimen size: 150 mm × 170 mm
V. Total weight: 500 N
VI. Computer control loading system and data acquisition
VII. Total cost: less than $30,000

4.3.2 Design Feasibility Based on Finite Element Analysis

An analysis of the triaxial device was performed using a general finite element analysis program (NISA[1]-II) followed by a series of extensive stress-strain analyses to ensure the feasibility of the design. Acrylic cell, aluminum base, soil specimen, aluminum load cap, and aluminum top end plate were modeled using 8 node solid elements. Applied loads constituted of the weight of the system, internal pressure, axial load on the specimen, and reactions of the tie rods on top of the cell. Zero vertical displacement boundary conditions were applied to the nodes along the very bottom

[1] NISA: Numerical Integrated Systems Analysis of elements (A family of general and special purpose finite element modeling and analysis programs for PCs, workstations, and supercomputers by Engineering Mechanics Research Corporation, Troy, Michigan)

nodes. A series of linear elastic analysis for the maximum design axial load (10 kN) and maximum internal pressure (400 kPa) were performed to investigate design feasibility and then to obtain the cell thickness. Figure 4.5 shows the finite element model of the cell. The corresponding von-Mises stress contours on the cell for the applied load conditions are shown in Figure 4.6. It is evident that the von-Mises stress values within the acrylic cell are less than 10 MPa (1.5 ksi) and it is even much less than acrylic tensile strength of 47-79 MPa. Note that though stress values are low, small elastic modulus of the acrylic (2 GPa) tends to have large strains, which does not allow increasing the load or cell pressure more than the design requirement values in this study. Based on the finite analysis, it was found that such that design is feasible and a wall thickness of 5 cm is sufficient for the cell to resist against the combined biaxial stresses. For cases involving higher loads, a new system is needed. Details of such a system are provided in Appendix C.

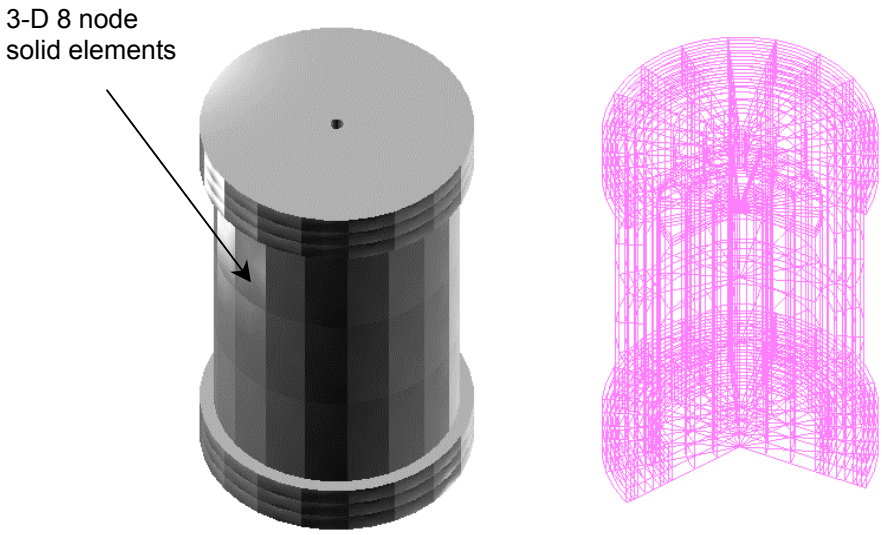

Figure 4.5. Finite element model of the triaxial cell

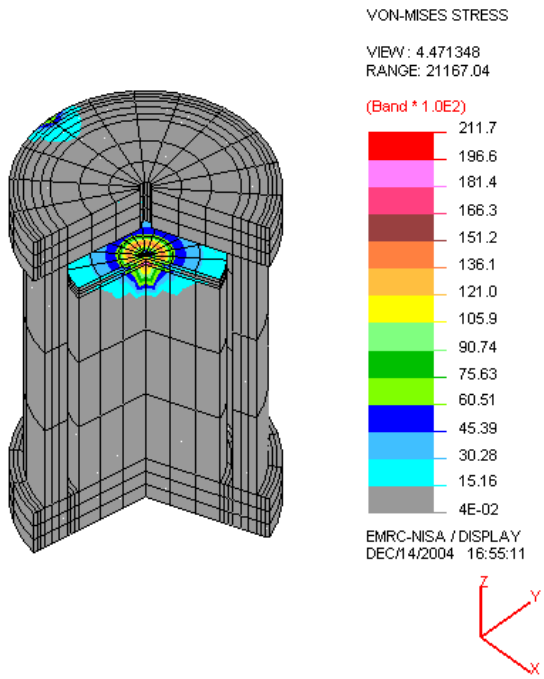

Figure 4.6. Selected Von-Mises stress contours for the maximum design load (psi) using an acrylic cell

Modified axial deformation is calculated by subtraction elongation of the cell and cell piston displacement. Using GRP materials instead of acrylic for the cell, allow increasing axial load and internal pressure dramatically.

4.3.3 X-ray CT Triaxial Components

A very small electronic loading jack, called GeoJac, provides an axial load up to 10 kN. Cell pressure is generated by an air compressor, and is regulated to the desired level using a component called DigiFlow. Both loading and data acquisition are controlled by a computer to minimize the human error. Figure 4.7 shows different components of the triaxial system that is under development by Trautwein Geotechnical Testing Instruments Company based in Houston, Texas.

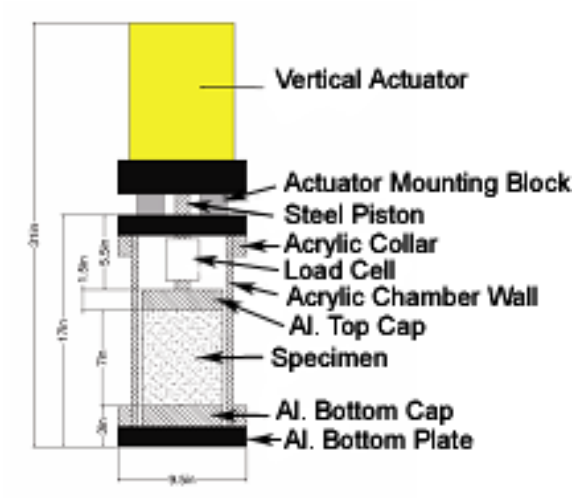

Figure 4.7. Schematic drawing of triaxial manufactured by Tratwein

Chapter 5

DETERMINATION OF 3-D INTERNAL DISPLACEMENT FIELDS

5.1 Introduction

Shear bands in granular materials are generally formed along three dimensional surfaces. Detection of the shape of such these surfaces, and internal displacement fields especially in the neighborhood of shear bands is important to characterize its features. Shape of the shear bands may be observed and photographed directly for simple cases such as plane strain problems. Use of small colored particles aids in the detection of the shape of shear bands easier, though some disturbance and a change in material properties is expected. X-ray CT can provide a 3-D image of the specimen and as such it is useful to detect shear band characteristics, nondestructively.

Use of easily detectable material as markers, such as colored sand or tiny metallic spheres is commonly used to find internal displacements. Colored sand layers are usually used behind a transparent sheet and the movement of the colored particles is traced from photographs that are taken continuously as the specimen is loaded. On the other hand, instead of markers, a rectangular grid, made of horizontal and vertical lines, is plotted on the transparent sheet and the displacements of the grains are obtained by tracing the relative movement of the particles respect to the grid lines (White and Bolton 2004). Particle image velocimetry (PIV), which is a technique to find instantaneous 3-D velocity vector in a flow field, is applied to obtain the displacements. This technique has been shown to predict displacement fields for large scale tests with a negligible error.

However, its application is limited to the displacements of the particles located only on the exterior boundaries. Very small metallic balls or wires have also been placed inside the specimen at certain locations to quantify the internal displacement fields using radiography or X-ray CT (Nemat-Nasser and Okada 2001; Wood 2002; Alshibli and Alramahi 2006). Disturbance and changes in material properties limit the calculation of 3-D displacements to only small number of points by this method.

Several different methods using image processing and computer vision techniques have been developed to quantify the 2-D displacement fields. The cross-correlation method remains most popular among them. In signal processing cross-correlation number is a measure that shows the similarity between two signals. It can also be used to compare the similarity between two digital images before and after applying displacements. The image before applying displacements is called the reference image and the image after applying displacements is called the current image. The principles of the cross-correlation technique to find the displacement fields rely on selecting a small rectangular region of the reference image as template and then finding another rectangular region with the same size on the current image as target with the maximum similarity or with the maximum cross-correlation. The displacement is obtained by subtraction of the distance between the central points of template and a target with maximum similarity with the template.

Sadek et. al (2003), Liu and Iskander (2004), and several other researchers applied cross-correlation technique to find the 2-D displacement fields on the exterior boundaries of soil specimens. This method has not been applied for 3-D X-ray CT

images due to some difficulties such as fluctuations of X-ray intensity with time, large sizes of 3-D images, and extremely long processing time.

In this chapter the cross-correlation technique is extended to three dimensions and practical methods are developed to obtain 3-D displacement fields from successive 3-D X-ray CT images. An interactive computer program (M-DST) is developed to determine the 3-D displacement fields using those techniques.

5.2 Cross-Correlation Technique for Pure Displacements

Any X-ray CT image can be represented by a discrete function $F(X_i)$, which maps point $X_i(x_i,y_i,z_i)$ in 3-D Euclidean space to $F(X_i)$ or image intensity at point X_i. To determine the internal displacement fields between two successive X-ray CT images, at times t, and $t+\Delta t$, the image at time t is considered as template or reference image, $F(X_i)$ and the image at time $t+\Delta t$ is considered as target or current image $G(X_i)$. A small box shape subvolume is taken from the current image $F(X_i)$, which is represented by $f(X_i)$. It is assumed that after applying a displacement d_i (with three components u_i, v_i, w_i in x, y, and z directions, respectively) to $f(X_i)$ there is another box shape subvolume with the same size of the template in the current image like target $g(X_i)$, which is the same as $f(X_i)$, i.e.,

$$g(X_i) = f(X_i - d_i) \tag{5.1}$$

However, in practice finding a target exactly the same as the template is nearly impossible due to several issues such as the fluctuation of X-ray with time, particle rotation, and noise. Therefore, Equation 5.1 is modified by an additional term to compensate for these issues. This additional term is usually added to the template as a remainder like $\eta(X_i)$:

$$g(X_i) = f(X_i - d_i) + \eta(X_i) \tag{5.2}$$

In order to find d_i, first the maximal correlation coefficients of g and f are defined as (Haralick and Shapiro 1993):

$$\frac{Cov[f(X_i - d_i), g(X_i)]}{\sqrt{Var[f(X_i - d_i)].Var[g(X_i)]}} = \frac{\sigma_{fg}(d_i)}{\sigma_f(d_i)\sigma_g(d_i)} \tag{5.3}$$

where:

$$\sigma_{fg}(d_i) = \frac{1}{m-1}\left[\sum_{i=1}^{m} f(X_i - d_i)g(X_i) - \frac{1}{m}\sum_{i=1}^{m} f(X_i - d_i)\sum_{i=1}^{m} g(X_i)\right] \tag{5.4}$$

$$\sigma_f^2(d_i) = \frac{1}{m-1}\left[\sum_{i=1}^{m} f^2(X_i - d_i) - \frac{1}{m}\left(\sum_{i=1}^{m} f(X_i - d_i)\right)^2\right] \tag{5.5}$$

$$\sigma_g^2(d_i) = \frac{1}{m-1}\left[\sum_{i=1}^{m} g^2(X_i) - \frac{1}{m}\left(\sum_{i=1}^{m} f(X_i)\right)^2\right] \tag{5.6}$$

where m is the number of voxels in each image.

Cross-correlation function similar to Equation 5.3 can also be obtained using the square Euclidean distance between f and g, $\alpha^2_{f,g}$, as follows:

$$\alpha^2_{f,g}(d_i) = \sum_{i=1}^{m}\left[g(X_i) - f(X_i - d_i)\right]^2 \tag{5.7}$$

Expanding $d^2_{f,g}$:

$$\alpha^2_{f,g}(d_i) = \sum_{i=1}^{m}\left[g^2(X_i) - 2g(X_i)f(X_i - d_i) + f^2(X_i - d_i)\right] \tag{5.8}$$

If the square terms in Equation 5.8 are approximately constant then the remaining term (cross-correlation) is a measure of the similarity between f and g:

$$c(d_i) = \sum_{i=1}^{m} g(X_i)f(X_i - d_i) \tag{5.9}$$

where $c(d_i)$ is cross-correlation coefficient as a function of displacement.

Application of above cross-correlation function to find displacements has several disadvantages (Lewis 1995). For example:

- If $\sum_{i=1}^{m} g^2(X_i)$ (image energy) varies with position, the matching algorithm based on Equation 5.9 fails, because the square terms in Equation 5.8 were assumed approximately to be constant.
- The range of the cross-correlation function depends on the size of the template.
- Equation 5.9 is not invariant with changes in image amplitude such as those caused by changing X-ray conditions across the image sequence.

To overcome the above problems, the cross-correlation function is normalized to unit length (Lewis 1995):

$$NCC(d_i) = \frac{\sum_{i=1}^{m}\left[g(X_i) - \overline{g}\right]\left[f(X_i - d_i) - \overline{f}\right]}{\left(\sum_{i=1}^{m}\left[g(X_i) - \overline{g}\right]^2 \sum_{i=1}^{m}\left[f(X_i - d_i) - \overline{f}\right]^2\right)^{0.5}} \tag{5.10}$$

where:

$NCC(d_i)$ = normalized cross-correlation as a function of displacement d_i

$\overline{f}$ = average of template f

$\overline{g}$ = average of target g

The above equation is referred to as the normalized cross-correlation function. Both correlation coefficients from Equation 5.3, and Normalized cross-correlation function from Equation 5.10 ranges from -1 to +1, in which +1 shows 100% similarity between template and target or both are the same; 0 means no similarity and -1 shows 100%

similarity in the reverse direction. In any case, the maximum absolute value resulting from Equation 5.3 or Equation 5.10 is always considered to compare two images. Finally, the displacement d_i is calculated as follows:

$$d_i = X_{cg}^{\max} - X_{cf}^{i} \tag{5.11}$$

where:

$X_{cg}^{\max}$ = Cartesian coordinates of the target central point so that the correlation coefficient or cross-correlation function is maximum

X_{cf}^{i} = Cartesian coordinates of the template central point

5.2.1 Determination of 3-D Displacement Fields

The reference image is divided to small box shape subvolumes to find the displacement fields using cross-correlation techniques. The size of the subvolumes depends on many different factors such as image size, available computer memory, and accuracy. Then for each template f in the reference image F a target g in the current image G is searched so that the correlation coefficient (Equation 5.3) or normalized cross-correlation (Equation 5.10) is maximal. The displacement d_i is determined based on the maximum similarity between two blocks using Equation 5.10. In case of significant rotations different orientations of the target must be examined to include the effect of affine deformation (displacement and rotation). This is done by using optimization techniques or robust statistical methods (Clocksin et al. 2002). However, for small rotations, rotation of the target blocks may be neglected to reduce processing time.

In order to illustrate the application of this technique, the displacements of a 3×3×3 block (template) in a 4×4×4 volume (reference) for a movement of 1 unit in X, Y, and Z directions are determined. Figure 5.1 shows the reference image left and the current image on the right. The numbers in each voxel show the image intensity at that point. The 3×3×3 template block in the lower left corner in the template has been moved to the upper back right corner in the current image.

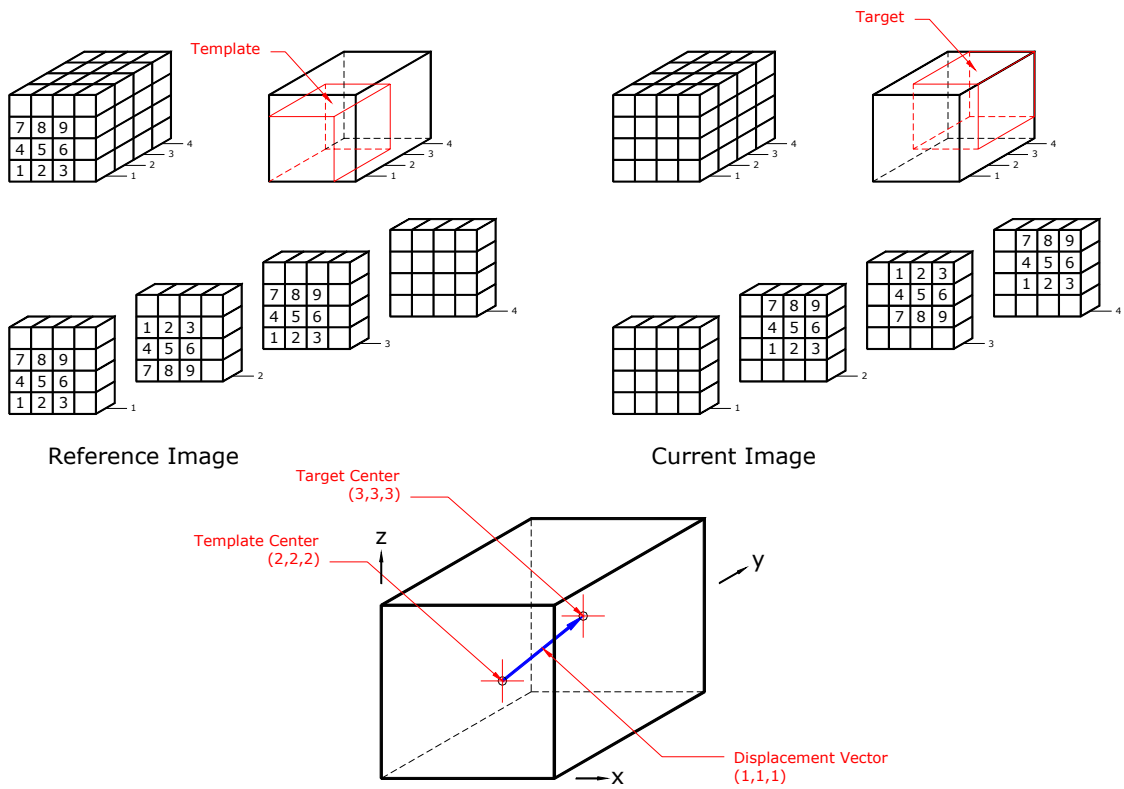

Figure 5.1. Determination of displacements of a 3×3×3 block in a 4×4×4 volume

Normalized cross correlation (NCC) values for the template and all possible targets are calculated using either Equation 5.3 or Equation 5.10. Each time the moving block center is located at a voxel of the target to examine all voxels in the target, which

are 64 in this example. Elements of the moving block, which are placed outside the target, are filled with zeros (zero padding) and maximum of the absolute values of NCC is found. Figure 5.2 shows the plot of NCC values at every voxel of the target. This plot has a maximum of 1 at element (voxel) number 42 corresponding to a point with Cartesian coordinates of *(3,3,3)*. Cartesian coordinates of the selected block in the template is *(2,2,2)* and the displacements are obtained by subtracting those block center coordinates using Equation 5.11, which are 1, 1, and 1 in X, Y, and Z directions, respectively.

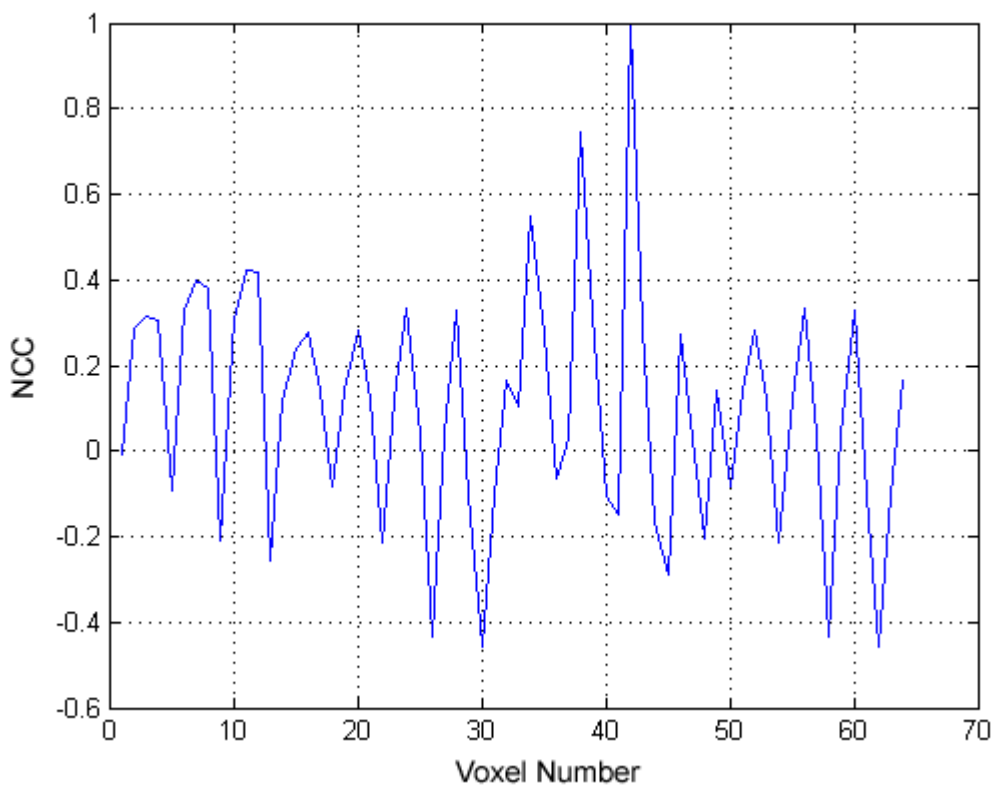

Figure 5.2. NCC values at every voxel of the current image

5.2.2 NCC Issues and Solutions

There are several issues with NCC that need to be resolved before programming the method:

1. X-ray intensity fluctuates, whereas the main assumption in NCC is to use the same X-ray intensity for both reference and current images.
2. NCC is not invariant and for the repeating patterns and affine deformation the results may fail or incur large errors.
3. As shown in the last example, for every block in the template all the voxels in the target must be examined. Thus NCC technique is extremely time consuming. For a $M \times N \times P$ voxel reference image and a $Q \times R \times S$ voxel current image, NCC is calculated $M \times N \times P \times Q \times R \times S$ times. For instance for a $300 \times 300 \times 500$ voxel reference image and the same current image size, NCC is calculated 2.025×10^{15} times to find the displacement at every voxel. Besides, several times this number is needed for the total suite of operations. It means that several months are needed to process this single problem on personal computers with the fastest CPU at the present time (about 4 *GHz*).

The following solutions are provided as the solutions to overcome the issues:

1. Use of the average of several different frames (X-ray snap shots) for each single digital radiograph and increasing the number of averaged frames smoothes the X-ray intensity fluctuation so that it can be assumed constant intensity with a good accuracy.

2. Displacements on soil specimens can be applied in small steps. When a fixed axis test such as triaxial is used the rotation of the blocks are small as well. Sand particles are irregular in shape, which means that no repeating pattern is expected for an image with sufficient resolution to separate the particles.
3. When there is no information about displacements all the voxels in the current image should be searched. Displacements of the blocks may be estimated based on the external radial and axial displacements. Therefore, to reduce the processing time a subvolume around a particular block from target is extracted to search for the maximum NCC within that small subvolume. Use of fast NCC algorithms by expanding both numerator and denominator of Equation 5.3 or Equation 5.10 (Lewis 1995; Eaton 2005), reduces the processing 20 times and even more. Finally, use of parallel processing is recommended to further reduce the processing time.

5.3 An Interactive Computer Code to Find 3-D Displacement Fields

An interactive computer code (M-DST) was developed to find the displacement fields by comparing template and target images using NCC technique in MATLAB environment. Figure 5.3 shows M-DST flowchart. M-DST can load 3-D X-ray CT images from different sources; from output of the visualization program (FlashCT-VIZ), from horizontal X-ray CT slices, and from a 3-D array stored as a MAT files. The program takes advantage of successive data write and read on the hard disk drive to process large volumes. In this way only the necessary portion of the image is loaded from hard disk drive to the random access memory (RAM). After completing the operations, the results are saved on the hard disk drive and deleted from RAM to provide sufficient

free space for the next image portion. The user can extract a subvolume from the reference image to limit the calculations to certain voxels. Displacement fields may be determined using three different methods; fast NCC using running sum, direct determination of NCC, and spatial correlation (inverse Fourier transform of the product of the transform of one function times the conjugate of the transform of the other). To ensure that the similar blocks are selected, the displacements between the blocks take in to account only when the maximum value of NCC is more than a similarity threshold. A similarity threshold about 95% gives acceptable results for most applications.

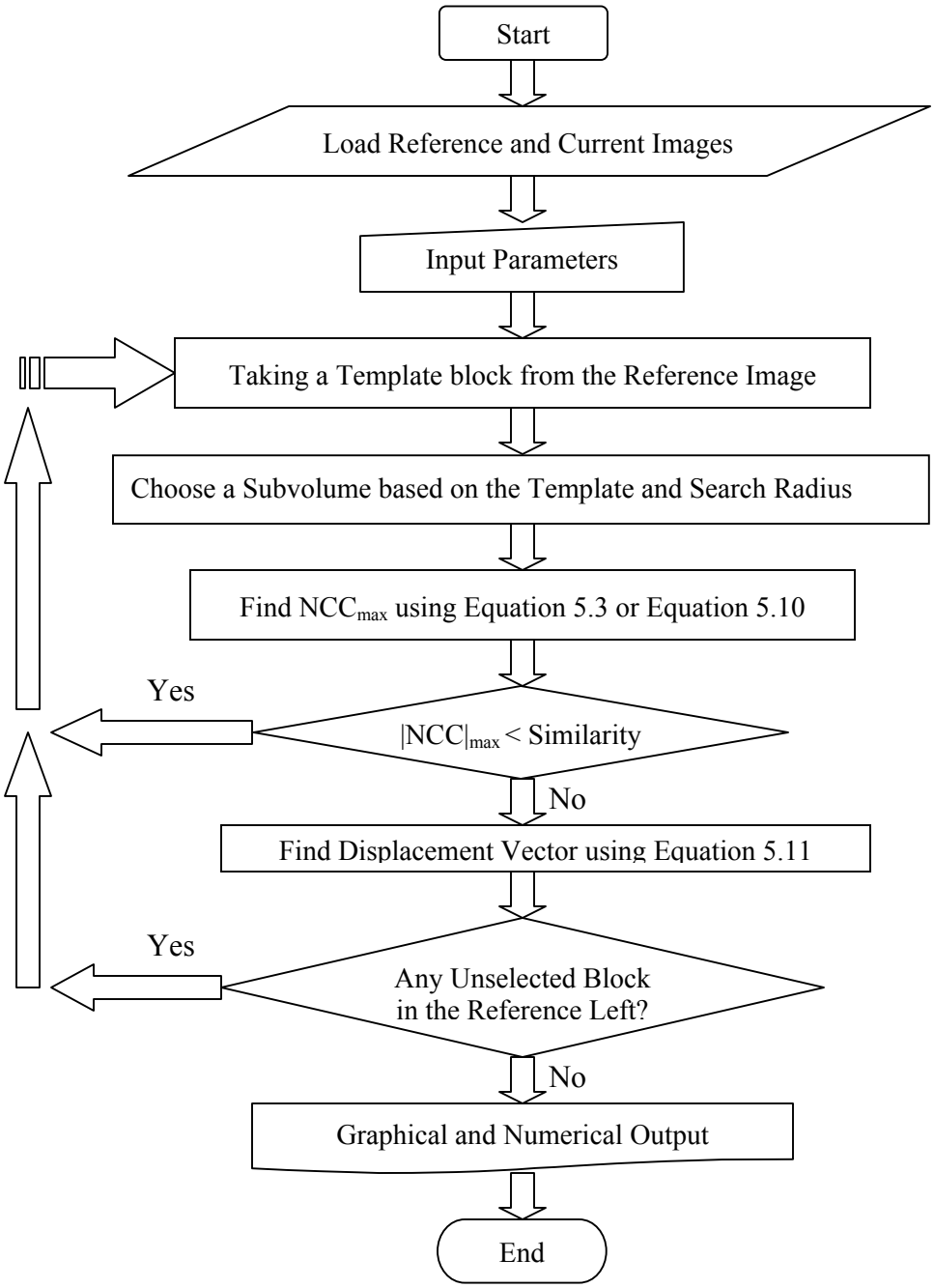

Figure 5.3. M-DST flowchart

It is recommended to reduce this number to 70% in case of significant rotations, unless rotation is included using optimization. However, reduction of the similarity threshold means reduction of accuracy but less processing time.

5.3.1 Verification of the Computer Code

Different tests were used to verify the computer code. In the first, the current image is generated by applying known displacements to the reference image. Then the displacements of the reference image are determined by the program and the results are compared. Figure 5.4 shows the displacement fields of a 3-D X-ray CT image after a translation of 3, 3, and 5 pixels in X, Y, and Z directions (The volume size is 337×337×246 voxels and the total processing time on a 3.2 GHz Pentium IV machine is about 17 hours. In this particular problem template size is 35×35×35 voxels, search radius is 60 pixels and the displacements are determined for 20 voxels intervals with 100% similarity threshold). The results of M-DST are exactly the same as imposed displacements. To check the program for larger displacements, the 3-D X-ray CT image is translated 10, 10, and 20 pixels in X, Y, and Z directions, respectively. The results are shown the Figure 5.5, which are identical to the imposed displacements. (To reduce the processing time, the search radius is reduced to 25 pixels and the displacements are determined for 35 voxels intervals. The other parameters in the program are kept unchanged. These changes reduce the processing time significantly to 00:48:38 hours using the same machine.)

In case of rotation of template blocks, M-DST determines rotation pattern correctly, but there is a significant error in displacement values. For instance the results of the 3-D X-ray CT image for a rotation of 5° (counter clockwise) around Z axis for 70% similarity threshold are shown in Figure 5.6. In this case M-DST could not find any template and target blocks to have a similarity more than 95%. It means that for

significant rotations considerable error is expected, though pattern of the displacement fields seems to be valid.

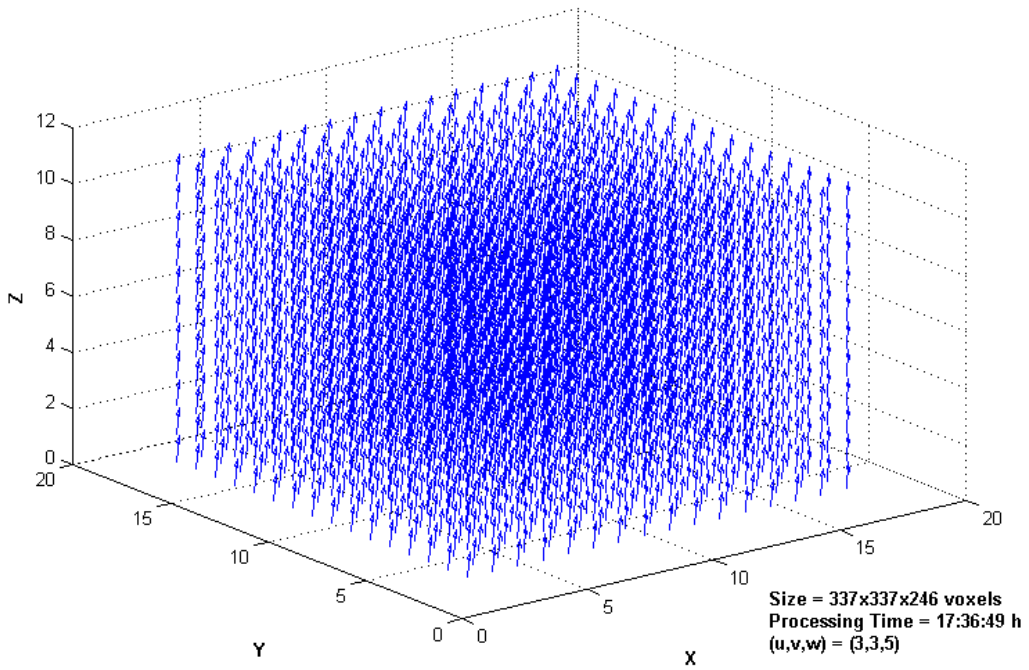

Figure 5.4. Determined 3-D displacement fields for imposed displacements of 3, 3, and 5 pixels in X, Y, and Z directions, respectively (search radius is 60 pixels)

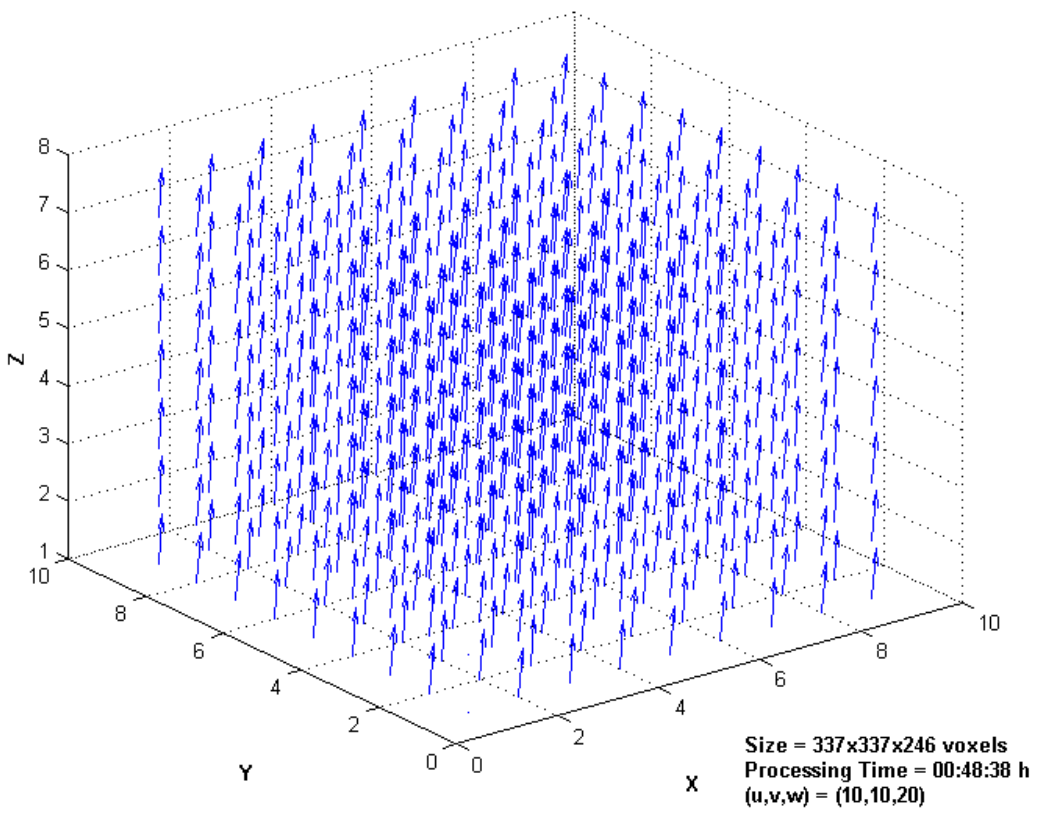

Figure 5.5. Determined 3-D displacement fields for imposed displacements of 10, 10, and 20 pixels in X, Y, and Z directions, respectively (search radius is 20 pixels)

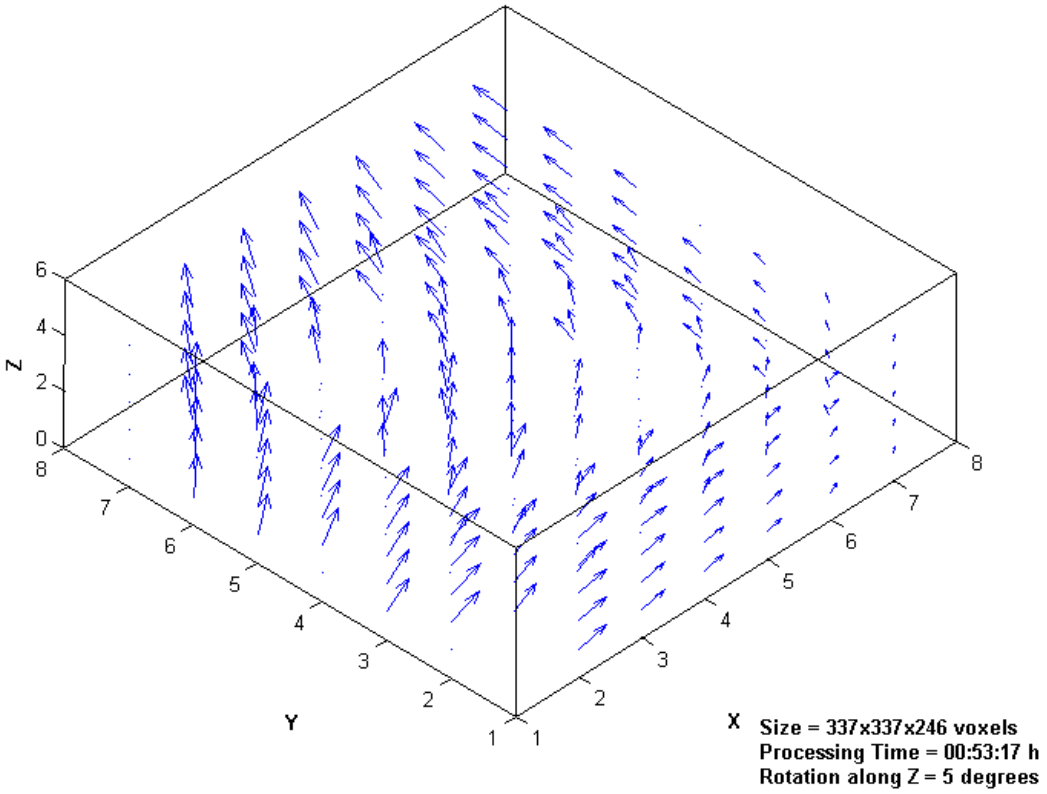

Figure 5.6. Determined 3-D displacement fields for imposed rotations of 5° along Z axis using 70% similarity threshold

Chapter 6

CHARACTERIZATION OF THE 3-D DISTRIBUTION OF LOCAL POROSITY

6.1 Introduction

Due to the large dilatancy, extremely large voids are produced within shear bands (Oda and Kazama 1998). Accordingly, a sudden jump in distribution of local void ratio (or porosity) can be used to detect shear bands (Alshibli et. al 1999; Batiste et. al 2004; Oda et. al 2004). Most past studies have used the local porosity distribution based on 2-D images to detect shear bands. Porosity and void ratio are parameters defined for 3-D volume and determination of these parameters from 2-D images results in errors. Therefore, it is evident that the local porosity distribution from 3-D images would provide a better description of shear band formation. In this study a method is developed to find the 3-D distribution of local porosity. A computer code is also developed to find the 3-D local porosity distribution and to plot the 3-D local porosity contours in three different planes, XY, YZ, and XZ.

6.2 Image Characterization and 3-D Local Porosity Distribution

The same procedures as described in section 3.3 are applied for image enhancement, noise removal, and segmentation in order to find the 3-D distribution of local porosity. Local porosity is defined as the ratio of the void volume to the volume of a small subvolume. The shape and size of the subvolume are in general chosen in a

somewhat arbitrary manner. It is preferred to do the calculations for a box shaped subvolume here. Numerical calculations based on void ratio become unstable if there is no solid particle within the selected subvolume. Thus, porosity instead of void ratio is monitored.

A new computer code is added to M-REV program (section 3.3) to determine and visualize the 3-D distribution of local porosity. Figure 6.1 shows the flowchart of the computer code to find the 3-D distribution of the local porosity. The program calculates the porosity corresponding to the center of the box shaped subvolume. User can choose the dimensions of the blocks and the distance between block centers. If the blocks do not fit fully inside the 3-D image then the portions that are located outside the image boundaries are trimmed. The program can represent the results in form of filled contour plots or contour lines in three different planes (XY, XZ, and YZ) or local porosity distribution histogram or as an AVI movie. The 3-D distribution of the local porosity can also be saved in a 3-D array.

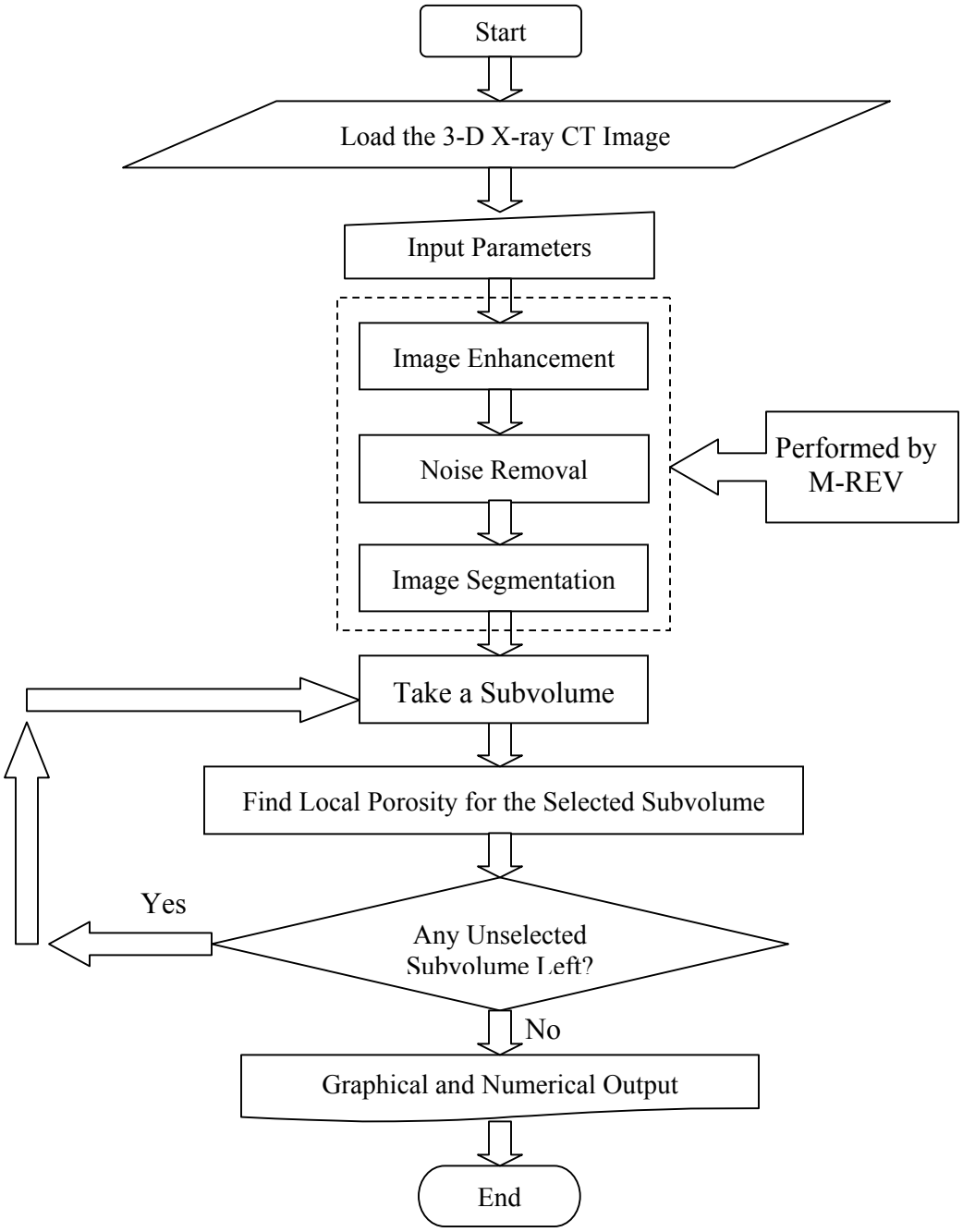

Figure 6.1. Flowchart of the 3-D local porosity distribution computer code

Figure 6.2 through 6.4 show the contours of 3-D local porosity distribution in XY, YZ, and XZ planes for a dry Silica specimen, respectively. The specimen was prepared in a plastic cylindrical mold, 27.82 *mm* in diameter, and 150.62 *mm* in height. The sand was compacted in five layers by tamping on the sides. Measured global porosity of the specimen (for the whole specimen volume) from the lab and REV code were 0.382 and 0.370, respectively. The contours show the local porosity distribution for one section at the middle of height (XY plane) and two sections and two other sections along the base diameter (YZ and XZ planes). The contours show that the distribution of the local porosity is not uniform. The porosity around the middle of the specimen is higher than the peripheral regions indicating that compaction does not achieve uniform condition across the specimen. The results also show a small segment near the surface where local porosity is decreased. Specimen indicating that this portion has been compacted more.

The histogram of the 3-D local porosity distribution is shown in Figure 6.5. The shape of the histogram for this compacted specimen is close to that of a normal distribution plot. Although the mean of the corresponding normal distribution is close to the global porosity of the specimen, they are not equal. If all of the subvolume blocks have the same size with no overlap between the blocks, then the average of the 3-D distribution of local porosity will be the same as the global porosity, otherwise a small difference is expected. The maximum values for local porosity distribution ($n=1$) correspond to the image background with no solid particles.

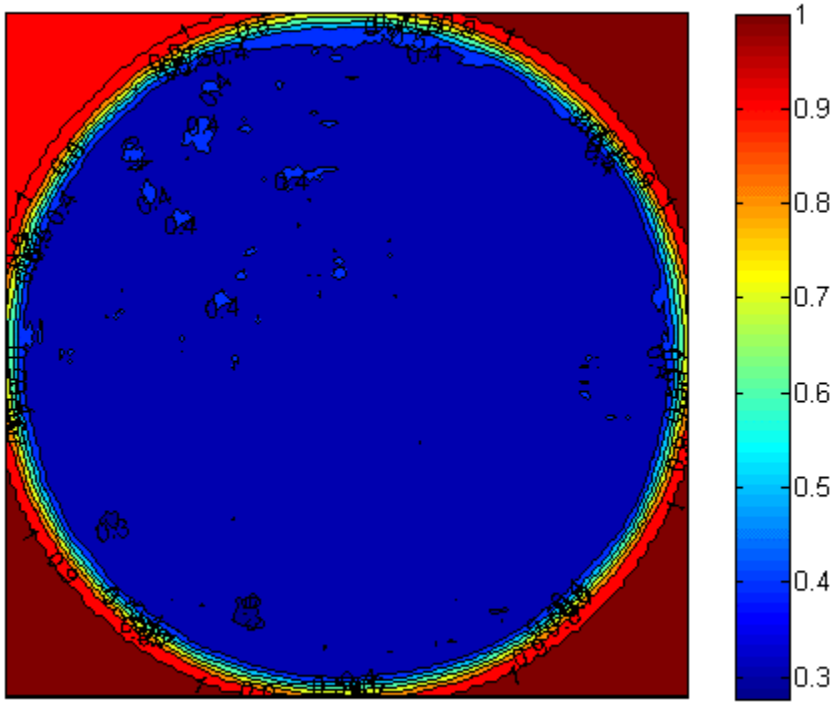

Figure 6.2. 3-D local porosity distribution contours of a Silica sand specimen in XY plane

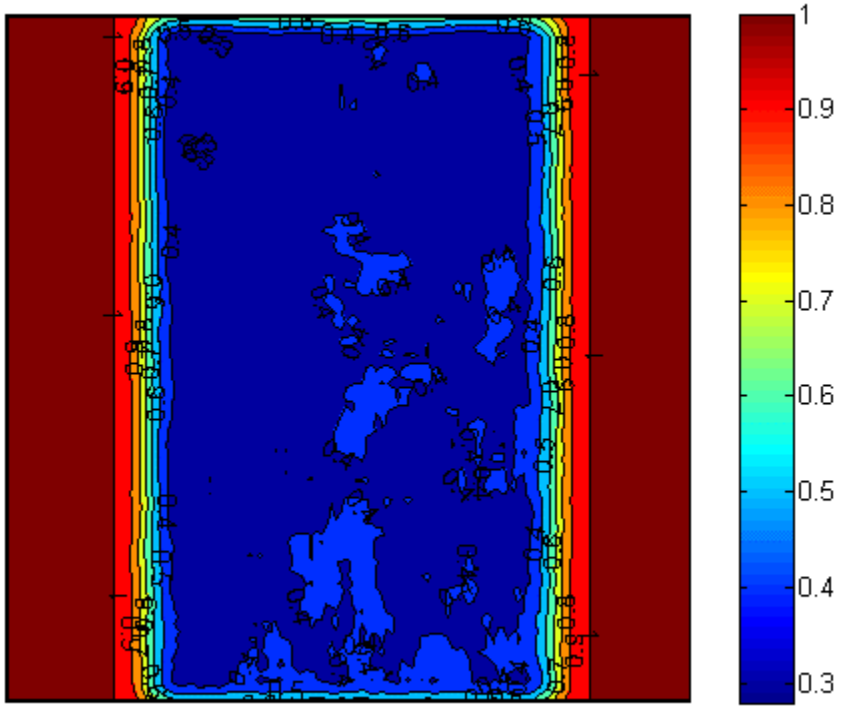

Figure 6.3. 3-D local porosity distribution contours of a Silica sand specimen in YZ plane

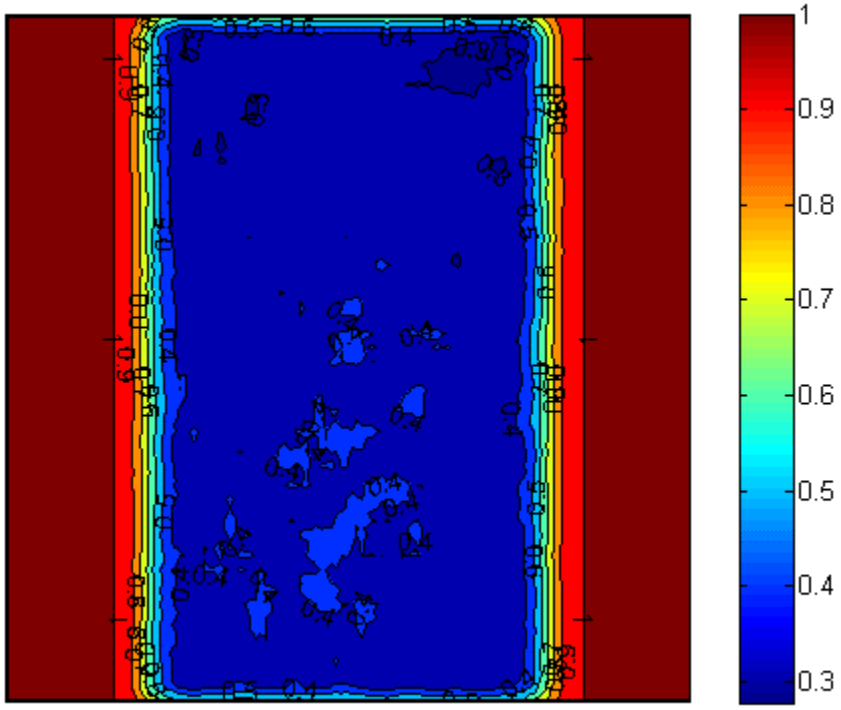

Figure 6.4. 3-D local porosity distribution contours of a Silica sand specimen in XZ plane

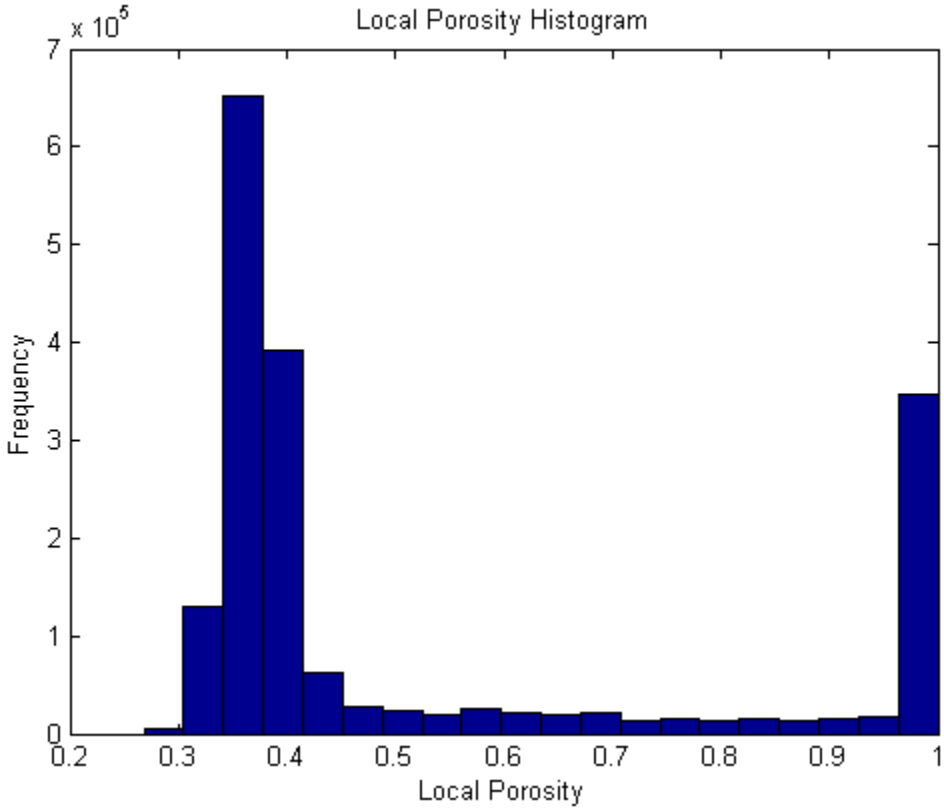

Figure 6.5. Histogram of 3-D local porosity distribution of a specimen of Silica sand

6.3 3-D Distribution of Local Porosity and Shear Bands Characterization

A combination of the developed techniques in chapter 5 and 3-D distribution of the local porosity can be used to characterize the soil microstructure in real time. Figure 6.6 shows a simple schematic diagram of the soil microstructure characterization in real time. A triaxial sand specimen is loaded by using the designed triaxial apparatus in chapter 4. A constant confining pressure is applied to the specimen for the whole period of the test. Axial load is applied in a very slow rate in several different steps. At each step loading is stopped and the specimen is scanned by X-ray CT. Scanning time is relatively fast so that no further changes in the soil microstructure is expected. Loading and scanning are continued until axial strain reaches to the final desired value (usually 20%). Then the 3-D CT images are processed to find the 3-D distribution of local porosity and displacement fields. Onset of formation of shear band and the related properties could be determined from sudden jumps in the 3-D distribution of the local porosity. Shape and orientation of the shear bands may be obtained directly from the 3-D X-ray CT images.

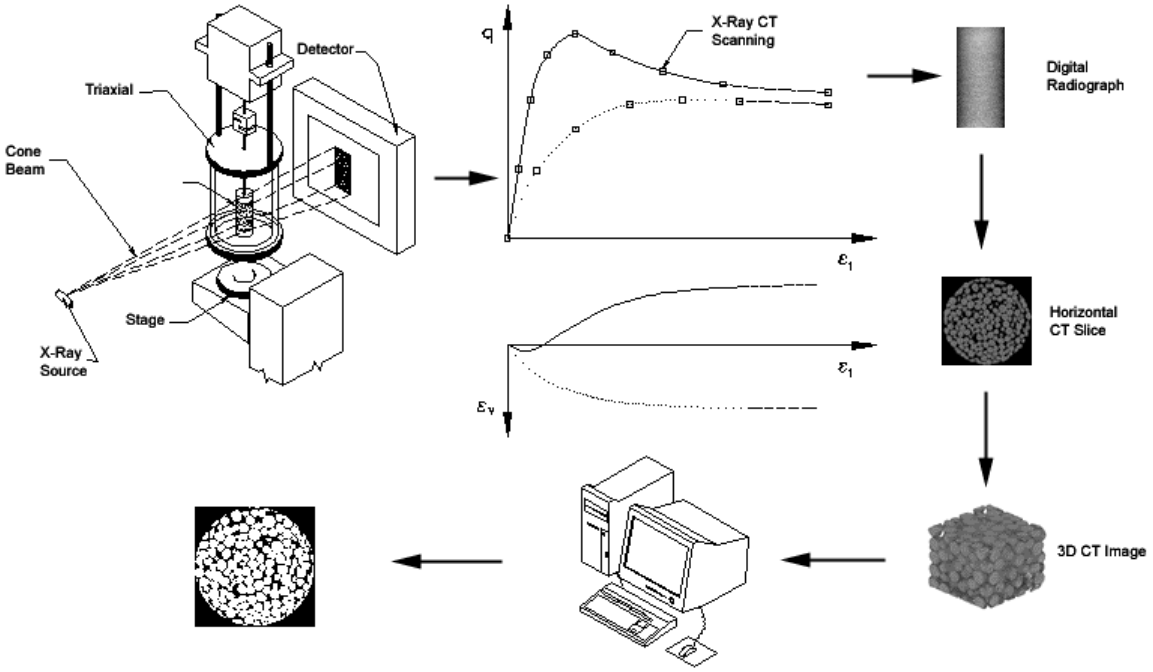

Figure 6.6. A summary of the shear band characterization procedure

Chapter 7

CONCLUSIONS AND RECOMMENDATIONS

7.1 Introduction

This study made use of the advances in X-ray computed tomography to generate 3-D images of the soil microstructure nondestructively. It has developed a systematic method to examine the existence and the characteristics of the representative elementary volume (REV) of a granular medium using X-ray CT. The study also developed a novel triaxial apparatus to be placed inside the X-ray chamber to facilitate the real time monitoring of the changes in sand microstructure when subjected to loading. Methods to find the internal 3-D displacement fields based on two 3-D X-ray CT images are also developed. The study concludes with the development of a method to quantify the 3-D local porosity distribution in specimens. This chapter presents a summary of the developments as well as some recommendations for future studies.

7.2 REV for Porosity of Sand

An interactive 3-D image-processing program was developed to process the 3-D CT images and choose the REV. The effect of the shape and size of the particles, specimen porosity, and location of the REV center were examined in this study using different specimens of spherical glass beads, silica sand and Ottawa sand. The results show the characteristic of three different regions; a microscopic fluctuations region, constant region, and monotonically increasing/decreasing region.

The REV radius for the glass beads specimens and random packing is found to be 2 to 3 times of the identical average sphere diameter. The radius for silica sand composed mainly of elongated particles is between 5 to 11 times of d_{50}, and for Ottawa sand composed mainly of subrounded particles is between 9 to 16 times of d_{50}. These values appear to justify the use of 10 to 20 diameters of sand grains adopted in some studies. The fact that the radius of REV appears to decrease with elongation and angularity leads us to the determination that interlocking may be a contributor in determining its size.

The proposed method is general and it can be applied for any granular or perforated material if the void sizes are more than the maximum CT image resolution. However, at the present time the maximum specimen size is limited to the capabilities of the X-ray CT equipment and available memory to process the image.

In view of its usefulness, the concept of REV relating to numerical modeling and selection of specimen size for laboratory tests is debated very much lately. As discussed in the introduction here, it is necessary to realize that REV concept is useful for getting average properties of a homogenous medium. On the other hand, element tests on natural media inevitably encounter heterogeneity and the classical continuum hypothesis breaks down. In this case, the size of REV becomes scale-dependent. One may define a REV size for a specific sized specimen in a laboratory-scale problem but this may not be applicable to larger sized specimens or field-scale problems, where heterogeneity at several scales exists. Additional non-local continuum measures are needed to fully describe scale effects in such heterogeneous media (See Al Hattamleh et al. 2003).

7.2 X-Ray Triaxial System

By applying some modifications and using a small light-weight loading system a novel triaxial system for real time monitoring of the soil microstructure was designed. This novel triaxial apparatus designed so that it can be placed on the FlashCT stage to generate the 3-D X-ray CT images of the soil microstructure in the time interval between the two load increments. This novel triaxial can also be used to perform triaxial tests on a wide range of different materials such as wood, asphalt, composites, ceramics, and plastics. Based on the design requirements in this study, acrylic material is recommended for the cell material.

7.3 3-D Internal Displacement Fields

The method of template matching to find the 2-D displacement fields between two 2-D digital photographs was extended to find the 3-D displacement fields between two 3-D X-ray CT images. An interactive computer program (M-DST) was developed to load two 3-D CT images, find the displacement fields, and represent it as a vector field or contour plots in three different planes.

The major problems with extension of this method for 3-D X-ray CT images are fluctuations of the X-ray beam, limited computer memory to load two 3-D X-ray CT images at the same time, and extremely long processing time. Fluctuation of the X-ray intensity was fixed using large numbers of averaging captured frames to form each digital radiograph. To overcome to the memory problem with loading of two 3-D X-ray CT images at the same time, the method of successive read and write on the hard disk drive was applied. Instead of searching the whole voxels of the current image, a search region is defined in the computer code and in this way only the part of the image, which is

required for processing, is loaded in memory to avoid memory overflow. To speed up the processing time, the computer code was developed so that user can install it on as many as machines he wants to find the displacement fields for each part individually. The results for each part are put together to have the displacement fields for the whole image.

7.4 3-D Local Porosity Distribution

3-D image processing techniques were used to find local porosity distribution. A computer code was developed to find the local porosity distribution for 3-D X-ray CT images. The 3-D X-ray CT image after segmentation is subdivided to smaller subvolumes and porosity is determined for each subvolume. The program can represent the results in form of filled contour plots or contour lines in three different planes (XY, XZ, and YZ) or local porosity distribution histogram or as an AVI movie. The 3-D distribution of the local porosity can also be saved in a 3-D array.

The results of 3-D local porosity distribution for Silica sand specimens prepared in a plastic mold by compacting the sand in five layers and tamping on the sides showed that porosity around the middle of the specimen is higher than the peripheral regions indicating that compaction does not achieve uniform condition across the specimen. The results also show a small segment near the surface where local porosity is decreased. Specimen indicating that this portion has been compacted more.

The developed code can also be applied to characterize the shear band properties for specimens are loaded inside the X-ray CT chamber. Onset of formation of shear band and the related properties could be determined from sudden jumps in the 3-D distribution of the local porosity.

7.5 Recommendations

This work has laid the foundation for development of nondestructive methods to characterize the granular microstructure and its changes in real time combining X-ray CT technology with robust image processing algorithms. This work should stimulate the experimental studies that attempt to quantify strain localization and related phenomena nondestructively.

The following recommendations are made for further research:

- Currently power of the X-ray CT and computer memory are two major issues that limit the finding REV to small scales. However, with continued advances in X-ray CT systems and computer hardware would push these limits and it would be possible to find REV for larger scales.
- In case of large rotations a large amount of error is expected in determination of 3-D displacement fields. An optimization code may need to be added to M-DST to consider rotation of the blocks.
- When the reference and the current image do not have the same size or there is distortion in the target, then the cross-correlation method used here fails. In this case a mathematical model such as hidden Markov models, which is widely used for voice recognition and computer vision, is recommended to find 3-D displacement fields.
- The time and delay in the triaxial device did not enable the real time experiments. Experiments should be performed to characterize the features of strain localization in granular materials.

- The current design of the triaxial apparatus is limited to sands. For the triaxial testing of stronger materials such as concrete and rock would need a different design as stronger and bigger jacks are required for imposing larger axial loads. In this case the rotary stage will not be able to handle the heavy weight of both triaxial apparatus and jack together and the alternate design in Appendix C is recommended.

REFERENCES

Aifantis, E. C. (1987). "Physics of Plastic Deformation". *International Journal of Plasticity*, Vol. 3, No. 3, pp. 2ll-247.

Al Hattamleh, O. (2003). *Investigation Of The Deformation Of Granular Materials: A Micromechanics Approach*. Ph. D. Thesis. Washington State University.

Al Hattamleh, O., Muhunthan, B., and Zbib, H. M. (2004). "Gradient Plasticity Modeling of Strain Localization in Granular Materials". *International Journal for Numerical and Analytical Methods in Geomechanics*, No. 28, pp. 465-481.

Al Hattamleh, O. (2003-2005). *Personnel Communication*. Washington State University.

Al Ramahi, B. (2004). *Characterization of Shearing Phenomenon and Porosity of Porous Media using X-Ray Computed Tomography*. MSc. Thesis. Louisiana State University.

Al Raoush, R. I. and Willson, C. S. (2005). "A Pore-Scale Investigation of a Multiphase Porous Media System". *Journal of Contaminant Hydrology*, Vol. 77, No. 1-2, pp. 67-89.

Al Raoush, R. I. and Alshibli, K. A. (2006). "Distribution of Local Void Ratio in Porous Media Systems from 3-D X-Ray Microtomography Images". *Physica A: Statistical Mechanics and its Applications*, Vol. 359, No. 1-4, pp. 713-728.

Alshibli, K. A. and Sture, S. (1999). "Sand Shear Band Thickness Measurements by Digital Imaging Techniques". *Journal of Computing in Civil Engineering*, Vol. 13, No. 2, pp. 103-109.

Alshibli, K. A., Sture, S., Costes, N. C., Frank, M. L., Lankton, M. R., Batiste, S. N., and Swanson, R. A. (2000). "Assesment of Localized Deformations In Sand Using X-Ray Computed Tomography". *ASTM Geotechnical Testing Journal*, Volume 23, No. 3, pp. 274-299.

Alshibli, K. A., Batiste, S. N., Swanson, R. A., Sture, S., Costes, N. C., and Lankton, M. R. (2000). "Quantifying void ratio variation in sand using computed tomography Source". *Geotechnical Special Publication*, No. 106, pp. 30-43.

Alshibli, K. A. and Sture, S. (2000). "Shear Band Formation in Plane Strain Experiments of Sand". *Journal of Geotechnical and Geoenvironmental Engineering*, Vol. 126, No. 6, pp. 495-503.

Alshibli, K. A., Batiste, S. N., and Sture, S. (2003). "Strain Localization in Sand: Plane Strain versus Triaxial Compression". *Journal of Geotechnical and Geoenvironmental Engineering*, Vol. 129, No. 6, pp. 483-494.

Alshibli, K. A. and Al Ramahi, B. (2006). "Microscopic Evaluation of Strain Distribution in Granular Materials During Shear". *Journal of Geotechnical and Geoenvironmental Engineering*, Vol. 132, No. 1, pp. 80-91.

ASTM Standard E 1441–00, *Standard Guide for Computed Tomography CT Imaging,* Annual Book of ASTM Standards, Nondestructive Testing, Vol. 03.03, ASTM International, West Conshohocken, PA, 2005.

Auzerais, F. M., Dunsmuir, J., Ferreol, B. B., Martys, N., Olson, J., Ramakrishnan, T. S., Rothman, D. H., and Schwartz, L. M. (1996). "Transport in Sandstone: A Study Based on Three Dimensional Microtomography". *Geophysical Research Letters*, Vol. 23, No. 7, pp. 705-708.

Batiste, S. N., Alshibli, K. A.; Sture, S., and Lankton, M. (2004). "Shear Band Characterization of Triaxial Sand Specimens using Computed Tomography". *Geotechnical Testing Journal*, Vol. 27, No. 6, pp. 568-579.

Bazant, Z. P. and Gambarova, P. G. (1984). "Crack Shear in Concrete: Crack Band Microplane Model". *Journal of Structural Engineering*, Vol. 110, No. 9, pp. 2015-2035.

Bear, J. (1972). *Dynamics of Fluids in Porous Media*, American Elsevier Publisher Co., New York.

Budhu, M. (1984). "On Comparing Simple Shear and Triaxial Test Results". *Journal of Geotechnical Engineering*, Vol. 110, No. 12, pp. 1809-1814.

Chang, C. S., Matsushima, T., and Lee, X. (2003). "Heterogeneous Strain and Bonded Granular Structure Change in Triaxial Specimen Studied by Computer Tomography". *Journal of Engineering Mechanics, ASCE*, Vol. 129, No. 11, pp. 1295-1307.

Charbeneau, R. J. (2000). *Groundwater Hydraulics and Pollutant Transport*. Prentice Hall, New Jersey.

Cislerova, M. and Votrubova, J. (2002). "CT Derived Porosity Distribution and Flow Domains". *Journal of Hydrology*, Vol. 267, No. 3-4, pp. 186-200.

Clausnitzer, V. and Hopmans, J. W. (1999). "Determination of Phase-Volume Fractions from Tomographic Measurements in Two-Phase Systems". *Advances in Water Resources*, Vol. 22, No. 6, pp. 577-584.

Clocksin, W. F., Quinta Da Fonseca, J., Withers, P. J., and Torr, P. H. S. (2002). "Image Processing Issues in Digital Strain Mapping". *Proceedings of SPIE-The International Society for Optical Engineering*, Vol. 4790, pp. 384-395.

Culligan, K. A., Wildenschild, D., Christensen, B. S. B., Gray, W. G., Rivers, M. L., and Tompson, A. F. B. (2004). "Interfacial Area Measurements for Unsaturated Flow through a Porous Medium". *Water Resources Research*, Vol. 40, No. 12, pp. 1-12.

Dagher, H. J., Abdel-Magid, B., Ritter, M., and Iyer, S. (1997). "GRP Prestressing of Wood Decks". *Proceeding of Structure Congress XV, ASCE*, Portland, Oregon, pp. 585-589.

de Borst, R. and Muehlhaus, H. B. (1992). "Gradient-Dependent Plasticity: Formulation and Algorithmic Aspects". *International Journal for Numerical Methods in Engineering*, Vol. 35, No. 3, pp. 521-539.

Dennis, M. J. (1989). "Industrial Computed Tomography". *Reprinted from Metals Handbook*, Vol. 17, pp. 358–386.

Desrues, J. and Chambon, R. (1989). "Shear band analysis for granular materials: the question of incremental non-linearity". *Ingenieur-Archive*, Vol. 59, No. 3, pp. 187-196.

Desrues, J., Chambon, R.; Mokni, M., and Mazerolle, F. (1996). "Void ratio Evolution inside Shear Bands in Triaxial Sand Specimens Studied by Computed Tomography". *Geotechnique*, Vol. 46, No. 3, pp. 529-546.

Desrues, J. and Viggiani, G. (2004). "Strain Localization in Sand: An Overview of the Experimental Results Obtained in Grenoble using Stereophotogrammetry". *International Journal for Numerical and Analytical Methods in Geomechanics*, Vol. 28, No. 4, pp. 279-321.

Desrues, J. and Hammad, W. (1989). "Shear Banding Dependency on Mean Pressure Level in Sand". International workshop on Numerical Methods for Localization and Bifurcation of Granular Bodies, Gdansk, Poland.

Dullien, F. A. L. (1979). *Porous Media: Fluid Transport and Pore Structure*, Academic Press, NewYork.

Eaton, D. (2006). "Fast NCC". http://www.cs.ubc.ca/~deaton/remarks_ncc.html.

Finno, R. J., Harris, W. W., Mooney, M. A., and Viggiani, G. (1996). "Strain Localization and Undrained Steady State". *Journal of Geotechnical Engineering, ASCE*, Vol.122, No. 6, pp. 462-473.

Finno, R. J., Harris, W. W., Mooney, M. A., and Viggiani, G. (1997). "Shear Bands in Plane Strain Compression of Loose Sand". *Geotechnique*, Vol. 47, No. 1, pp. 149-165.

Fleck, N. A. and Hutchinson, J. W. (1993). "Phenomenological Theory for Strain Gradient Effects in Plasticity". *Journal of the Mechanics and Physics of Solids*, Vol. 41, No. 12, pp. 1825-1857.

Ge, X., Ren, J., Pu, Y., Ma, W., and Zhu, Y. (1999). "Real-in-Time CT Triaxial Testing Study of Meso-Damage Evolution Law of Coal". *Yanshilixue Yu Gongcheng Xuebao/Chinese Journal of Rock Mechanics and Engineering*, Vol. 18, No. 5, pp. 497-502.

Geraud, Y. (1991). *Deformations Thermomecaniques et Porosite des Roches Granitiques. Evolution des Espaces Poreux*, Thesis doct., University of Maseilles.

Geraud, Y., Mazerolle, F. Raynaud, S., and Lebon, P. (1998). "Crack Location in Granite Samples Submitted to Heating, Low Confining Pressure and Axial Loading*"*. *International Journal of Geophysics*, No. 133, pp. 553-567.

Gonzalez, R. C., Woods, R. E., and Eddins, S. L. (2004). *Digital Image Processing using Matlab*, Prentice Hall.

Graton, L. C. and Fraser, H. J. (1935). "Systematic Packing of Spheres with Particular Relation to Porosity and Permeability," *Journal of Geology*, Vol. 43, No. 8, pp. 785–909.

Gudehus, G. and Nubel, K. (2004). "Evolution of Shear Bands in Sand". *Geotechnique*, Vol. 54, No. 3, pp. 187-201.

Guler, M., Edil, T. B., and Bosscher, P. J. (1999). "Measurement of Particle Movement in Granular Soils using Image Analysis". *Journal of Computing in Civil Engineering*, Vol. 13, No. 2, pp. 116-122.

Han, C. and Drescher, A. (1993). "Shear Bands in Biaxial Tests on Dry Coarse Sand". *Soils and Foundations*, Vol. 33, No. 1, pp. 118-132.

Haralick, R. M. and Shapiro, L. G. (1993). Computer and Robot Vision, Vol. II, Addison-Wesley Publishing Company, Inc.

Horii, H., Takamatsu, K., Inoue, J., and Sasaki, N. (1998). "Measurement of Displacement Field by Match Method and Observation of Strain Localization in Soft Rock". *Proceeding of Second International Conference on Imaging Technologies: Techniques and Applications in Civil Engineering, ASCE*, Reston, VA, pp. 10-19.

HYTEC INC, 2004, *FlashCT User's Manuals*, Los Alamos, NM.

Kak, A. C. and Slaney, M. (2001). *Principle of Computerized Tomographic Imaging*, Siam, Philadelphia, PA.

Klobes, P., Riesemeier, H., Meyer, K., Goebbels, J., Siitari-Kauppi, M., and Hellmuth, K. H. (1997). "Investigation of Rock Samples using X-Ray Microcomputer-Tomography before and after Mercury Intrusion Porosimetry". *Materials Research Society Symposium - Proceedings*, Vol. 465, *Scientific Basis for Nuclear Waste Management XX*, pp. 863-870.

Lawler, J., and Shah, S. (2002). "Fracture Process in Concrete Studied with Subregion Scanning Computer Vision". *The 15th Engineering Mechanics Division Conf., ASCE*, Reston, VA.

Lewis, J. P. (1995). "Fast Normalized Cross-Correlation". Industrial Light & Magic, http://www.idiom.com/~zilla/Papers/nvisionInterface/nip.html.

Li, X. J. and Zhang, D. L. (2000). "Monitoring Change of Structure of Road Foundation Soil in Uniaxial Compression Test with CT". *Chinese Journal of Geotechnical Engineering*, Vol. 22, No. 2, pp. 206-209.

Liu, J. and Iskander, M. (2004). "Adaptive cross correlation for imaging displacements in soils". *Journal of Computing in Civil Engineering*, Vol. 18, No. 1, pp. 46-57.

Lu, Z. H., Chen, Z. H., and Pu, Y. B. (2002). "Study on Damage Evolution of Natural Expansive Soil with Computerized Tomography during Triaxial Shear Test". Chinese Journal of Hydraulics Engineering, No. 6, pp. 106-112.

Masad, E. and Muhunthan, B. (2000). "Three-Dimensional Characterization and Simulation of Anisotropic Soil Fabric". *Journal of Geotechnical and Geoenvironmental Engineering*, Vol. 126, No. 3, pp. 199-207.

Masad, E., Button, J. W., and Papagiannakis, T. (2000). "Fine-aggregate angularity: Automated image analysis approach". *Transportation Research Record*, No. 1721, pp. 66-72.

MathWorks, 2004, *Image Processing Toolbox for Use with MATLAB User's Guide*, Version 5, Natick, MA.

Meegoda, N. J., King, I. P., and Arulanandan, K. (1989). "Expression for the Premeability of Anisotropic Granular Media". *International Journal for Numerical and Analytical Methods in Geomechanics*, Vol. 13, No. 6, pp. 575-598.

Mindlin, R. D. (1964). "Microstructure in Linear Elasticity". *Archive for Rational Mechanics and Analysis*, Vol. 10, Issue 1, pp.51-78.

Muhunthan, B. Chameau, J. L. and Masad, E. (1996). "Fabric Effects on the Yield Behavior of Soils". *Soils and Foundations, JSGE*, Vol. 36, No. 3, pp. 85-97.

Nemat-Nasser, S. and Okada, N. (2001). "Radiographic and Microscopic Observation of Shear Bands in Granular Materials". *Geotechnique*, Vol. 51, No. 9, pp. 753-765.

Oda, M., Konishi, J., and Nemat-Nasser, S. (1982). "Experimental Micromechanical Evaluation of Strength of Granular Materials: Effect of Particle Rolling". *Mechanics of Materials*, Vol. 1, No. 4, pp. 269-283.

Oda, M. and Kazama, H. (1998). "Microstructure of Shear Bands and Its Relation to the Mechanisms of Dilatancy and Failure of Dense Granular Soils". *Geotechnique*, Vol. 48, No. 4, pp. 465-481.

Oda, M., Takemura, T., and Takahashi, M. (2004). "Microstructure in Shear Band Observed by Microfocus X-ray Computed Tomography". *Geotechnique*, Vol. 54, No. 8, pp. 539-542.

Ostoja-Starzewski, M. (2005). "Scale Effects in Plasticity of Random Media: Status and Challenges". *International Journal of Plasticity*, Vol. 21, No. 6, pp. 1119-1160.

Otani, J., Mukunoki, T., and Obara, Y. (2000). "Application of X-ray CT Method for Characterization of Failure in Soils". Soils and Foundations, Vol. 40, No. 2, pp. 111-118.

Otani, J. and Mukunoki, T. (2001). "Development of New Triaxial Compression Test Apparatus for Geomaterials on Industrial X-Ray CT Scanner". *Proceeding of XVth International Conference on Soil Mechanics and Geotechnical Engineering.* pp. 231-234.

Otani, J. and Mukunoki, T. (2001). "Development of New Triaxial Compression Test Apparatus for Geomaterials on Industrial X-Ray CT Scanner". *Proceeding of XVth International Conference on Soil Mechanics and Geotechnical Engineering*, pp. 231-234.

Otsu, N. (1979). "Threshold Selection Method from Gray-Level Histograms". *IEEE Transactions on Systems, Man and Cybernetics*, Vol. SMC-9, No. 1, pp. 62-66.

Pradhan, T. (1997). "Characteristics of Shear Band in Plane Strain Compression Test of Sands". *In Deformation and Progressive Failure in Geomechanics, Asaoka A, Adachi T, Oka F. (eds). Pergamon, Oxford*, pp. 241-246.

Rechenmacher, A., and Saab, N. (2002). "Digital Image Correlation (DIC) to Evaluate Progression and Uniformity of Shear Bands in Dilative Sands". *Proceedings of the15th Engineering Mechanics Division Conference, ASCE*, Reston, Va.

Roberts, A. J., (1994). *A One-Dimensional Introduction to Continuum Mechanics*, World Scientific Publishing Co., Singapore.

Russ, J. C., (2002). *The Image Processing Hand Book*, CRC Press, Boca Raton, FL.

Saada, A. S., Bianchini, G. F., and Liang, L. (1994). "Cracks, Bifurcation and Shear Bands Propagation in Saturated Clays". *Geotechnique*, Vol. 44, No. 1, pp. 35-64.

Saada, A. S., Liang, L., Figueroa, J. L., and Cope, C. T. (1999). "Bifurcation and Shear Band Propagation in Sands". *Geotechnique*, Vol. 49, No. 3, pp. 367-385.

Sadek, S., Iskander, M., and Liu, J. (2002). "Geotechnical Properties of Transparent Silica". *Canadian Geotechnical Journal*, Vol. 39, No. 1, pp. 111-124.

Sadek, S., Iskander, M., and Liu, J. (2003). "Accuracy of Digital Image Correlation for Measuring Deformations in Transparent Media". *Journal of Computing in Civil Engineering*, Vol. 17, No. 2, pp. 88-96.

Schanz, T., Desrues, J., and Vermeer, P. A. (1997). "Comparison of Sand Data on Different Plane Strain Devices". *In Deformation and Progressive Failure in Geomechanics, Asaoka A, Adachi T, Oka F. Pergamon*, *Oxford*, pp. 289-295.

Shah, S. P. and Choi, S. (1996). "Evaluation of Fracture Processes in Cement-Based Materials under Compression Using Computer Vision". *American Society of Mechanical Engineers, Materials Division (Publication) MD*, Vol. 74, pp. 25-26.

Shi, B., Murakami, Y., Wu, Z., Chen, J., and Inyang, H. (1999). "Monitoring of Internal Failure Evolution in Soils using Computerization X-ray Tomography". *Engineering Geology 54*, pp. 321-328.

Spanne, P., Jones, K. W., Prunty, L., and Anderson, S. H. (1994). "Potential Applications of Synchrotron Computed Microtomography to Soil Science". *SSSA Special Publication*, No. 36, pp. 43-57.

Spanne, P., Thovert, J. F., Jacquin, C. J., Lindquist, W. B., Jones, K. W., and Adler, P. M. (1994). "Synchrotron Computed Microtomography of Porous Media: Topology and Transports". *Physical Review Letters*, Vol. 73, No. 14, pp. 2001-2004.

Stroeven, M., Askes, H., and Sluys, L. J. (2004). "Numerical Determination of Representative Volumes for Granular Materials". *Computer Methods in Applied Mechanics and Engineering*, Vol. 193, No. 30-32, pp. 3221-3238.

Sun, H., Chen, J. F., and Ge, X. R. (2004). "Deformation Characteristics of Silty Clay Subjected to Triaxial Loading, by Computerised Tomography". *Geotechnique*, Vol. 54, No. 5, pp. 307-314.

Tani, K. (1997). "X-Ray Computed Tomography Technique to Observe Shear Banding in Dense Sands. Deformation and Failure in Geomechanics". *IS Nagoya '97, Pergamon,* pp. 315-320.

Vardoulakis, I. (1980). "Shear Band Inclination and Shear Modulus of Sand in Biaxial Tests". *International Journal for Numerical and Analytical Methods in Geomechanics*, Vol. 4, No. 2, pp. 103-119.

Vardoulakis, I. and Aifantis, E. C. (1989). Gradient Dependent Dilatancy and Its Implications in Shear Banding and Liquefaction". *Ingenieur-Archiv*, Vol. 59, No. 3, pp. 197-208

Vardoulakis, I. (1996). "Deformation of Water-Saturated Sand: I. Uniform Undrained Deformation and Shear Banding". *Geotechnique*, Vol 46, No. 3, pp. 441-456.

Viggiani, G., Lenoir, N., Besuelle, P., Michiel, M. D., Marello, S., Desrues, J., and Kretzschmer, M. (2004). "X-ray Microtomography for Studying Localized Deformation in Fine-Grained Geomaterials under Triaxial Compression". *C. R. Mecanique 332, Elsevier*, pp. 819-826.

Vinegar, H. J., De Waal, J. A., and Wellington, S. L. (1991). "CT Studies of Brittle Failure in Castlegate Sandstone". *International Journal of Rock Mechanics and Mining Sciences & Geomechanics Abstracts*, Vol. 28, No. 5, pp. 441-450.

Walton, K. (1987). "Effective Elastic Moduli of a Random Packing of Spheres". *Journal of the Mechanics and Physics of Solids*, Vol. 35, No. 2, pp. 213-226.

Wang, Q. and Lade, P. V. (2001). "Shear Banding in True Triaxial Test and Its Effect on Failure in Sand". *Journal of Engineering Mechanics*, Vol. 127, No. 8, pp. 754-761.

Wang, L. B., Frost, J. D., and Lai, J. S. (2004). "Three-Dimensional Digital Representation of Granular Material Microstructure from X-ray Tomography Imaging". Journal of Computing in Civil Engineering, ASCE, Vol. 18, No.1, pp. 28-35.

White, D., Take, W., and Bolton, M. (2001). "Measuring Soil Deformation in Geotechnical Models Using Digital Images and PIV Analysis". *Proceedings of the 10th International Conference on Computer Methods and Advances in Geomechanics*, Tuscon, AZ, Balkema, Rotterdam, The Netherlands, pp. 997-1002.

White, D. J. and Bolton, M. D. (2004). "Displacement and Strain Paths During Plane-Strain Model Pile Installation in Sand". *Geotechnique*, Vol. 54, No. 6, pp. 375-397.

Wood, D. M. (2002). "Some Observations of Volumetric Instabilities in Soils". *International Journal of Solids and Structures* 39, Pergamon, pp. 3429-3449.

Yagi, K., Miura, S., Asonuma, T., Sakon, T., and Nakata, T. (1997). "Particle Crushing and Shear Banding of Volcanic Coarse-Grained Soils". *In Deformation and Progressive Failure in Geomechanics, Asaoka A., Adachi T., Oka F. (eds). Pergamon; Oxford*, pp. 139-145.

Yoshida, T., Tatsuoka, F., and Siddiquee, M. (1994). "Shear Banding in sands Observed in Plane Strain Compression". *Localization and Bifurcation theory for Soils and Rocks, Chambon R., Desrues J., Vardoulakis I. (eds). Balkema, Rotterdam*, pp. 165-181.

Zbib, H. M. and Aifantis, E. C. (1988). "On the Concept of Relative and Plastic Spins and Its Implications to Large Deformation Theories. Part II: Anisotropic Hardening Plasticity". *Acta Mechanica*, Vol. 75, pp. 35-56.

Zhou, Z., Synolakis, C. E., Leahy, R. M., and Song, S. M. (1995). "Calculation of 3-D Internal Displacement Fields from 3-D X-ray Computer Tomographic Images". *Proceedings: Mathematical and Physical Sciences*, Vol. 449, No. 1937, pp. 537-554.

Appendix A

X-RAY COMPUTED TOMOGRAPHY

A.1 Introduction

X-ray Computed tomography (X-ray CT), in a general sense, is an imaging technique that generates an image of density distribution of a thin cross-section of a specimen. Computed tomography imaging is also known as CAT scanning (Computed Assisted Tomography). Tomography is from the Greek word "tomos" meaning "slice" or "section" and “graphia” meaning, "describing". Computed tomography was invented by the British Engineer Godfrey Hounsfield of EMI Laboratories in the late 1960’s and early 1970’s in England, and independently by South African born physicist Allan M. Cormack (1963) of Tufts University, Massachusetts. Since then X-ray CT has made great improvements in speed, quality, and resolution.

The X-ray CT image represents the point-by-point linear attenuation coefficients in the slice, which depends on the physical density of the material, the effective atomic number of the material, and the X-ray beam energy. X-ray CT image is highly sensitive to small differences (less than 1%) in density (Dennis 1989). Computed tomography system can also produce digital radiography images (DR). Both DR and CT images may be further processed. A digital radiography image is a digital attenuation image, which formed by placing the specimen between the X-ray source and the detector. Consequently, in DR all points are projected on a 2-D plane and finding the 3-D coordinates of a point form a DR is almost impossible. On the other hand, in CT images

the coordinates of every point are known and this is the major difference between a DR image and a CT image (Figures A.1 and A.2). A series of CT images can be used to characterize the object volume. The 3-D image is formed by voxels, which are box-shaped volume defined by the area of the pixel and the height of the slice thickness (Appendix B).

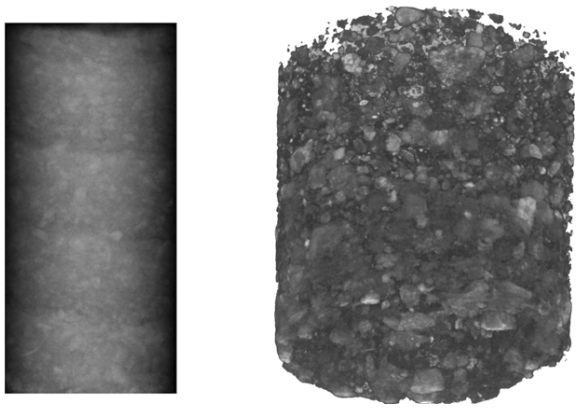

(a) (b)

Figure A.1. Difference between (a) digital radiograph and (b) 3-D X-ray CT image of a cylindical soil sample

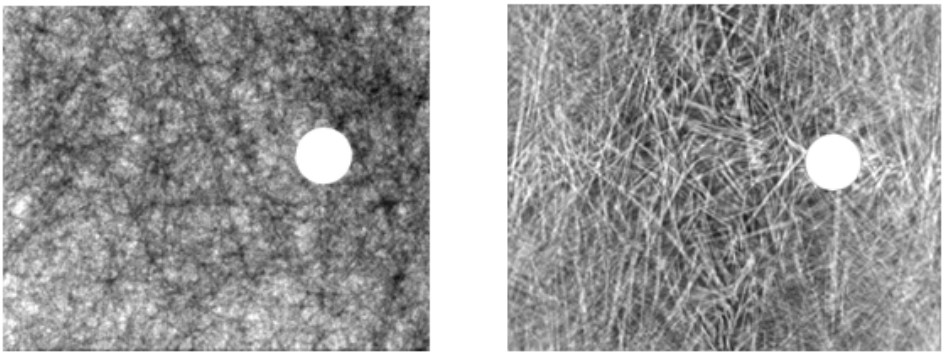

(a) (b)

Figure A.2. Difference between (a) digital radiograph and (b) X-ray CT image of a reinforced composite specimen (middle slice)

A.2 Principles of X-ray CT

The CT scanning system contains a radiation source and a linear array radiation detector with a precision stage to scan cross-sectional slice from different angles. The detector usually consists of a series of individual X-ray sensors arranged in lines and columns. X-ray beam may be in any of these forms; parallel beam, fan beam, and cone beam depending on the geometric shape. However, the beam must be wide enough to expose all the detector elements. The pixels on the detector measure the energy of the X-ray beam, which can be related to the numbers of photons. Subsequently, the acquired data are sent to the computer to produce the CT image. The CT image reconstruction algorithm generates two-dimensional images in horizontal planes from a set of digital radiographs taken at different angels. Though the whole processes of data acquisition, reconstruction, and post processing are done by the X-ray CT Software, knowing the basic principles of computed tomography and the meaning of important terms in X-ray

CT are necessary. Therefore, a brief description of the important terminology is provided next for completeness.

A.2.1 CT Numbers (H)

The resulting images of CT are grey scale images; usually white color indicates the highest density and black the lowest density (Figures A.3 and A.4). Each shade is related to a CT number or Hounsfield unit (Hounsfield 1973):

$$CT\ Number(H) = 1000\left(\frac{\mu^x - \mu_w{}^x}{\mu^x{}_w}\right) \tag{A.1}$$

where

μ^x = linear attenuation coefficient

$\mu_w{}^x$ = linear attenuation coefficient of the water

The scaling of the linear attenuation coefficient into an integer pixel value, as well as the range of CT number scales, is somewhat arbitrary among the different systems. For example, in medical CT systems the CT number of water is assumed zero and is considered as a reference for other CT numbers. On the other hand, in industrial CT systems the CT number of air is normally set the value 0. Note that no standard scaling of the CT values is applicable to all different materials and X-ray energies used. The value $H = 0$ corresponds to water and the value $H = -1000$ corresponds to $\mu^x = 0$, which is assumed to be the attenuation coefficient of air.

The projection data values for a narrow mono-energetic beam of X-ray radiation can be theoretically modeled by considering first Lambert's law of absorption:

$$I = I_0 \exp(-\mu^x s) \tag{A.2}$$

where I is the intensity of the beam transmitted through the absorber, I_0 is the initial intensity of the beam, s is the thickness of the absorber, and μ^x is the linear attenuation coefficient of the absorber material.

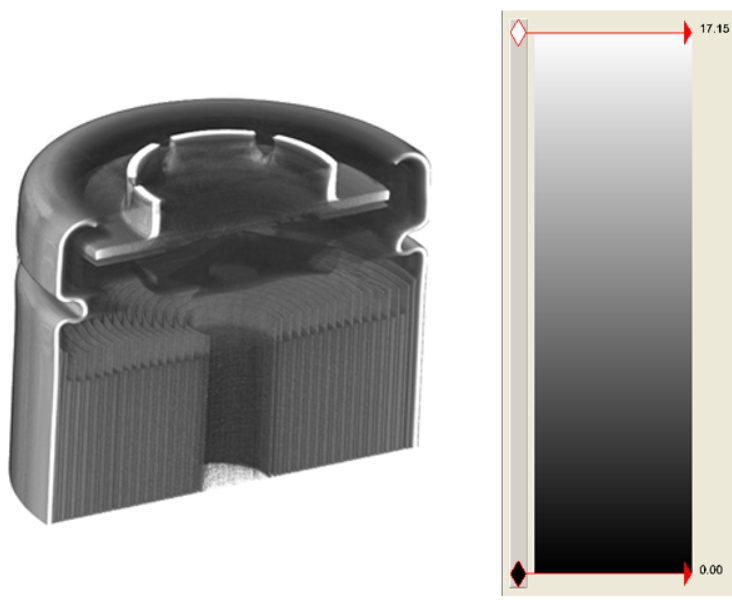

Figure A.3. 3-D X-ray CT image of a battery and distribution of CT numbers

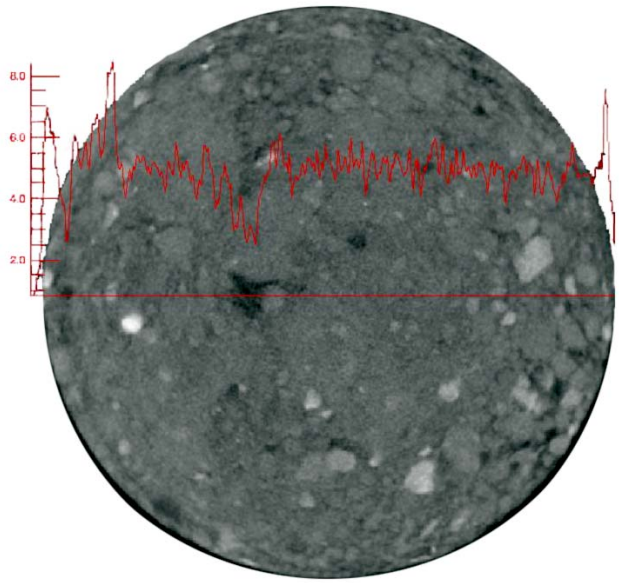

Figure A.4: Variation of CT numbers along the diameter of a soil sample

A.2.2 CT Image Quality

Spatial resolution, image contrast, and image artifacts are three basic factors affecting image quality. Spatial resolution is a measure of the ability of an imaging system to identify and distinguish small details. For example, the X-ray CT system at Washington State University can reach a spatial resolution up to 5 micron under certain conditions (high enough to detect sand particles). The amount of the contrast on a X-ray CT image is governed by object contrast, which refers to the contrast generated by variations in the attenuations of the radiation propagating through the specimen, the contrast resolution of the detector-readout system, and the size of discontinuity with respect to the special resolution of the system.

Artifacts are image features that do not correspond to physical structures in the object. All imaging techniques are subject to certain types of artifacts. In general the two

major causes of X-ray CT image artifacts are the finite amount of data for generating the constructed image, and the systemic errors in CT process and hardware. Inaccuracies in geometry, beam hardening (the increase in effective energy of a poly-energetic X-ray beam with increasing the attenuation of the beam), aliasing (an artifact in discretely measured data cause by insufficient sampling of high-frequency data, with this high frequency information falsely recorded at a lower frequency), and partial penetration are some of the other factors known to cause artifact. For instance the straight lines and noisy circles in Figure A.5 are artifacts on a CT slice of a battery.

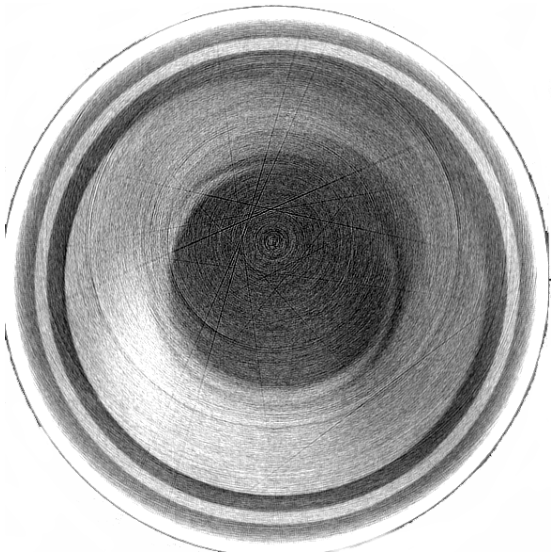

Figure A.5. Artifacts (straight lines and noisy circles) on a X-ray CT slice of a battery

A.2.3 Computed Tomography Reconstruction Techniques

To reconstruct a CT image, first the measured radiation intensities are converted into the projection data that correspond to the sum or projection of X-ray densities along a ray path. Subsequently, the point-by-point distribution of the X-ray densities in the two-dimensional image of the cross-sectional slice is determined by processing of the

projection data with a reconstruction algorithm. These are the basic steps of reconstruction process. There are many different reconstruction algorithms available for computed tomography. Most, however, are based on two basic methods: transform methods and iterative methods. The two main types of transform methods are Fast Fourier Transform (FFT) and Filtered Back-Projection. In industrial X-ray CT systems to process large image sizes, the Filtered Back Projection technique is the most commonly used method.

Calculation of projection data is the first step in the reconstruction of a CT image. The measured intensity data are normalized by the corresponding intensity obtained without presence of the object. The projection data values correspond to the sum of the linear attenuation coefficients values along the line of the transmitted radiation.

The linear attenuation coefficients of the material distribution in a two-dimensional section can be expressed by the function, $\mu^x(x, y)$, where x and y are the Cartesian coordinates specifying the location of points in the section. The intensity of radiation transmitted along a particular path is given by:

$$I = I_0 \exp\left[-\int_{x-ray\,source}^{\det ector} \mu^x(x, y) ds \right] \tag{A.3}$$

where ds is the differential of the path length along the ray. Reconstruction program in a X-ray CT system determines the distribution of $\mu^x(x, y)$ from a series of intensity measurements through the section. This equation may be rewritten in the form of Radon transformation of $\mu^x(x, y)$ equation, to give projection value, p^x:

$$p^x = \ln\left(\frac{I_0}{I} \right) = \int_{x-ray\,source}^{\det ector} \mu^x(x, y) ds \tag{A.4}$$

The above Radon transformation of $\mu^x(x, y)$ equation is fundamental to the CT process. Radon (1917) showed that $\mu^x(x, y)$ can be determined analytically from a given finite set of projection values (Appendix B).

A.2.3.1 Fourier Transform Reconstruction Technique

A Fourier transform is a mathematical operation that converts the object distribution defined in special coordinates into equivalent sinusoidal amplitude and phase distribution in special frequency coordinates (Appendix B). It is used as a reconstruction technique. The one-dimensional Fourier transformation of a set of projection data at a particular angle, θ, is described by:

$$P^x(\rho, \theta) = \int_{-\infty}^{+\infty} p^x(r, \theta) \exp(-2\pi\rho r) dr \tag{A.5}$$

where r is the spatial position along the set of projection data and ρ is the corresponding spatial frequency variable.

Central slice theorem is the basis of both Fourier transform reconstruction technique and filtered-backprojection method. This theorem states that the Fourier transform of a one-dimensional projection through two-dimensional distribution is mathematically equivalent to the values along a radial line through a two-dimensional Fourier transform of the original distribution. Taking the inverse two-dimensional Fourier transform yields the object distribution in spatial coordinates.

A.2.3.2 Filtered-Backprojection Technique

As mentioned earlier the Filtered Backprojection Technique (FBP) is the most commonly used CT reconstruction algorithm. Filtering operations, such as image

smoothing or sharpening, can be performed on the data in the spatial frequency domain. Backprojection is the mathematical operation of mapping the one-dimensional projection data back into a two-dimensional grid. It means that a visible structure in two or more images taken at different angles can backproject along the corresponding ray paths to determine the intersection of the rays and the location of the structure in space.

According to the central slice theorem the Fourier transform of the one-dimensional projection data through a two-dimensional distribution is equivalent to the radial values of the two-dimensional Fourier transform of the distribution. Consequently, the filtering operation can be performed on the projection data prior to backprojection. This is the conceptual basis of the filtered backprojection technique and it is a useful method for reconstructing the large image sizes.

A 3-D X-ray CT image is formed by a stack of 2-D reconstructed slices in equal distances (Figure A.6). The gaps between the 2-D slices are filled by finding the intensity of gap voxels using a linear interpolation.

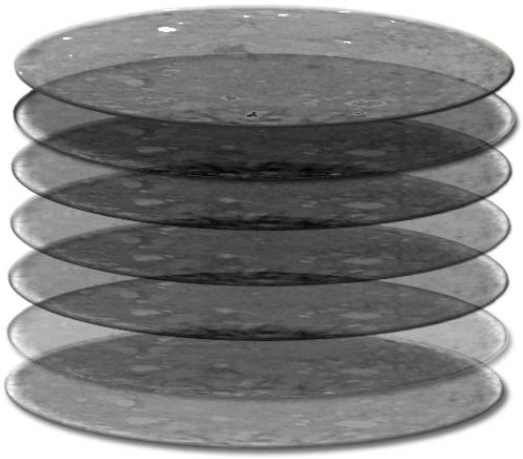

Figure A.6. A pile of 2-D reconstructed slices to generate a 3-D CT image

A.3 X-Ray CT System at Washington State University

The CT scans for this study are performed at the Washington State University High Resolution X-ray Tomography facility. The facility consists of Flat panel amorphous silicon high-resolution computed Tomography or FlashCT (Figure A.7). FlashCT is an advanced high-speed 3rd generation industrial X-ray CT based 3-D scanning system for nondestructive testing and evaluation. FlashCT is suitable for use within a wide spectrum of X-ray energies and geometric magnifications.

Washington State University's FCT-4200 is a novel design that incorporates both an X-tek 225 keV micro-focus X-ray source for material characterization at high magnification and a Pantak/Seifert 420 keV X-ray source for larger component analysis housed in a single radiation cabinet enclosure (Figures A.8). The micro-focus X-ray source takes advantage of an electromagnetic field and a vacuum pump around the X-ray outlet to reduce the X-ray spot size. The detector employed is a Varian PaxScan 2520 with CsI scintillator. The distance between adjacent pixels (pixel spacing) on the detector is *127 μm*. With the wide energy spectrum and high magnification available, the FCT-4200 can image a large variety of sample shapes, sizes, and densities. The X-ray CT components are placed in a protective cabinet against X-ray with external cabinet dimensions of *2.37 m (L) × 1.27 m (W) × 2.06 m (H)*. The walls of the cabinet have been built using two *3 mm* thick steel plates, which a *12 mm* thick lead plate has been placed between those plates. The thickness of the wall behind the detector is significantly more. Because of the limited dimensions of the protective cabinet, and also the other components inside, there is only a limited room for the specimens or any other instrument.

Figure A.7. FlashCT facility at Washington State University

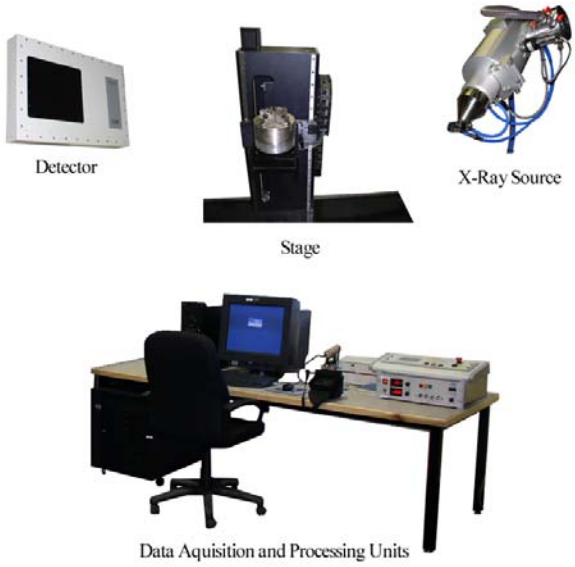

Figure A.8. Main components of FlashCT (or any other X-ray CT system in general)

A.4 X-Ray CT Scanning Procedure

Though the X-ray CT systems are very different, the scanning procedures are almost the same. The major steps to scan an object are:

1. Specimen size with respect to the effective atomic number of the object material, size of the stage, required resolution, and power of the X-ray source is examined to ensure such that scan is possible. This depends on many different variables and experience has the main role. However, most of the times a few scans prior to the main scan are performed to ensure that the CT image meet the requirements.
2. The object is fixed on the stage located between X-ray source and detector. The distance between object and X-ray source (or object and detector) is normally set based on the desired spatial resolution. If the distance between the X-ray source and detector, pixel spacing of the detector, and desired spatial resolution are assumed to be d, PS, and SR, respectively, then the distance between the object and the X-ray source, d_{source}, is obtained by Equation A.6. However, it is important to note that the maximum spatial resolution is limited to the system specifications. If the image size exceed than the detector, then d_{source} must be increased until the whole image fits in the detector.

$$d_{source} = d\frac{SR}{PS} \tag{A.6}$$

3. X-ray detector is calibrated, which for the number of photons that it counts for two different conditions; when the X-ray is off (dark field calibration) and when the X-ray is on with no object in the way of X-ray beam (light or gain field calibration). For light field calibration it is recommended to use close values to the scan values for X-ray current and intensity. No good quality image is obtained unless a good calibration is performed prior to the scan. Calibration may be repeated several times for the best result.
4. Rotary stage rotates the specimen a small angel then stops and a digital radiograph is taken. This process is continued to complete a full circle rotation.
5. 2-D CT slices are reconstructed from digital radiographs, and finally the 3-D CT image is formed by a stack of 2-D slices.

Appendix B

AN OVERVIEW OF DIGITAL IMAGE PROCESSING

B.1 Digital Image

A digital image is a discrete function. Its domain is the set of positive integer numbers and its range can be either the set of positive integer numbers (gray scale images) or the set of rational numbers between 0 and 1 including both 0 and 1 (RGB images). The elements of digital images are called pixel and voxel for two dimensional and three dimensional digital images, respectively. Pixels are small square shaped elements arranged in rows and columns that form the domain of the image. Voxels are small box shaped elements, formed by extruding a pixel to a finite imaginary thickness. In other words, voxels are extension of a planar element to a volume element to form three dimensional digital images.

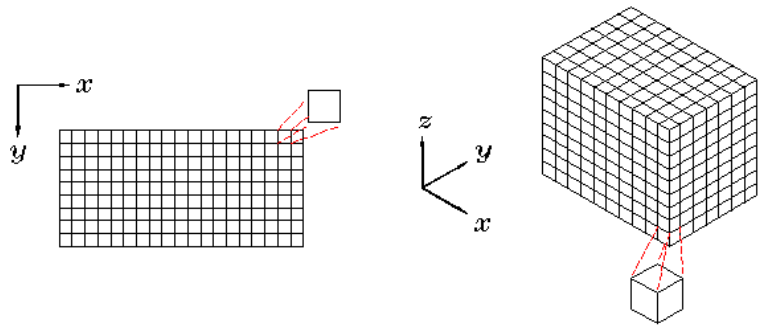

(a) (b)

Figure B.1. (a) A 2-D image and a magnified pixel (b) A 3-D image and a magnified voxel

The value of each pixel or voxel represents the intensity or amplitude of the image at that point. The intensity range for a gray scale image depends on the number of bits (the smallest part of the memory, which is either 0 or 1) in a byte. The image is referred to the number of bits in a byte. If the image consists of two colors only, black and white, then 1 can be considered for white and 0 for black. In this case one bit in a byte is enough to show those two colors. As such those images are called logical images.

To have different gray shades between black and white the number of bits in a byte must be increased. In an 8-bit gray scale image, each bit can be either 0 or 1, so the total number of possible gray shades will be 2^8 or 256 gray shades from black (00000000) to white (11111111). Figure B.2(a) shows an 8-bit gray scale image with the spectrum of the gray shades and Figure B.2(b) shows a logical (1-bit) image of the same image. Representation the different gray shades, using 8 bits in each byte, is shown in Figure B.3. In the same manner the total number of possible shades for a 16-bit and 32-bit gray scale images are 65,536, and 4,294,967,296.

For most applications 8 to 16 bits are sufficient and increasing the number of shades does not provide more accuracy or better quality. In practice and for most applications there is no significant difference between 8-bit, 16-bit, and 32-bit images; however a raw 16-bit image needs 256 times more memory than a raw 8-bit image, and a raw 32-bit image needs 16,777,216 times more memory than an 8-bit raw digital image.

The 8-bit image, which is made by putting the bytes together with no compression, is called a raw image. The image may be subjected to some rules such as compression to reduce the size. It may also include additional to make a standard graphical format that can be recognized by different operating systems.

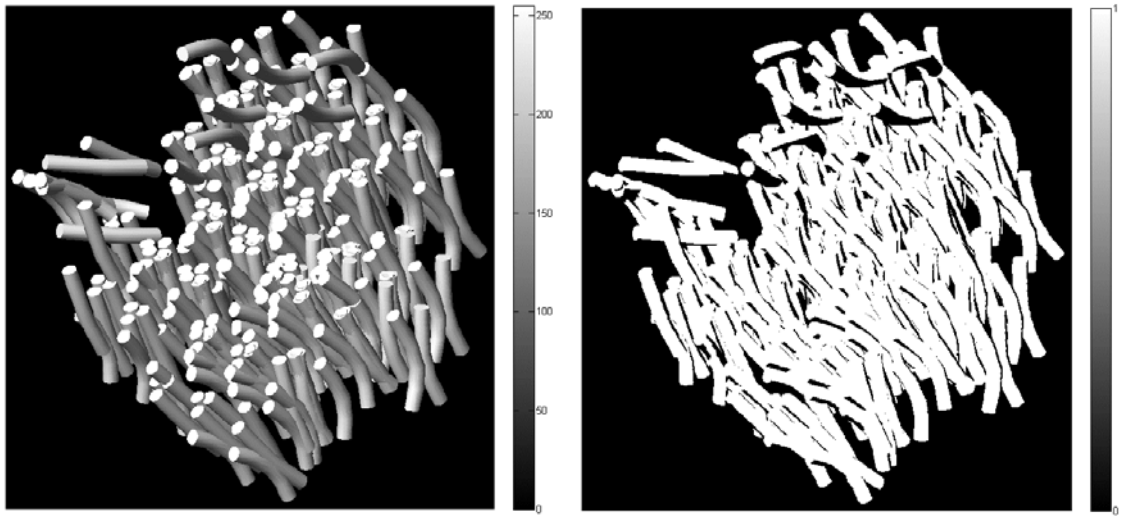

(a) (b)

Figure B.2. (a) An 8-bit gray scale image (b) logical image of the same image

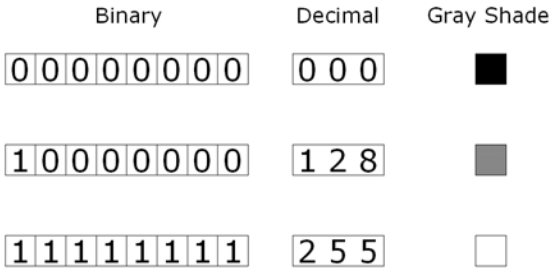

Figure B.3. Representation of different gray shades using 8 bits for each shade

The structure of the color images is somewhat different. Index images and true colors are two common types of color images. We give a brief introduction on how color is added to an image and the structures. A true color image, also known as RGB image color intensity of each pixel or voxel is defined by three bytes for three major colors red (R), green (G), and blue (B). In MATLAB a true color image is stored as an m×n×3 data

array, relating to images in three different layers, red, green, and blue. If 8 bits are used in each byte, then the combinations of the three major colors can represent 16,777,216 different colors, though the difference between all of the colors may not be recognized by human eye. Further, neither all monitors nor all printers can show or print all the combinations colors. Figure B.4 shows the individual values of red, green, and blue colors and an example of their combination.

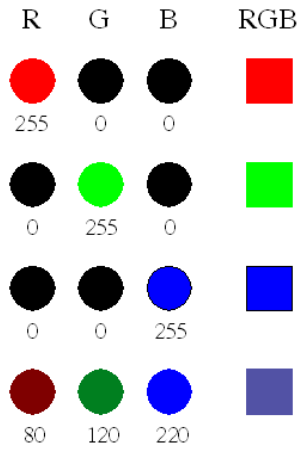

Figure B.4. Basic colors of true color images and a sample combination of basic colors

B.2 Digital Image Processing

Digital image processing consist of algorithms for contrast enhancement, noise reduction, image sharpening, segmentation, object recognition, and quantitative analysis of the image. Digital image processing is a wide field, and its application is ever increasing. Nowadays it plays a very important role in engineering, medicine, and science. In geotechnical engineering the digital images may be processed to find the numbers, dimensions, and orientations of the soil particles. It is used for diagnosis and tracking of the recovery progress using processed digital images taken by microscopes,

X-Ray CT scanners or MRI. In Astronomy it is used to find new born stars and counting the number of stars in a region. These are but a few examples of the countless applications of digital image processing. In this study digital image processing is used to process three-dimensional X-ray CT images of sand specimens to find the representative elementary volume element (REV) size, to study shear band characteristics, and to obtain the three-dimensional displacement field between the two successive 3-D X-ray CT images.

In 3-D image processing and computer vision fields, the size of the problem and the processing time depends on computer hardware and specifications and limitations of the operating system. At the present time computers based on MS-Windows XP operating system support up to a maximum of 4 GB of RAM with a maximum CPU speed between 3 GHz to 4 GHz. These values are so small for processing a 3-D image unless the codes are optimized to use a minimum amount of RAM memory. Note that the processing time can be reduced by parallel processing.

Many commercial digital image processing computer programs are available at present. A person can also develop his or her own image processing algorithm depending on the type of need.

B.3 Structure of FlashCT Output Files

It is necessary to understand the structure of the files, which are generated by FlashCT during scan and reconstruction to process the images. Digital radiographs (DR) are saved in a series of raw files with raw extension during scan. The raw files are used to generate sinograms, and reconstructed files. Each FlashCT data file consists of 25 bytes header followed by image data and optional footer information. The first 25 bytes

of the files provide meta-data about the file, describing the type and format of data. The data following the header is an array of Height × Width × Depth bytes scaled between 0 and ($2^{8\times Depth}$-1). To map the data from image to image, the data must first be converted into floating point form using the origianl maximum and minimum values (Anthony Davis and Jeff Hay 2003). Detailed discussion of the header file bytes and a sample code to read FlashCT image file format in MATLAB may be found in publication HYTEC: HTN-107990-0015 (1/14/2003).

The 3-D image is read and stored in a 3-D array of numbers. The height, width, and length of the volume generated by FlashCT-DAQ (data acquisition program) are determined by the height of crop region (in full resolution mode). Crop region here is referred to a rectangular region in FlashCT-DAQ that is used to define the scanning region of scan. For example if the height and width of the crop region in FlashCT-DAQ are 240 pixels and 500 pixels, respectively, then 500 two dimensional 240×240 slices are generated and the corresponding volume will have 240×240×500 voxels in width, length, and height, respectively. Figure B.5 shows the relation between the crop region size and the generated volume for FlashCT.

The data corresponding to voxel gray shades are stored as 16 bit unsigned integers ranging from 0 to 65,535. The data may be converted to 8-bit unsigned integers ranging 0 to 255. This conversion has small effect on image resolution but reduces image size. However, this conversion is not always useful and it is not recommended for sensitive image processing projects.

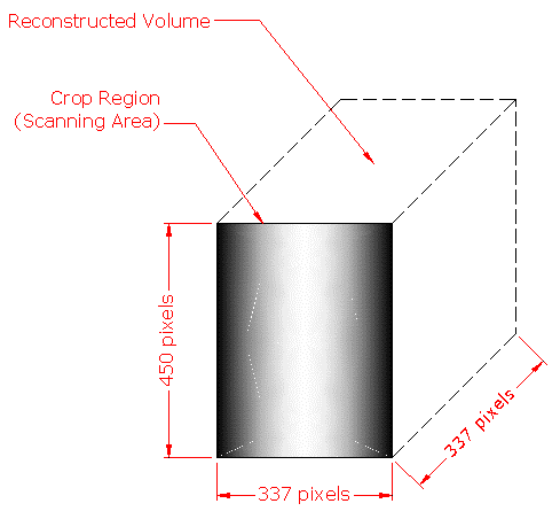

Figure B.5. Relation between the crop region size and the generated volume

B.4 Quality Improvement of X-ray CT Images

CT images may need some improvement in contrast enhancement, background noise removal, and container wall removal. It is also desirable to have CT slice images in standard graphical file formats such as BMP, TIFF, or PNG in three different Cartesian coordinates planes XY, YZ, and XZ.

An interactive computer program called MFC was developed to perform the above tasks. This program can load a 3-D X-Ray CT volume, adjust image contrast (manual or automatic), remove background noise or container wall, crop the image, rotate the image for any arbitrary angle, extract the CT slices as a series of standard graphical file formats (TIFF, BMP, and PNG) in XY, YZ, or XZ planes, and save the whole image as a MAT file, which can be read by MATLAB. MFC has the ability to save the circular and rectangular crop regions for applications including similar images as well as contrast settings.

B.5 Thresholding

Thresholding is a process used to extract a desired feature of an image from the rest. The simplest case of thresholding involves choosing a number in the range of gray shade values to divide it into two parts. Depending on the problem the gray shade values of one part is replaced with 0 and the other part is replaced with 1. Threshold may be set by a user just by observing the separated regions. Figure B.6 represents an example of the application of different threshold values for a CT slice of glass beads. Comparing the logical images with the original image shows that a threshold value of 10 is too small to extract the beads only, while a threshold value of 40 is too large to captures all the beads. In this example a threshold between 20 and 30 appears to be a good value. Even though visual examination gives reasonable estimate of threshold it is subjective.

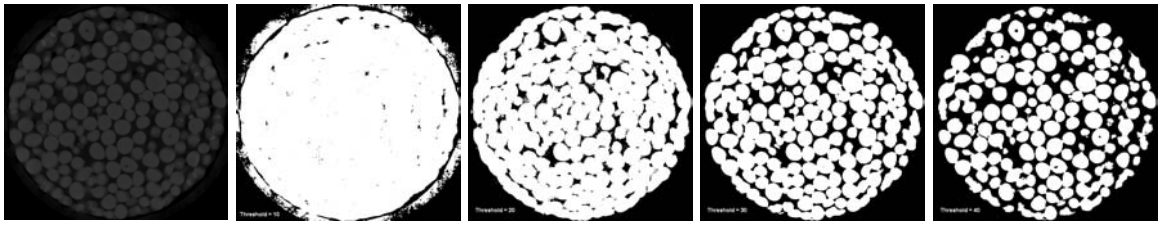

(a) (b) (c) (d) (e)

Figure B.6. A CT slice of glass beads and logical images with different thresholds "t"

(a) original image (b) t=10 (c) t=20 (d) t=30 (e) t=40

In some cases, threshold can be chosen by equating a specific property form other measurements with that estimates from image analysis. For example, the threshold values can be modified until the global porosity of the specimen measured using gravimetric methods matches to that obtained from image analysis. Figure B.7 shows a

plot of porosity obtained as a function of threshold values. It is seen even a small change in threshold has a significant effect on porosity. Therefore, as a result of sensitivity to averaging errors this method may not give the best threshold. Thus it is only recommended to obtain a preliminary estimate.

Image brightness histogram is a practical method that enables us to obtain the best threshold automatically. Brightness histogram is a plot of the number of pixels in the image with a given gray shade value. The brightness histogram of a CT slice of glass beads is shown in Figure B.8. This histogram has two distinct peaks separated by a trough. The trough divides the brightness histogram into two regions. The left and the right sides of the trough represent the background and foreground of the image, respectively. Trough location can be considered a threshold, however, in many cases the brightness histogram has more than two peaks or difference between the peaks is negligible making it difficult to identify a threshold. Different methods such as valley sharpening technique (Weszka et al. 1974), the difference histogram method (Watanabe et al. 1974), and Otsu's method (Otsu 1979) have been proposed to provide better guidance on the selection of threshold.

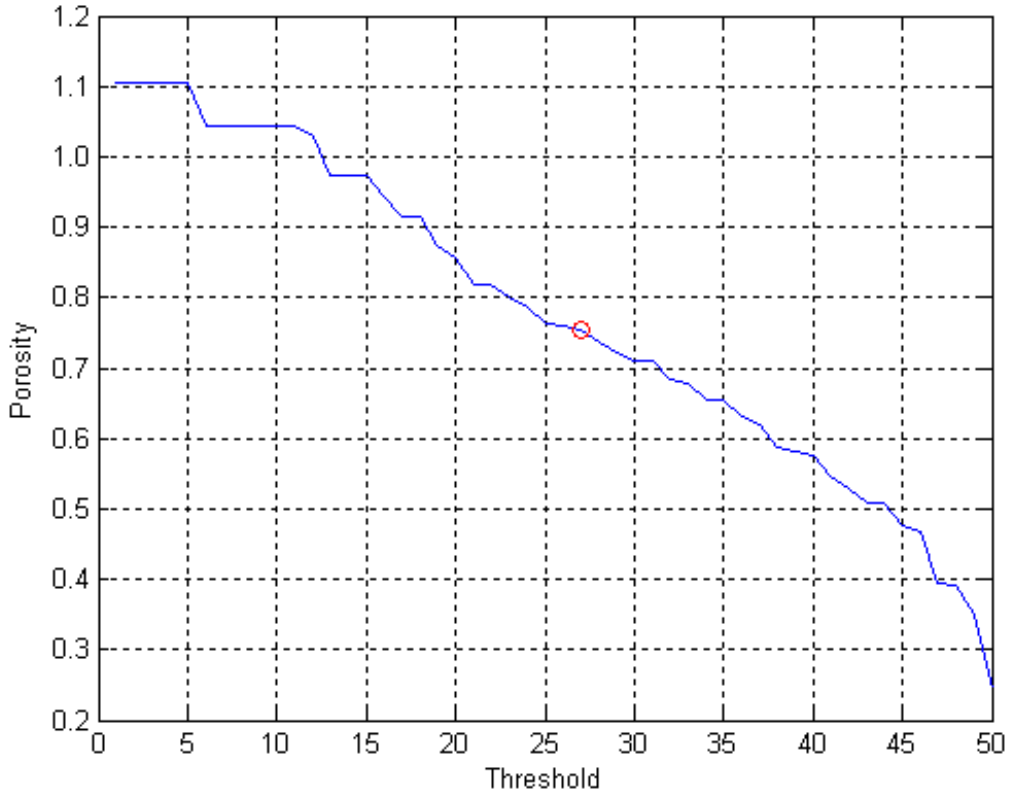

Figure B.7. Variation of porosity versus threshold (the red circle corresponds to the best threshold)

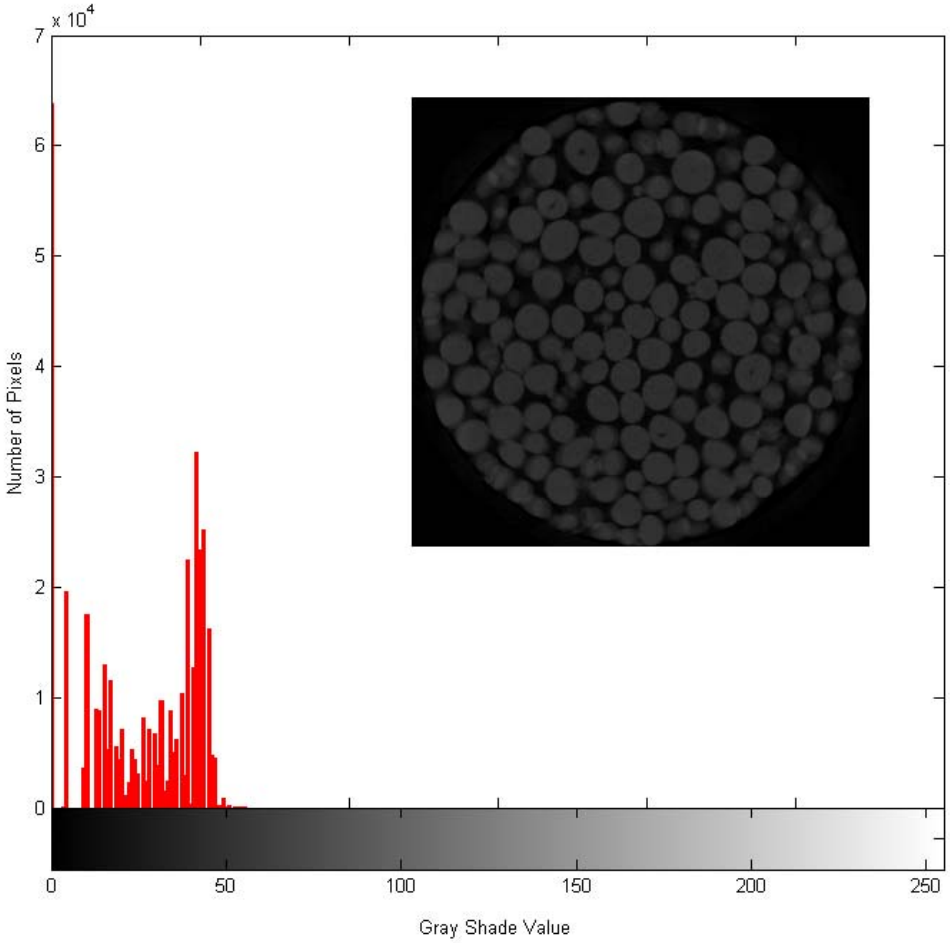

Figure B.8. Brightness histogram of a CT slice of glass beads

B.5.1 Otsu's Thresholding Method

Otsu (1979) proposed a powerful technique to find the optimum threshold from the image brightness histogram. In this method, the brightness histogram is normalized. Subsequently it is divided into two classes; one with the pixel values less than the threshold and the other with values greater than the threshold. Note that the threshold value is unknown at this point. The probabilities of class occurrence, the class mean levels, the zero and the first order cumulative moments of the brightness histogram up to the threshold value level, the total mean level of the original image, and class variances are calculated. Based on the calculated parameters three object functions are considered, the within-class variance, the between-class variance, and the total variance of levels. The optimum threshold value is obtained by maximizing one of the object functions. It has been proved that the maximum and so the threshold always exist and this is one of the main advantages of Otsu's method (Otsu 1979). Figure B.9 illustrates the application of this method for a CT slice of glass beads. The best threshold calculated using this method is 27.

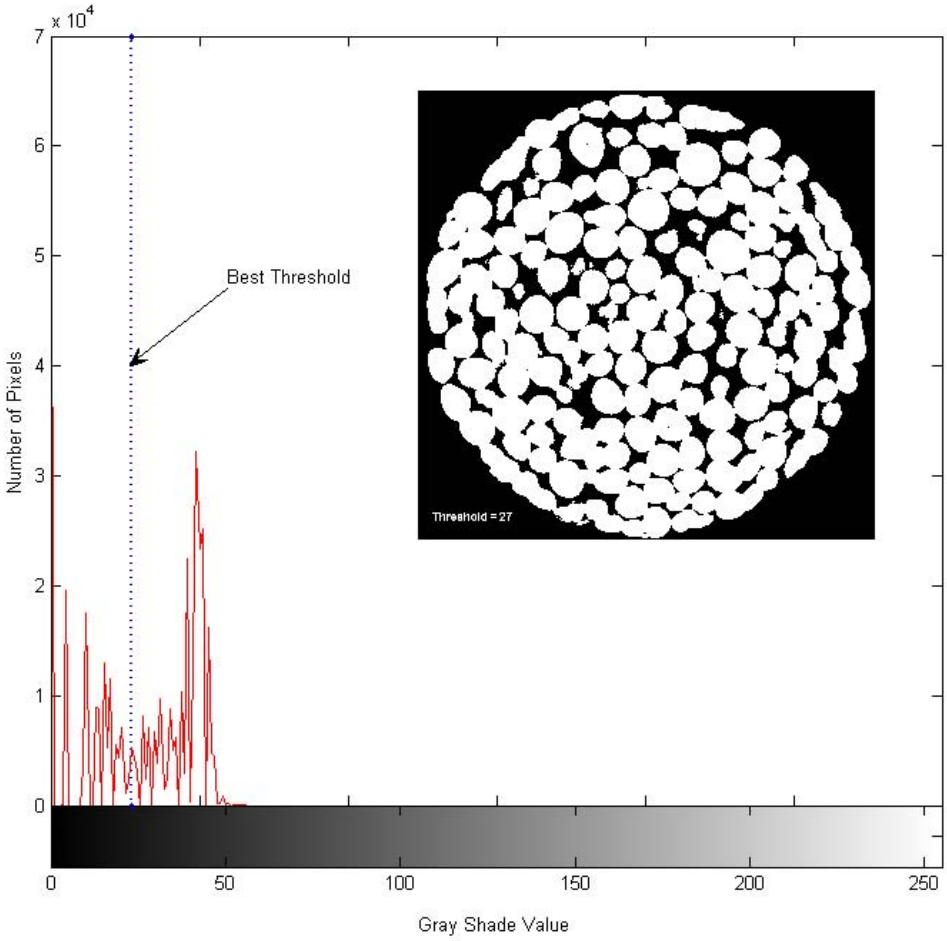

Figure B.9. Illustration of Otsu's method with the logical image after application of threshold

B.6 Filtering

A neighborhood operation for modifying or enhancing an image is called filtering. Filtering algorithm is applied to the neighborhood of an input pixel to determine the pixel value of the output image. Filtering operation can be linear or nonlinear. The output pixel value is a linear combination of the neighborhood pixels in linear filtering. Filtering is done using convolution or correlation. Convolution is an operation to find each output pixel value by using the weighted sum of neighboring input pixels. The matrix of the weights is referred to as the filter. Correlation procedure similar to convolution but the filter is rotated by 180° before it is applied to the neighborhood pixels. For the pixels along the image boundary, the values of the pixels off-the-edge image are assumed zero (MATLAB IPT 5.1)

Convolution and correlation are explained by the following example. Suppose the image is:

$$I = \begin{bmatrix} 0 & 2 & 1 & 3 \\ 10 & 3 & 4 & 8 \\ 9 & 0 & 2 & 1 \\ 5 & 0 & 1 & 5 \end{bmatrix} \tag{B.1}$$

and the filter is:

$$f = \begin{bmatrix} 2 & 1 & 3 \\ 4 & 3 & 5 \\ 7 & 8 & 6 \end{bmatrix} \tag{B.2}$$

In order to find the value of the filtered image at row 3 and column 2 using correlation the center of filter is placed at *I(3,2)* and the output pixel value is determined by:

$$2\times10+1\times3+3\times4+4\times9+3\times0+5\times2+5\times7+8\times0+6\times1=123 \qquad \text{(B.3)}$$

Filter must be rotated 180° to filter the image using convolution:

$$f^{180}=\begin{bmatrix}6 & 8 & 7\\ 5 & 3 & 4\\ 3 & 1 & 2\end{bmatrix} \qquad \text{(B.4)}$$

Now *I(2,3)* is determined by:

$$6\times10+8\times3+7\times4+5\times9+3\times0+4\times2+3\times5+1\times0+2\times1=182 \qquad \text{(B.5)}$$

Different filters are designed and used for various image processing tasks such as edge detection, sharpening, and blurring. Those filters are available in most image processing computer programs. Figure B.10 shows an application of image filtering using this filter to make edges and fine details in the image crisper.

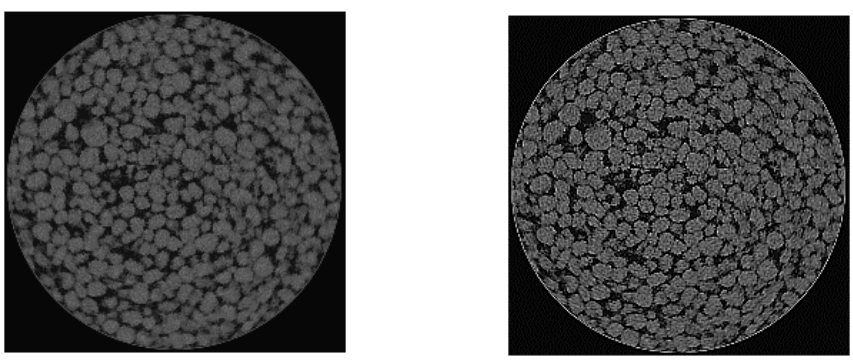

(a) (b)

Figure B.10. (a) An original CT slice of silica sand (b) filtered image using unsharp mask

B.7 Transformations

The transformed image is further processed using different mathematical transformations such as Fourier transform, discrete cosine transform, radon transform,

and wavelet transform. These transformations are useful for image processing tasks that deal with convolution, enhancement, restoration, feature detection, and image compression. A brief description of the discrete Fourier transformation, discrete cosine transformation, and Radon transformations are presented below.

B.7.1 Discrete Fourier Transform

The discrete Fourier transformation transforms an image *f(x,y)* from spatial domain to frequency domain by (MATLAB IPT 5.1):

$$F(\omega_1, \omega_2) = \sum_{x=-\infty}^{x=\infty} \sum_{y=-\infty}^{y=\infty} f(x, y)\, e^{-i\omega_1 x}\, e^{-iw_2 y} \tag{B.6}$$

Where *f(x,y)* is the pixel value of digital image *f* at location *(x,y)*, *i* is complex number ($i^2 = -1$) ω_1, and ω_2 are frequency variables with units of radian per sample. Inverse Fourier transform is used to recover the original image *f* from F:

$$f(x, y) = \frac{1}{4\pi^2} \int_{\omega_1=-\pi}^{\omega_1=\pi} \int_{\omega_2=-\pi}^{\omega_2=\pi} F(\omega_1, \omega_2)\, e^{i\omega_1 x}\, e^{i\omega_2 y} \tag{B.7}$$

$|F(\omega_1, \omega_2)|$ is usually used as a representation of discrete Fourier transform. *F(0,0)* represents the sum of all the pixel values in *f*. Figure B.11 shows an image in spatial domain and its Fourier transformation in frequency domain.

Fourier transform is often used for filtering, convolution, and feature detection. To filter an image in frequency domain, first the Fourier transform of the image is determined. Filter is applied to this image in frequency domain. Finally, inverse Fourier transform of the image is determined. This process enables us to filter out certain frequencies.

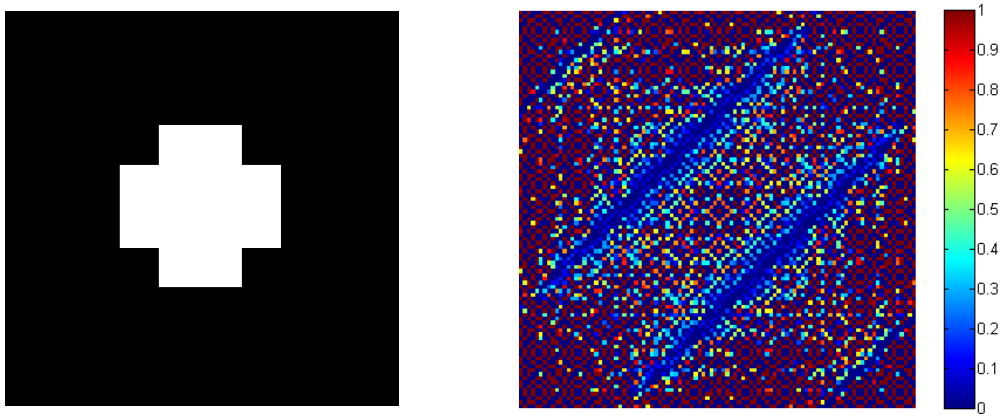

(a) (b)

Figure B.11. (a) An image in spatial domain (b) the same image in frequency domain

Figure B.12 shows a CT slice of silica sand and the same image after applying Gaussian filter on frequency domain.

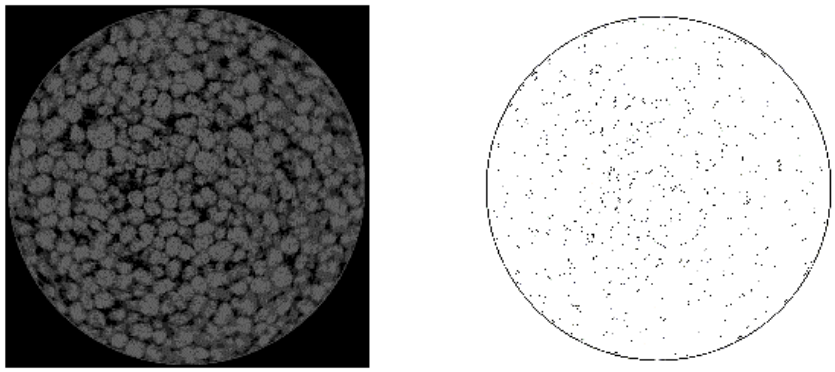

(a) (b)

Figure B.12. (a) CT slice of silica sand (b) filtered image after applying Gaussian filter

Feature detection using Fourier transform is done by creating a template and by matching its location the image. Template is a small rectangular region (for 2-D images)

or a box volume (for 3-D images) of the image, which contains the desired feature. The correlation of the template with the original image is computed and the maximum pixel values identify the locations of the template.

Figure B.13 shows an image of a text in both horizontal and vertical directions. To find the locations of letter “e” in horizontal direction, first a part of image containing letter “e” is captured and stored as template (Figure B.14). Then the correlation of the template with the original image is computed (Figure B.15). The maximum values of the pixels on the correlated image correspond to the locations of the template in the image (Figure B.16). Note that template must be rotated 90° clockwise before applying correlation to find the template locations in the vertical text. For a general case the rotation angle of the template is considered an unknown that is eventually found by optimization.

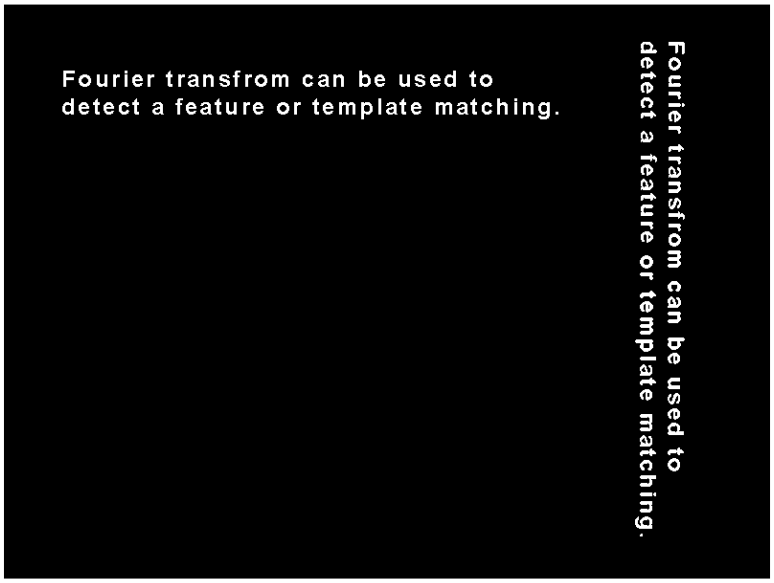

Figure B.13. Image of a text

Figure B.14. Template image (magnified)

Figure B.15. Correlated image

Figure B.16. Locations of template in the image (white spots)

B.7.2 Discrete Cosine Transform (DCT)

The discrete cosine transform of a two dimensional image stored as a M×N matrix A is defined by (MATLAB IPT 5.1):

$$B_{pq} = \alpha_p \alpha_q \sum_{m=0}^{M-1} \sum_{n=0}^{N-1} A_{mn} \cos\frac{\pi(2m+1)p}{2M} \cos\frac{\pi(2n+1)q}{2N}$$

$$\begin{aligned} 0 \le p \le M-1 \\ 0 \le q \le N-1 \end{aligned} \tag{B.8}$$

α_p and α_q are defined by:

$$\alpha_q = \begin{cases} 1/\sqrt{N} & for \;\; q = 0 \\ \sqrt{2/N} & for \;\; 1 \le q \le N-1 \end{cases} \tag{B.9}$$

$$\alpha_p = \begin{cases} 1/\sqrt{M} & for \quad p = 0 \\ \sqrt{2/M} & for \quad 1 \le p \le M-1 \end{cases} \tag{B.10}$$

This transformation concentrates most of the visually significant information about an image in a few coefficients. Therefore, this transformation is very useful for image compression and it is used to compress the image using JPEG[2] format. Discrete cosine transformation is invertible and its inverse is given by:

$$A_{mn} = \sum_{p=0}^{M-1} \sum_{q=0}^{N-1} \alpha_p \alpha_q B_{pq} \cos\frac{\pi(2m+1)p}{2M} \cos\frac{\pi(2n+1)q}{2N}$$

$$\begin{aligned} 0 \le p \le M-1 \\ 0 \le q \le N-1 \end{aligned} \tag{B.11}$$

α_p and α_q are defined by:

$$\alpha_q = \begin{cases} 1/\sqrt{N} & for \quad q = 0 \\ \sqrt{2/N} & for \quad 1 \le q \le N-1 \end{cases} \tag{B.12}$$

$$\alpha_p = \begin{cases} 1/\sqrt{M} & for \quad p = 0 \\ \sqrt{2/M} & for \quad 1 \le p \le M-1 \end{cases} \tag{B.13}$$

Figure B.17 (a) shows a CT slice image in TIFF format and Figure B.17 (b) shows that image after compression using discrete cosine transform. Though quality of the compressed image is less, it is clearly recognizable and its size is 22.5 times less.

[2] Joint Photographic Expert Group

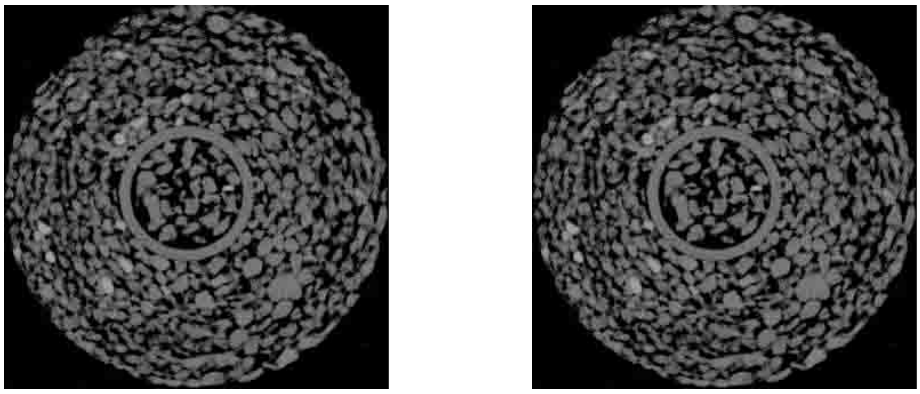

(a) (b)

Figure B.17. (a) Original CT slice (b) compressed image using DCT

B.7.3 Radon Transform

Radon transformation is at the core of the reconstruction technique in computed tomography. Figure B.18 shows a two-dimensional function *f(x,y)* and its parallel projection on a detector. A projection is formed by combining a set of line integrals.

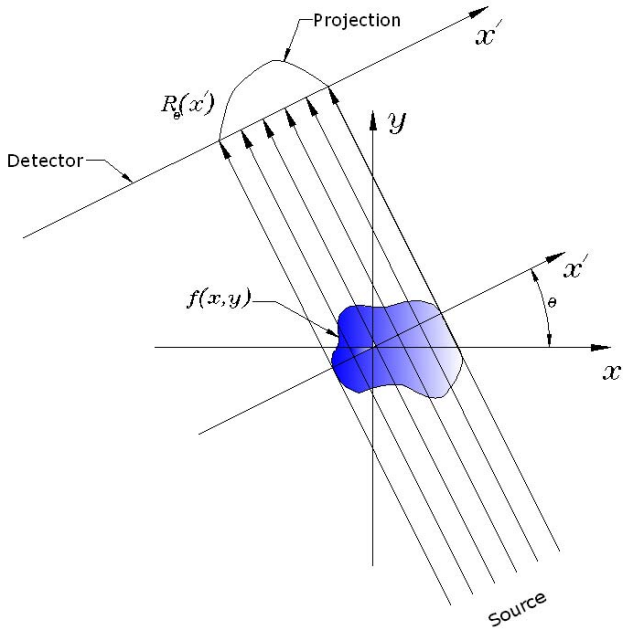

Figure B.18. Parallel projection of a two dimensional function *f(x,y)*

If the distance of any point of *f(x,y)* from the origin along x' axis is indicated by *t*, then Radon transformation is given by (MATLAB IPT 5.1):

$$\Re\{f(x,y)\} = \int_{-\infty}^{\infty}\int_{-\infty}^{\infty} f(x,y)\delta(x\cos\theta + y\sin\theta - t)dxdy \tag{B.14}$$

δ is the Dirac delta function defined by:

$$\delta(z) = \begin{cases} \infty & if \quad z = 0 \\ 0 & if \quad z \neq 0 \end{cases} \tag{B.15}$$

If the source is placed in a fixed position relative to line of detector another type of projection is formed, which is known as a fan beam projection (Figure B.19).

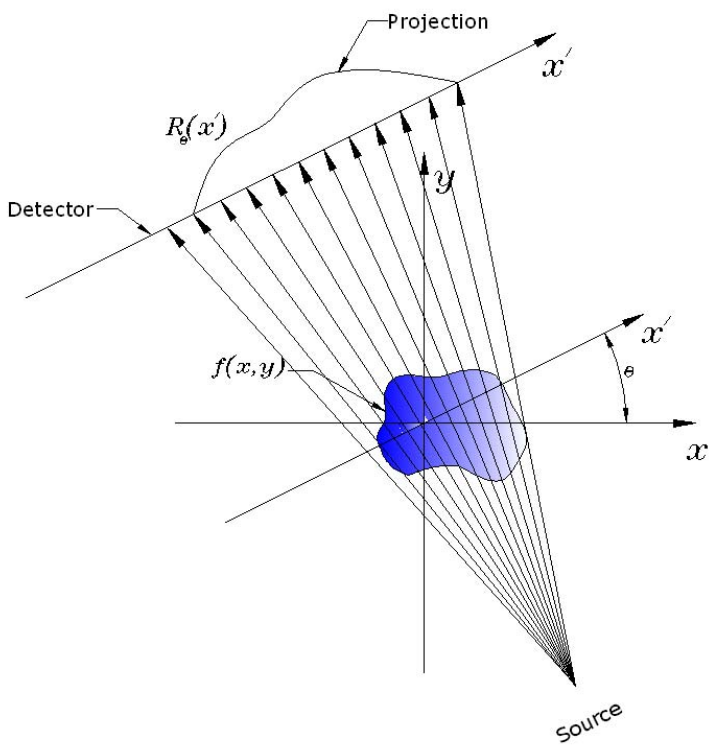

Figure B.19. Fan beam projection of a two dimensional function *f(x,y)*

For two dimensional images with parallel projection, Radon transformation at each point along the detector line (x') is simply determined by adding all the pixel values along the ray perpendicular to the point. Figures B.20, and B.21 show Radon transform of a cross-shaped logical image at 0° and 45° angles, respectively. The horizontal axis shows the pixels along the projection line and vertical axis shows the summation of the pixels along each ray or the value of Radon transformation.

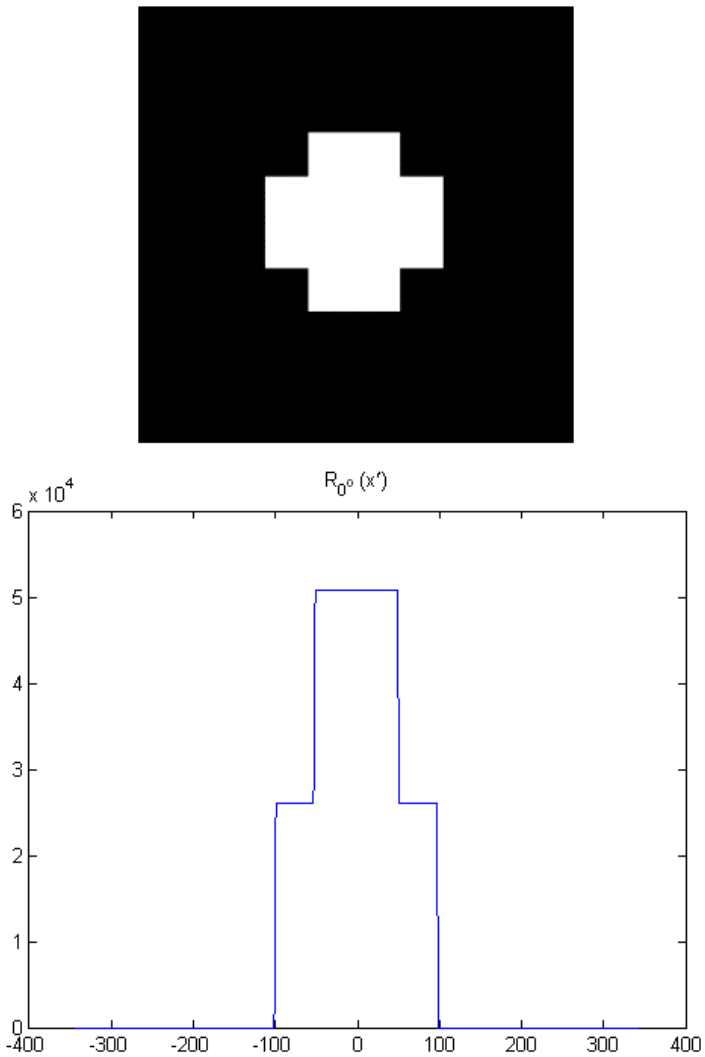

Figure B.20. Radon transform of a logical image at 0°

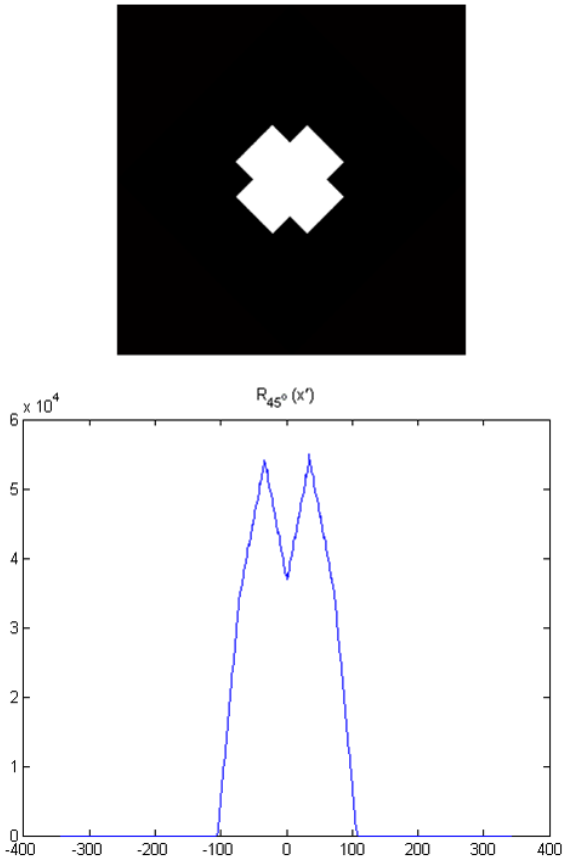

Figure B.21. Radon transform of a logical image at 45°

Radon transform is invertible and it can be used to reconstruct an image from its projections at different angles. Figure B.22 shows 360 parallel projections of an image in 1° increment. Figure B.23 shows the reconstructed image from those projections using inverse of Radon transform. Quality of the reconstructed image is a function of projections. However, number of projections has an optimum more than which does not have any effect on quality of the reconstructed image. Figures B.24 and B.25 show the reconstructed images using 36 and 3600 projections, respectively. As it is seen 36 projections are not enough, while 3600 projections do not have any significant effect in

improving image quality. However, it is important to know that all reconstructed images are subjected to some kinds of artifacts.

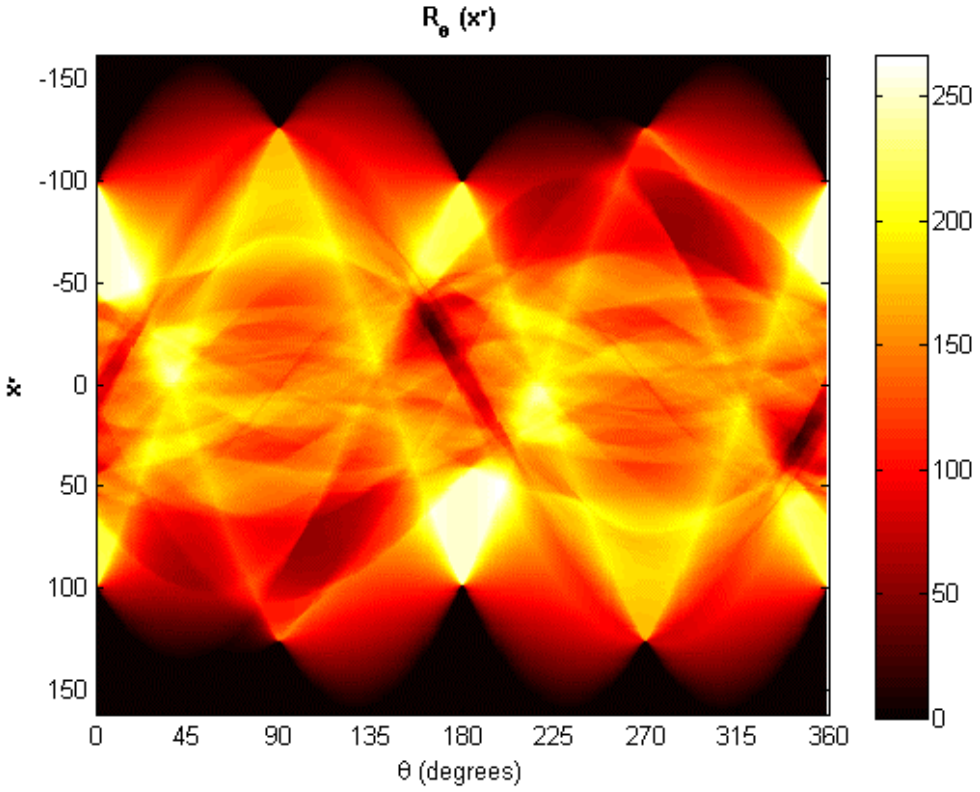

Figure B.22. 360 parallel projections of an image in 1° increment

(a) (b) (c)

Figure B.23. (a) Original gray scale image (b) logical image (c) reconstructed image using 360 projections

Figure B.24. Reconstructed image using 36 projections

Figure B.25. Reconstructed image using 3600 projections

B.8 Morphological Operations

Morphological operations are those that relate to shapes such as skeletonization, filling, and segmentation. Skeletonization reduces all objects in an image to lines according to image structure (Figure B.26). Filling is a morphological reconstruction operation used to fill the closed loops (Figure B.27). Segmentation subdivides an image into objects. It is considered to be one of the most difficult tasks in image processing. Several methods exists for segmentation and we present a brief description of the watershed transform (Gonzalez et al. 2004).

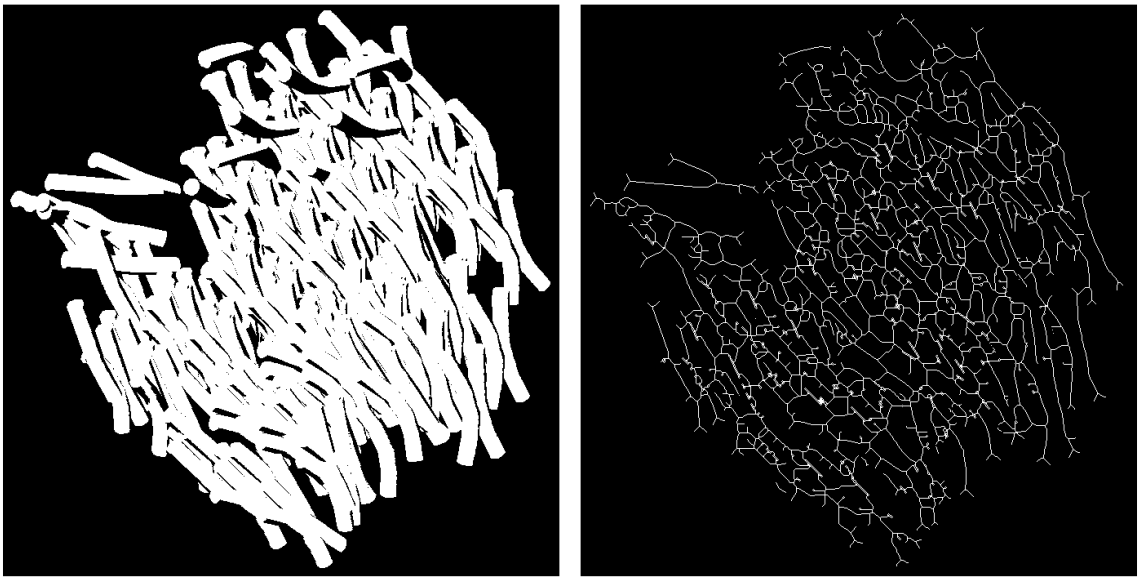

(a) (b)

Figure B.26. (a) Original image (b) image after skeletonization

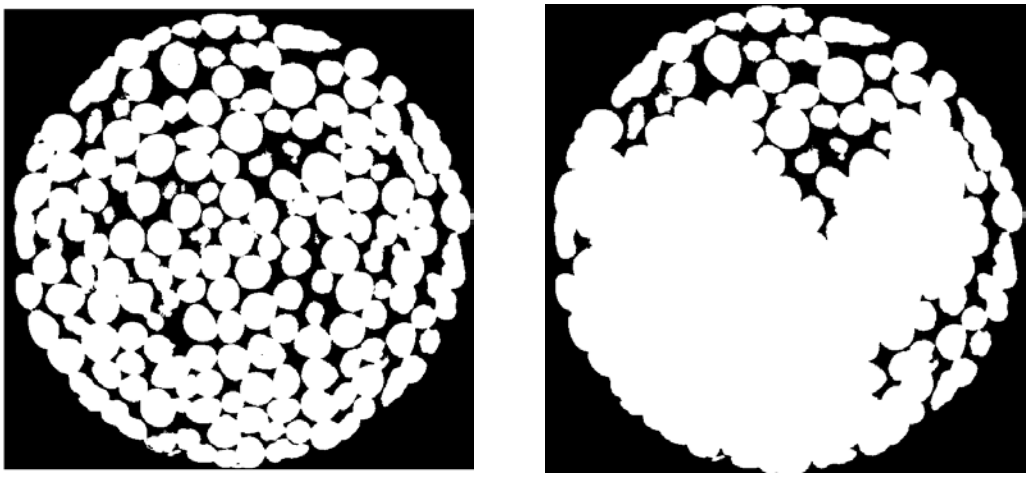

(a) (b)

Figure B.27. (a) Original image (b) image after filling holes (closed loops)

B.9 Watershed Transform

Merriam-Webster's Collegiate Dictionary (2006) defines watershed as a "divide" or "a region or area bounded peripherally by a divide and draining ultimately to a particular water course or body of water". The same concept is used in image processing to solve variety of image segmentation problems. If the gray scale vales on the images are considered as elevations on a topography map then the dividing lines between humps or pits are known as watershed lines or watershed ridge lines. Figure B.29 shows a gray scale image of four circles. For the two top circles gray shades varies from 0 at the center to 255 around the edges, while for the two bottom circles gray shades varies from 0 around the edges to 255 at the center. Figure B.30 is a representation of these circles in a 3-D Euclidian space by assuming an elevation equal to the gray shade value of each pixel.

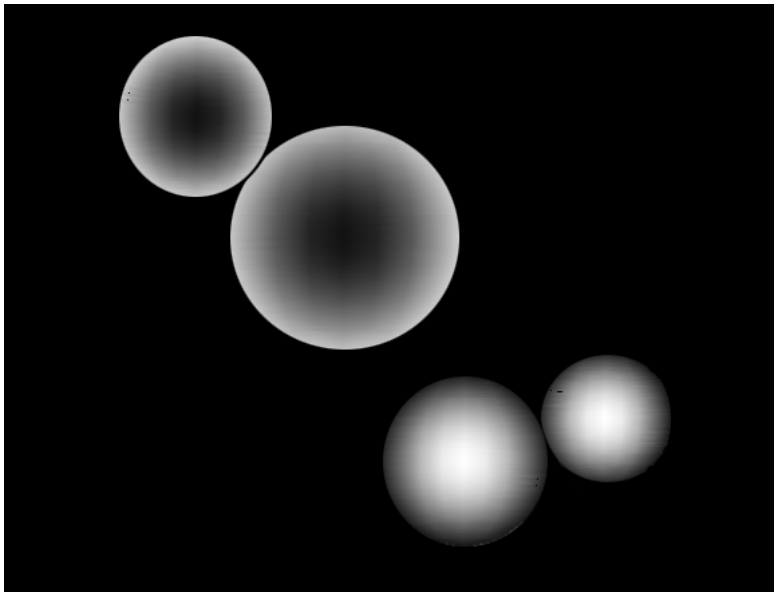

Figure B.28. A gray scale image of four circles touching two by two

It is evident that the circles form two humps and two pits. The dividing lines between the two humps or the two pits are called watershed lines. Watershed segmentation is a very useful operation in the segmentation of granular material images.

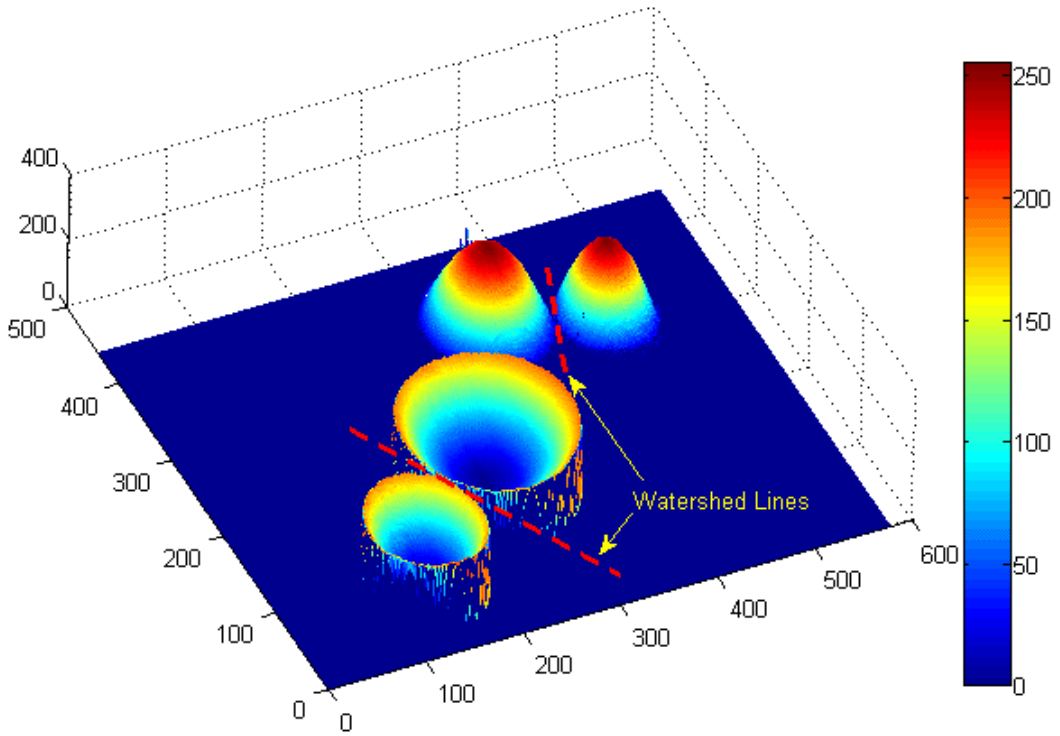

Figure B.29. Representation of circles in Figure B.29 assuming an elevation of gray shade values at each pixel

One of the commonly used tool in conjunction with watershed transform for segmentation is the distance transform. It is the distance from every pixel to the nearest nonzero-valued pixel in a logical image. The distance transforms of one-valued pixels are zero. A practical application of watershed transform in segmentation of touching glass beads is shown in Figure B.30.

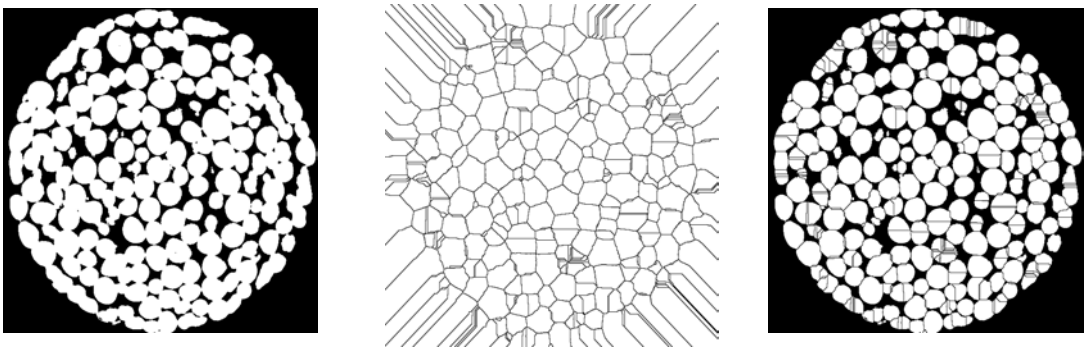

(a) (b) (c)

Figure B.30. (a) A logical CT image of glass beads (b) watershed transform of the image (c) segmented image

When the boundaries of the particles are not well distinguished by distance transform gradient method is applied prior to the watershed transform. Gradient method traces the particle boundaries by locating abrupt changes in pixel values. A common problem with watershed transform is oversegmentation. This problem is seen in Figure B.30(c) where some particles have been divided to several particles. This problem is solved using a technique called minima imposition (Soille, 2003). This technique modifies a gray scale image so that regional minima occur only in certain marked locations. Figure B.31 shows application of this technique to correct oversegmentation problem of Figure B.30(c).

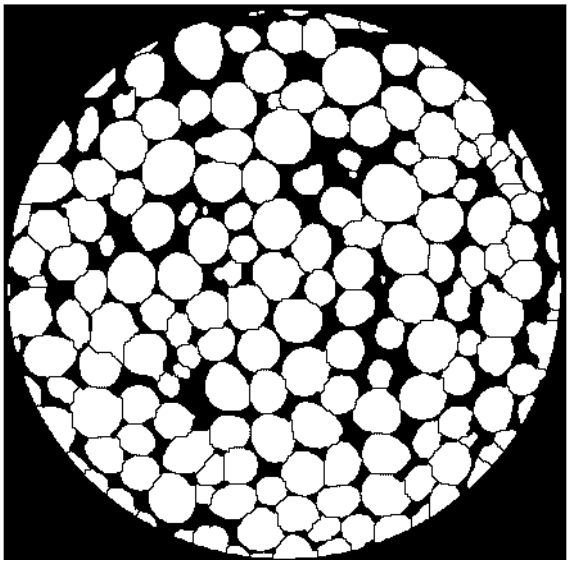

Figure B.31. Correction of oversegmentation problem in Figure B.31(c) using minima imposition technique

Appendix C

AN ALTERNATE DESIGN OF X-RAY CT TRIAXIAL

If the required axial load or cell pressure is more than the maximum values in the first design, then a different approach must be employed. It is evident that in this case a large and heavy loading frame is required, which can not be mounted on the top of the cell. Figure C.1 shows a section of the loading frame and the cell. Loading frame is placed outside imaging area, and cell is designed for a tensile hoop stress only. Top cap and base plate of the cell are connected using a few steel rods out of the imaging area. In this design position of the loading frame is fixed, while cell, specimen, and loading ram rotate with the rotation of the X-ray CT stage. In this case two ball-bearing systems are used to reduce the friction, one on the top, and the other at the bottom of the cell.

This design guarantees application of very large loads and cell pressures inside the X-ray CT chamber, unless the stage motor cannot provide adequate torque for rotation. This design is applicable for both compressive and tensile triaxial test on a wide range of materials including asphalt concrete, concrete, metals, rocks, etc.

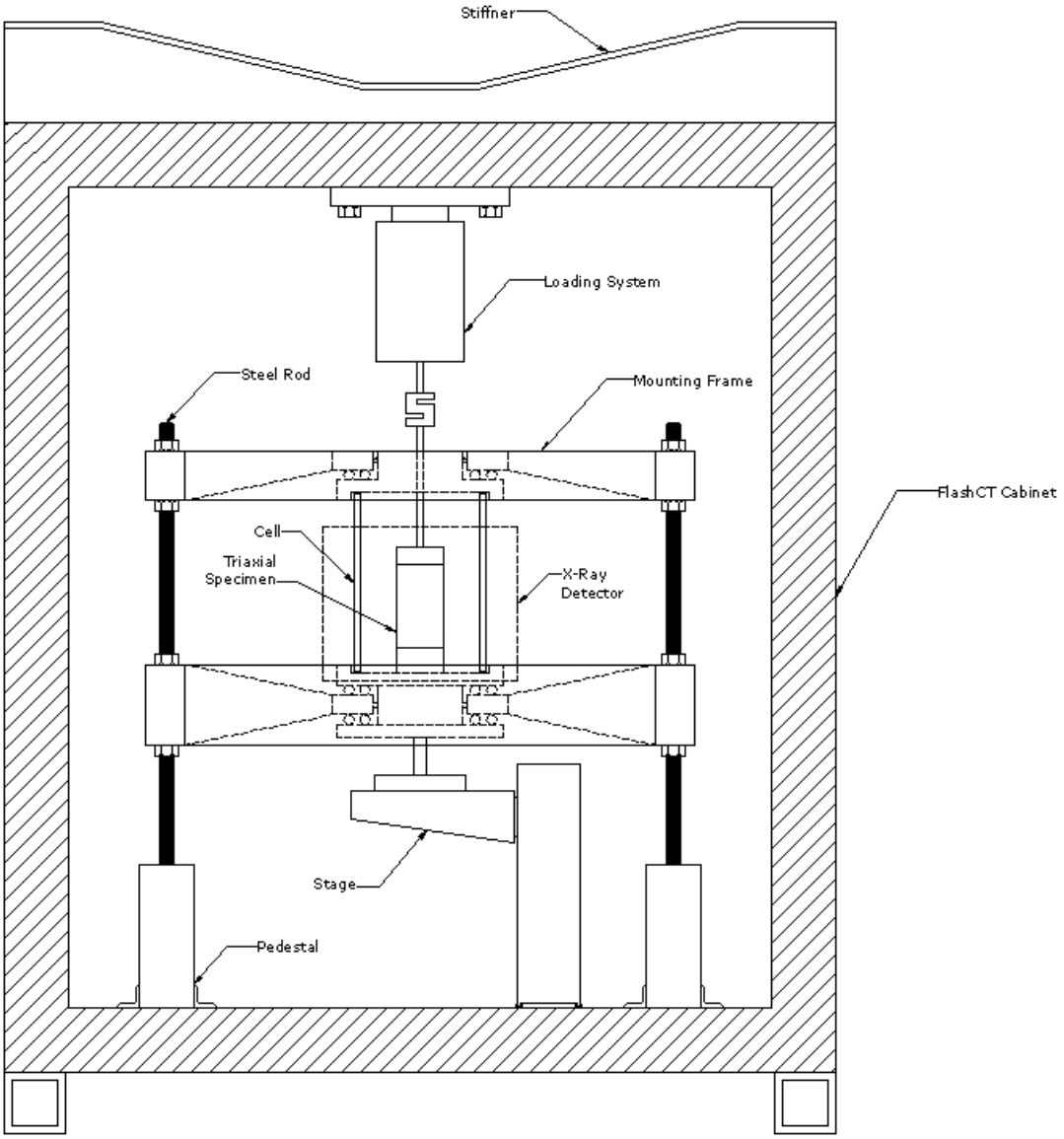

Figure C.1. Another triaxial design for large load applications